



NTNU – Trondheim
Norwegian University of
Science and Technology

Experimental study of bubble characteristics and heat transfer in subcooled flow boiling of R-134a

Keun-Soo Park

Master's Thesis

Submission date: August 2013

Supervisor: Carlos Alberto Dorao, EPT

Norwegian University of Science and Technology
Department of Energy and Process Engineering



Norwegian University of
Science and Technology

Experimental study of bubble characteristics and heat transfer in subcooled flow boiling of R-134a

Keunsoo Park

Master of Science in Energy and Processing Engineering

Submission date: June 2013

Supervisor: Carlos Alberto Dorao, IVT

Norwegian University of Science and Technology

Department of Energy and Process Engineering

Abstract

Because of its high heat transfer efficiency, subcooled flow boiling can contribute to the miniaturization of subsea heat exchangers. An experimental investigation was conducted to study the parametric influence on the distribution of bubble sizes and velocities as well as the heat transfer coefficient in the subcooled flow boiling of R-134a in a horizontal conventional annular channel. High-speed visualization was used to capture the flowing bubble behaviors at the end of a heated tube. The association between the heat transfer coefficients and various bubble characteristics, such as bubble size, velocity, population and interfacial area concentration, under different operating conditions were revealed. Most of the bubbles in the experiments slid along the upper part of the heated tube, while only tiny bubbles lifted off the surface. Bubble size distributions have a bimodal shape, composed of two different bubble size groups. The distributions of two bubble size groups follow the type 1 distribution of Pearson's system and were interpolated using this system in order to develop a population balance framework for further study. Bubble sliding velocities were based on size indicating that larger bubbles have higher sliding velocities, conversing to the bulk liquid velocity. Through investigating the observed bubble characteristics, coalescence during flowing was identified as the major mechanism of large bubbles formations. The interfacial area concentration shows a close association with the heat transfer coefficient, and they were correlated by a power function. The Jakob number, the ratio of densities and the Boiling numbers have consistent relations with the bubble sizes and velocities. New correlations were proposed for predicting bubble sizes and sliding velocities as functions of these three dimensionless numbers. The suggested correlations agree with the experimental data with deviations of less than 10%.

EPT-M-2013-

MASTER THESIS

for Keunsoo Park

Stud.techn Keunsoo Park Spring 2013

Experimental study of the dispersed phase during subcooled flow boiling

*Eksperimentell studie av dispergert fase under subcooled flyt kokende***Background and objective**

The dynamic phase, which governs the interfacial terms between the two phases, plays a major role in the prediction of subcooled boiling flow. A population of bubbles of different sizes can be observed. This population is controlled for several parameters such as operational conditions, fluid properties, etc. A common modeling approach for describing the dynamic of the dispersed phase is the population balance equation. This equation provides a details description of the different kind of interactions of the dispersed phase such as breakage, coalescence, evaporation and condensation. However its applicability is rather limited as the large uncertainty in the available models.

In this work, an experimental and modeling work will be performed for developing suitable models for a population balance framework for a boiling tube. High speed visualization will be used for obtaining bubble size distribution under different parameters. The proposed models will be calibrated with the obtained experimental data.

The following tasks are to be considered:

- 1 Literature review on the modelling of subcooled boiling using the population balance framework.
- 2 Setting the models for the population balance model, and identification of the parameters that can be obtained from the rig.
- 3 Setting of the experiment, data acquisition, error analysis, and data processing
- 4 Evaluation of the sensitivity of the developed models

-- ” --

Within 14 days of receiving the written text on the master thesis, the candidate shall submit a research plan for his project to the department.

When the thesis is evaluated, emphasis is put on processing of the results, and that they are presented in tabular and/or graphic form in a clear manner, and that they are analyzed carefully.

The thesis should be formulated as a research report with summary both in English and Norwegian, conclusion, literature references, table of contents etc. During the preparation of the text, the candidate should make an effort to produce a well-structured and easily readable report. In order to ease the evaluation of the thesis, it is important that the cross-references are correct. In the making of the report, strong emphasis should be placed on both a thorough discussion of the results and an orderly presentation.

The candidate is requested to initiate and keep close contact with his/her academic supervisor(s) throughout the working period. The candidate must follow the rules and regulations of NTNU as well as passive directions given by the Department of Energy and Process Engineering.

Risk assessment of the candidate's work shall be carried out according to the department's procedures. The risk assessment must be documented and included as part of the final report. Events related to the candidate's work adversely affecting the health, safety or security, must be documented and included as part of the final report. If the documentation on risk assessment represents a large number of pages, the full version is to be submitted electronically to the supervisor and an excerpt is included in the report.

Pursuant to "Regulations concerning the supplementary provisions to the technology study program/Master of Science" at NTNU §20, the Department reserves the permission to utilize all the results and data for teaching and research purposes as well as in future publications.

The final report is to be submitted digitally in DAIM. An executive summary of the thesis including title, student's name, supervisor's name, year, department name, and NTNU's logo and name, shall be submitted to the department as a separate pdf file. Based on an agreement with the supervisor, the final report and other material and documents may be given to the supervisor in digital format.

Work to be done in lab (Water power lab, Fluids engineering lab, Thermal engineering lab)
 Field work

Department of Energy and Process Engineering, 16. January 2013

Olav Bolland
Department Head

Carlos A. Dorao
Academic Supervisor

Research Advisors: Ezequiel Manavela Chiapero
Han Deng

Acknowledgements

This master thesis was written during stay in NTNU as an master exchange student in Energy and Processing Department at Norwegian University of Science and Technology.

First, I would like to express my gratitude to my advisor Carlos Alberto Dorao. Despite of my sudden request for collaborative research, he sincerely welcomed me and supported my research. Sometimes I was sick of the experiments and had trouble adjusting new environment, your passion provoked me to go back to work.

And my supervisor, Ezequiel Manavela Chiapero, always be with me and help my project. Your concern by asking my progress and challenge was great encouragement to me. Discussion with you was also beneficial. I am happy to keep up working with you.

In addition, the existence of Luis, who is doing a master project with me, triggered me. Your gorgeous background and passion on the research was impressive.

Lastly, I also want to thank to my advisor, Daejun Chang, in South Korea who admitted me to go to NTNU and financially supported me. It was great opportunity for me to experience new world.

Nomenclature

| | |
|----------|--|
| A_b | measured area occupied by bubble image in pixel |
| A_i | inner cross-section area of tube = $1.964\text{E-}05 \text{ m}^2$ |
| a_i | interfacial area concentration [mm^{-1}] |
| Bo | Boiling number |
| $B(x)$ | type 1 distribution function |
| $B_n(x)$ | normalized type 1 distribution function |
| C_{pf} | heat capacity of liquid [$\text{J/kg}^\circ\text{C}$] |
| C_r | slip ratio |
| Co | Confinement number |
| CF | correction factor |
| D_i | inner tube diameter = 0.005 m |
| D_o | outer tube diameter = 0.008 m |
| d_a | bubble diameter in equivalent circular area [mm] |
| d_i | bubble diameter of i-th subgroup [mm] |
| d_m | modal diameter of the large bubble group [mm] |
| d_m^+ | dimensionless $d_m \times 10^3$ |
| d_p | bubble departure diameter [mm] |
| d_p^+ | dimensionless $d_p \times 10^3$ |
| d_{pe} | bubble diameter in equivalent circular perimeter [mm] |
| E | mean deviation between the size distribution and type 1 distribution |
| f_s | size distribution |
| f_v | volume distribution |
| G | mass flow rate [$\text{kg/m}^2\text{s}$] |

| | |
|-----------|--|
| g | acceleration due to gravity = 9.81 m/s^2 |
| h | local heat transfer coefficient [$\text{W/m}^2\text{K}$] |
| I | current [A] |
| i_{fg} | latent heat [J/kg] |
| Ja | Jakob number |
| K_p | distance between adjacent pixel [mm/pixel] |
| Ku | kurtosis of small bubble group |
| k_f | thermal conductivity of liquid [W/mK] |
| k_w | thermal conductivity of wall [W/mK] |
| L | tube length = 2 m |
| N_b | number of redundantly counted bubbles |
| N_c | number of counted images |
| N_{pop} | bubble population [mm^{-3}] |
| N_u | number of uncounted images |
| $N(d_i)$ | number of bubbles with diameter of i -th subgroup |
| P | pump power [W] |
| P_w | power for heating tube [W] |
| Q | volumetric flow rate [m^3/s] |
| q | heat flux [kW/m^2] |
| q'' | volumetric heat transfer [kW/m^3] |
| Re | Reynold number |
| r | radial coordinate |
| S | suppression factor |
| S_v | total volume of redundantly counted images |
| $T_{f,i}$ | tube inlet temperature [$^\circ\text{C}$] |

| | |
|------------------|--|
| T_{sat} | saturation temperature [$^{\circ}C$] |
| T_{wi} | inner wall temperature [$^{\circ}C$] |
| T_{wo} | outer wall temperature [$^{\circ}C$] |
| t_i | initial time [s] |
| t_f | final time [s] |
| ΔT_{sub} | inlet subcooling [$^{\circ}C$] |
| ΔT_{sat} | wall superheating [$^{\circ}C$] |
| Δt | time interval [s] |
| V | voltage [V] |
| \dot{V}_i | tube inlet volumetric flow rate [l/min] |
| v_b | bubble velocity [mm/s] |
| \bar{v}_b | average bubble sliding velocity [mm/s] |
| x | variable in function or horizontal position of mass center of bubble |
| x_{outlet} | outlet quality |
| y | vertical position of mass center of bubble [mm] |
| z | tube axial coordinate |

Greek letters

| | |
|-------------|--|
| α | void fraction |
| β_1 | skewness |
| β_2 | kurtosis |
| κ | criterion for determining types of Person's system |
| μ_1 | first moment, average bubble diameter |
| μ_2 | second moment |
| $\mu_{2,l}$ | variance of the large bubble group |
| μ_3 | third moment |

| | |
|--------------|--|
| μ_4 | fourth moment |
| μ_f | dynamic viscosity of liquid [<i>Pa.s</i>] |
| ρ | density [<i>kg/m³</i>] |
| $\Delta\rho$ | density difference [<i>kg/m³</i>] |
| σ | surface tension [<i>N/m</i>] |

Subscripts

| | |
|------------|---|
| <i>a</i> | equivalent circular area |
| <i>b</i> | bubble |
| <i>c</i> | counted |
| <i>f</i> | liquid phase, final |
| <i>fg</i> | latent |
| <i>i</i> | initial, inner, index for bubble size subgroup |
| <i>l</i> | large bubble group |
| <i>m</i> | mode |
| <i>n</i> | normalized distribution |
| <i>o</i> | outer |
| <i>p</i> | equivalent circular perimeter, departure, pixel |
| <i>pop</i> | population |
| <i>r</i> | ratio |
| <i>s</i> | bubble size, small bubble group |
| <i>sat</i> | saturated state |
| <i>sub</i> | subcooling |
| <i>TP</i> | two-phase |
| <i>V</i> | Volume |
| <i>w</i> | heated wall |

Table of Contents

| | |
|---|----|
| 1 Introduction | 1 |
| 2 Experimental facility and procedures | 5 |
| 2.1 Experimental facility | 5 |
| 2.1.1 Main components of the test loop..... | 7 |
| 2.1.2 Heated section | 9 |
| 2.1.3 Visualization section | 10 |
| 2.1.4 Measurements and accuracy..... | 12 |
| 2.2 Experiment procedures | 15 |
| 2.2.1 Hysteresis loop | 15 |
| 2.2.2 Assurance for stable experimental conditions..... | 18 |
| 2.2.3 Consistency of experimental results..... | 20 |
| 2.3 Experimental conditions | 21 |
| 2.3.1 Restriction on the freedom of selecting experimental conditions | 21 |
| 2.3.2 Mass flow rate and inlet subcooling matrix | 24 |
| 2.3.3 Heat flux | 27 |
| 2.3.4 Power..... | 28 |
| 2.3.5 Coupling effect of inlet subcooling and heat flux | 29 |
| 3 Data processing | 31 |
| 3.1 Image analysis | 31 |
| 3.1.1 Image analysis algorithm | 31 |
| 3.1.2 Measurements of bubble diameter and velocity..... | 33 |

| | |
|--|--------|
| 3.1.3 Correction for the number of bubbles | 34 |
| 3.2 Data reduction..... | 37 |
| 3.2.1 Basic assumption..... | 37 |
| 3.2.2 Inner wall temperature | 37 |
| 3.2.3 Wall temperature and liquid temperature profiles..... | 38 |
| 3.2.4 Pearson's system | 40 |
| 3.2.5 Data bank structure..... | 42 |
| 4 Results and discussion..... | 51 |
| 4.1 Phenomenological analysis of bubble characteristics..... | 51 |
| 4.2 The influence of single parameter on bubble characteristics..... | 62 |
| 4.2.1 Mass flow rate and inlet subcooling..... | 62 |
| 4.2.2 Heat flux | 74 |
| 4.2.3 Pressure | 77 |
| 4.3 Coupling effect of heat flux and inlet subcooling on bubble characteristics..... | - 84 - |
| 4.4 Relation between heat transfer and bubble characteristics | - 87 - |
| 4.5 Correlation equations..... | - 92 - |
| 4.5.1 Relevant dimensionless numbers to bubble characteristics | - 92 - |
| 4.5.2 Correlation equations for predicting bubble characteristics..... | - 95 - |
| 5 Conclusion..... | - 97 - |
| 6 Reference..... | - 99 - |

List of Figures

| | |
|--|----|
| Figure 1 Scheme of the experimental facility [22] | 6 |
| Figure 2 Main components of the test loop [23]..... | 8 |
| Figure 3 Heated section | 9 |
| Figure 4 Visualization section [23]..... | 11 |
| Figure 5 High-speed camera with laser | 12 |
| Figure 6 Software interface to control the experimental facility | 13 |
| Figure 7 Hysteresis loop in the boiling curve measured at the ninth wall thermocouple..... | 16 |
| Figure 8 Example of acceptable experimental conditions | 19 |
| Figure 9 Recorded experimental conditions of set 1 (top) and set 2 (bottom) | 26 |
| Figure 10 Example of image processing, before (left) and after (right) | 32 |
| Figure 11 Dismissed bubble due to its cut shape..... | 35 |
| Figure 12 Temperature profiles of inner wall and bulk liquid..... | 39 |
| Figure 13 Modal diameter of the large bubble group | 45 |
| Figure 14 Representative size distribution obtained at $P = 7.7 \text{ bar}$, $G = 300 \text{ kg/m}^2\text{s}$, $\Delta T_{sub} = 35.0^\circ \text{C}$, and $q = 7.64 \text{ kW/m}^2$ | 52 |
| Figure 15 Typical bubble flowing patterns at $G = 300 \text{ kg/m}^2\text{s}$ (left) and $500 \text{ kg/m}^2\text{s}$ (right) | 53 |
| Figure 16 Typical size-velocity diagram measured at $G = 500 \text{ kg/m}^2\text{s}$ | 53 |
| Figure 17 Observed bubble coalescence in flowing, diameter of front bubble: 2.34, rear bubble: 3.87, and after coalescence: 4.64 mm..... | 55 |
| Figure 18 Collection of the size distributions with increasing mass flow rate from 300 to 340 $\text{kg/m}^2\text{s}$, adjusting $P = 7.7 \text{ bar}$, $\Delta T_{sub} = 34.0^\circ \text{C}$, and $q = 7.64 \text{ kW/m}^2$ | 58 |
| Figure 19 Bubble population at $\Delta T_{sub} = 35.0^\circ \text{C}$, $P = 7.7 \text{ bar}$, and $q = 13.21 \text{ kW/m}^2$ | 61 |
| Figure 20 Imaginary frequencies of bubble departure and coalescence in flowing | 61 |
| Figure 21 Average bubble diameters with respect to mass flow rate and inlet subcooling around $G = 300$ (left) and $500 \text{ kg/m}^2\text{s}$ (right)..... | 63 |
| Figure 22 Size distributions around $G = 300$ (left) and $500 \text{ kg/m}^2\text{s}$ (right) at $\Delta T_{sub} = 35.0^\circ \text{C}$ | 63 |

| | |
|--|----|
| Figure 23 Volume distributions around $G = 300$ (left) and $500 \text{ kg/m}^2\text{s}$ (right) at $\Delta T_{sub} = 35.0^\circ \text{C}$ | 63 |
| Figure 24 Mode of large bubble group with respect to mass flow rate and inlet subcooling around $G = 300$ (left) and $500 \text{ kg/m}^2\text{s}$ (right) | 65 |
| Figure 25 Mode of large bubble group with respect to wall superheating around $G = 500 \text{ kg/m}^2\text{s}$ | 65 |
| Figure 26 Mode of large bubble group with respect to predicted ONB location around $G = 500 \text{ kg/m}^2\text{s}$ | 65 |
| Figure 27 Bubble population with respect to mass flow rate and inlet subcooling around $G = 300$ (left) and $500 \text{ kg/m}^2\text{s}$ (right)..... | 66 |
| Figure 28 Bubble population with respect to wall superheating around $G = 500 \text{ kg/m}^2\text{s}$ | 67 |
| Figure 29 Interfacial area concentration with respect to mass flow rate and inlet subcooling around $G = 300$ (left) and $500 \text{ kg/m}^2\text{s}$ (right)..... | 68 |
| Figure 30 Void fraction with respect to mass flow rate and inlet subcooling around $G = 300$ (left) and $500 \text{ kg/m}^2\text{s}$ (right)..... | 68 |
| Figure 31 Relation between void fraction and predicted OSV location with respect to mass flow rate and inlet subcooling around $G = 300$ (top) and $500 \text{ kg/m}^2\text{s}$ (bottom) | 69 |
| Figure 32 Variance of large bubble group with respect to mass flow rate and inlet subcooling around $G = 300$ (left) and $500 \text{ kg/m}^2\text{s}$ (right)..... | 71 |
| Figure 33 Kurtosis of small bubble group with respect to mass flow rate and inlet subcooling around $G = 300$ (left) and $500 \text{ kg/m}^2\text{s}$ (right) | 71 |
| Figure 34 Kurtosis with respect to wall superheating with respect to mass flow rate and inlet subcooling around $G = 500 \text{ kg/m}^2\text{s}$ | 72 |
| Figure 35 Relation between kurtosis of small bubble group and predicted OSV location mass flow rate and inlet subcooling around $G = 500 \text{ kg/m}^2\text{s}$ | 72 |
| Figure 36 Average sliding bubble velocities and bulk liquid velocities with respect to mass flow rate and inlet subcooling around $G = 300$ (left) and $500 \text{ kg/m}^2\text{s}$ (right)..... | 73 |
| Figure 37 Average bubble diameter and mode of large bubble group with respect to heat flux at $G = 300$ (left) and $500 \text{ kg/m}^2\text{s}$ (right)..... | 76 |
| Figure 38 Population, interfacial area concentration, and void fraction with respect to heat flux at $G = 300$ (left) and $500 \text{ kg/m}^2\text{s}$ (right) | 76 |
| Figure 39 Variance of large bubble group and kurtosis of small bubble group with respect to heat flux at $G = 300$ (left) and $500 \text{ kg/m}^2\text{s}$ (right)..... | 76 |

| | |
|--|--------|
| Figure 40 Average sliding bubble velocity and bulk liquid velocity with respect to heat flux at $G = 300$ (left) and $500 \text{ kg/m}^2\text{s}$ (right)..... | 77 |
| Figure 41 Captured images at $q = 7.64$ (left) and 7.83 kW/m^2 (right) | 77 |
| Figure 42 Average bubble diameter (left) and mode of large bubble group (right) with respect to pressure at $G = 300$ and $500 \text{ kg/m}^2\text{s}$ | 79 |
| Figure 43 Variance of large bubble group (left) and kurtosis of small bubble group (right) with respect to pressure at $G = 300$ and $500 \text{ kg/m}^2\text{s}$ | 79 |
| Figure 44 Population, interfacial area concentration, and void fraction with respect to pressure at $G = 300$ (left) and $500 \text{ kg/m}^2\text{s}$ (right) | 80 |
| Figure 45 Average sliding bubble velocity and bulk liquid velocity with respect to pressure at $G = 300$ (left) and $500 \text{ kg/m}^2\text{s}$ (right)..... | 80 |
| Figure 46 Predicted ONB and OSV location with respect to pressure at $G = 500 \text{ kg/m}^2\text{s}$ | 81 |
| Figure 47 Wall superheating with respect to pressure at $G = 500 \text{ kg/m}^2\text{s}$ | 82 |
| Figure 48 Average bubble diameter and mode of large bubble size with respect to heat flux and inlet subcooling at $G = 300$ (left) and $500 \text{ kg/m}^2\text{s}$ (right) | - 85 - |
| Figure 49 Population, interfacial area concentration, and void fraction with respect to heat flux and inlet subcooling at $G = 300$ (left) and $500 \text{ kg/m}^2\text{s}$ (right)..... | - 85 - |
| Figure 50 Average bubble sliding velocity and bulk liquid velocity with respect to heat flux and inlet subcooling at $G = 300$ (left) and $500 \text{ kg/m}^2\text{s}$ (right) | - 85 - |
| Figure 51 Increase of wall superheating with increasing heat flux and decreasing inlet subcooling | - 86 - |
| Figure 52 Average bubble diameter and mode of large bubble group with respect to outlet qualities from experimental set 1 | - 86 - |
| Figure 53 Local heat transfer coefficient with respect to mass flow rate and inlet subcooling around $G = 300$ (left) and $500 \text{ kg/m}^2\text{s}$ (right) | - 88 - |
| Figure 54 Local heat transfer coefficient with respect to heat flux at $G = 300$ (left) and $500 \text{ kg/m}^2\text{s}$ (right) | - 88 - |
| Figure 55 Local heat transfer with respect to pressure at $G = 300$ and $500 \text{ kg/m}^2\text{s}$ | - 88 - |
| Figure 56 Local heat transfer coefficient with respect to outlet quality from experimental set 1 and 2 at $G = 300$ (left) and $500 \text{ kg/m}^2\text{s}$ (right)..... | - 89 - |
| Figure 57 Effect of mass flow rate on the relation between local heat transfer coefficient and outlet quality from experimental set 1 and 2 around $G = 300$ (left) and $500 \text{ kg/m}^2\text{s}$ (right) | - 89 - |

Figure 58 Local heat transfer coefficient with respect to bubble population from experimental set 1 and 2 around $G = 300$ (left) and $500 \text{ kg/m}^2\text{s}$ (right) - 91 -

Figure 59 Local heat transfer coefficient with respect to interfacial area concentration with respect to mass flow rate and inlet subcooling (first row), heat flux (second row), and pressure (third row) at $G = 300$ (left) and $500 \text{ kg/m}^2\text{s}$ (right) - 91 -

Figure 60 Relevance of Jakob number, Boiling number and ratio of densities to dimensionless mode of large bubble group (left) and slip ratio (right) - 94 -

Figure 61 Comparison between predicted and measured dimensionless mode of the large bubble group - 96 -

Figure 62 Comparison between predicted and measured slip ratio - 96 -

List of Tables

| | |
|---|--------|
| Table 1 Accuracy of measurements | 14 |
| Table 2 Different flow patterns under the same conditions according to the way of changing power | 17 |
| Table 3 Allowable fluctuations of the operating conditions | 19 |
| Table 4 Experimental conditions of mass flow rate and inlet subcooling matrix, set 1 and 2 | 25 |
| Table 5 Experimental conditions with varying heat flux, set 3 and 4..... | 27 |
| Table 6 Experimental conditions of varying pressure, set 5 and 6 | 28 |
| Table 7 Experimental conditions of coupling effects in set 7..... | 30 |
| Table 8 Experimental conditions of coupling effects in set 8..... | 30 |
| Table 9 Correction factors for number of bubbles..... | 36 |
| Table 10 Photos of bubbles varying operating conditions from the basic ones: $P = 7.7 \text{ bar}$ and $\Delta T_{sub} = 35.0 \text{ }^\circ\text{C}$ | - 83 - |
| Table 11 Coefficient and power of the interpolated equation..... | - 90 - |
| Table 12 Dimensionless numbers as candidates for correlation equations | - 93 - |
| Table 13 Coefficients of correlation equations (56) | - 95 - |

1 Introduction

The dynamic phase, which governs the interfacial transport between the two phases, plays a major role in the prediction of a subcooled boiling flow. A common modeling approach for describing the dynamics of the dispersed phase is the population balance equation. This equation provides a detailed description of the various interactions of the dispersed phase, including breakage, coalescence, evaporation, and condensation [1, 2]. However, its applicability is rather limited due to a lack of experimental data concerning the bubble behaviors, which could reduce the large uncertainty in the available models.

Flow boiling heat transfer has been widely used in the design of highly compact subsea heat exchangers. Subcooled flow boiling in these apparatuses can further improve their energy efficiencies because of its significant heat-transfer enhancement properties [3]. To develop a rigid calculation model for a compact subsea heat exchanger, detailed information on the bubble characteristics and associated heat transfer is required [4, 5].

Since the first photographic study was performed by F. C. Gunther et al. [6], revealing the parametric influences on bubble size, lifespan, and population, a considerable amount of research has been carried out to investigate the effects of pressure, inlet subcooling, mass flow rate, and heat flux on the bubble characteristics and associated heat transfer. The work of J. Garnier et al. [7], commonly called the DEBORA test, is regarded to have yielded

reliable experimental results. These researchers discovered the radial gradients of diverse bubble characteristics of R12, such as the bubble diameter, velocity, bubble density, interfacial area concentration, and void fraction, under a wide range of operating conditions [7]. The influences of various parameters on the bubble size, density, and frequency and on the heat transfer of R-134a in the horizontal channel have been partially identified by Y. M. Lie et al. [3]. V. Prodanovic et al. [8] investigated the effect of pressure on the bubble characteristics and noted that the bubble diameter depends strongly on pressure. An experimental investigation of the nucleation site density on a stainless steel surface was performed by L. Zou [9]. The reported parametric influences vary depending on the details of the experimental conditions, but generally, bubble generation is more strongly promoted at lower mass flow rates and inlet subcooling and at higher heat fluxes and pressures.

The size distribution, which has been assumed to be stochastic in nature in the majority of previous studies, has been analyzed extensively in the literature [10-12]. U. Puli et al. [10] examined the bubble size distribution of water in a horizontal annulus and focused on the change in the proportion of small bubbles in the distribution caused by manipulating the experimental conditions. R. Maurus et al. [11] extended the research on this topic by also observing the bubble lifetime and obtained similar distributions for the lifetime and size of the bubbles. Recently, a mechanical bubble size model, S_{γ} , was examined by B.J. Yun et al. [12] from the perspective of the size distribution, and the results were used to develop a suitable population balance framework and to enhance the accuracy of the predictions of subcooled flow boiling for CFD code.

Sliding bubble characteristics including size, velocity, and the effect of sliding on the enhancement of heat transfer, have been investigated extensively. The results from optical experiments by A. B. Ozer et al. [13] and Y. Y. Hsieh [14] demonstrated that when most of the bubbles are sliding along a heated surface, the enhancement in heat transfer with increasing heat flux can be primarily attributed to the sliding of the bubbles rather than to a greater number of activated nucleation sites. The authors also reported that downstream nucleation sites are significantly deactivated by the cooling effect of sweeping bubbles. S. Li et al. [15] studied the effects of various parameters on bubble size and sliding velocity and reported an increase in bubble sliding velocity as inlet subcooling decreased despite a constant flow rate. By collecting the experimental results from the literature, G. Sateesh et al. [16] proposed correlations for the heat transfer coefficients of sliding bubbles. N. Basu et al. [17, 18] categorized the initial bubble sliding according to bubble merging during sliding and suggested distinct correlations for heat transfer reflecting different mechanisms in different categories. B. Donnelly et al. [19] identified two main mechanisms for the improvement of heat transfer caused by bubble sliding: the sliding bubble acting as a blurry body and the generated wake resulting in mixing.

Two photographic studies have been conducted in which the operating conditions were nearly identical to those of the present experiments in terms of parameters, tube geometries, and fluid properties [20, 21]. However, the experiment described in M. Lin et al. [20] was carried out in a horizontal plate with complex geometry instead of in a horizontal channel,

and the inlet subcooling and pressure in the experiment of C.P. Yin et al. [21] were considerably lower than those in this study.

Therefore, the heat transfer and associated bubble characteristics in the downstream region of a horizontal channel, which is characterized by a wide spread in the size distribution and the coalescence of the sliding bubbles, have not been fully explored, particularly for the new refrigerant R-134a. The present study provides experimental data on the subcooled flow boiling of R-134a at mass flow rates of approximately 300 and 500 kg/m^2s , inlet subcooling ranging from 20.0 to 36.0 °C, heat fluxes varying from 4.07 to 13.21 kW/m^2 , and pressures from 4.7 to 7.7 *bar*. The experiments were carried out with a horizontal, annular heated channel with an inner diameter of 5 *mm*, and a high-speed camera at a rate of 500 frames/s was used to record the bubble characteristics at the end of the heated tube. After the raw data were processed according to the objectives of the analysis, they were collected in a data bank, including the bubble characteristics, heat transfer, and operating conditions, and the parametric effects on the data were investigated. Through phenomenological analysis of the data, some deductions were made concerning the interaction of the dispersed phase, which could not be observed directly. A method of interpolating the measured size distributions was proposed for use in developing a population balance framework in a future study. The bubble characteristics, which are closely related to the heat transfer coefficients, were identified and correlated. New correlation equations for bubble sizes and velocities were proposed; these equations are written in terms of appropriate dimensionless numbers.

2 Experimental facility and procedures

2.1 Experimental facility

The experimental facility had been mainly designed by E.M. Chiapero and L.C. Ruspini in NTNU and the detail description is included in L.C. Ruspini [22]. The working fluid in the loop is R-134a which is easy to handle thanks to its low boiling point and low latent heat.

The facility can be operated within the following parameter regions:

- Mass flow rate: 5–2000 kg/m^2s
- Inlet temperature: -20–40 °C, Inlet subcooling: 0–50 °C
- Heating power: 0–2 kW
- System pressure: 4–10 bar

Figure 1 is the P&ID of the facility and all the main components and their configurations are sketched.

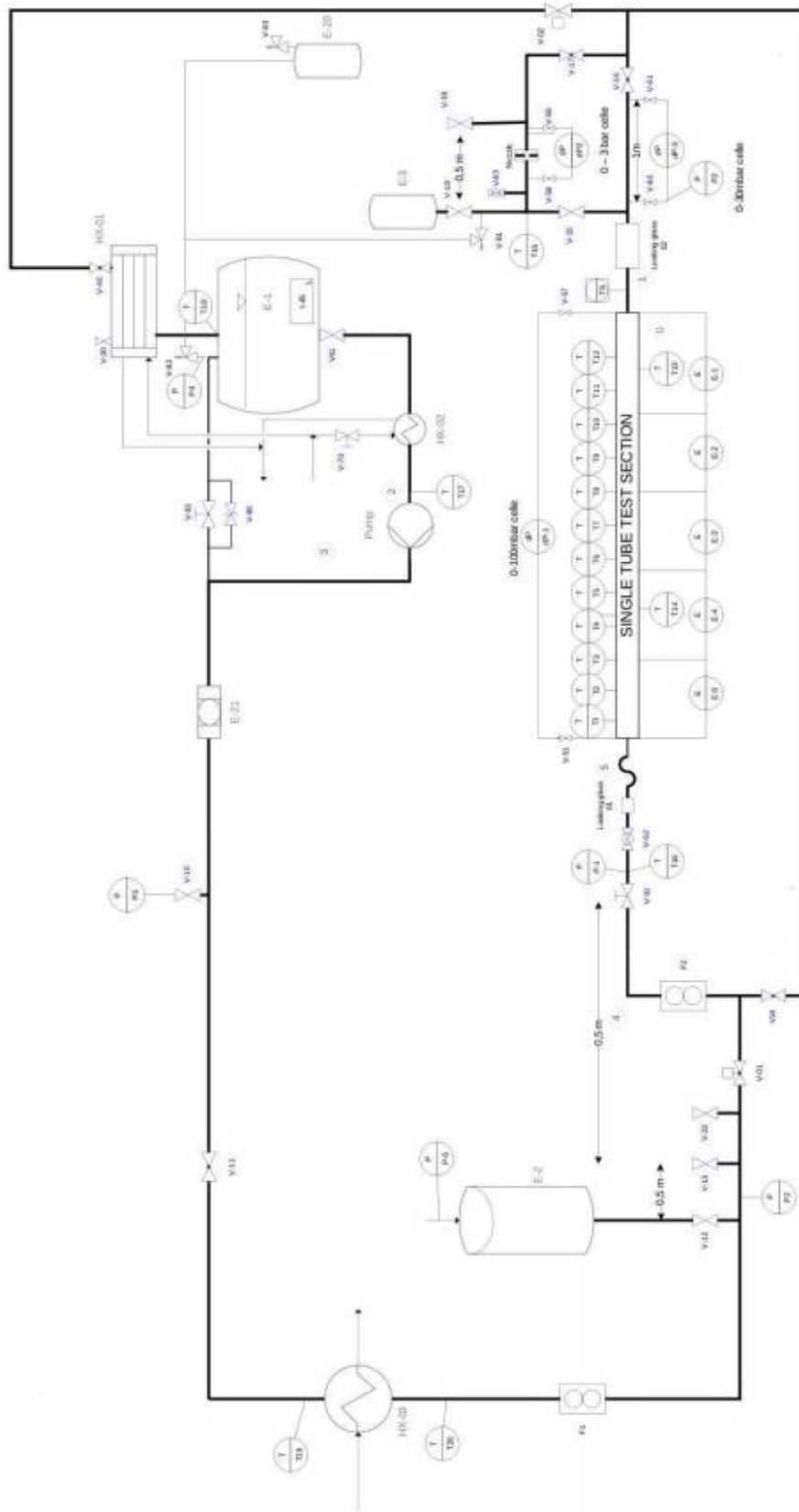


Figure 1 Scheme of the experimental facility [22]

2.1.1 Main components of the test loop

The test loop consists of the following main components:

- Main storage tank
- Pump: a gear pump with a magnetic drive coupling
- Conditioner: K9 model, plate-fin heat exchanger with glycol and water
- Condenser: K6 model, shell and tube heat exchanger with glycol and water

The configuration of the main components in the facility is presented in Figure 2 [23].

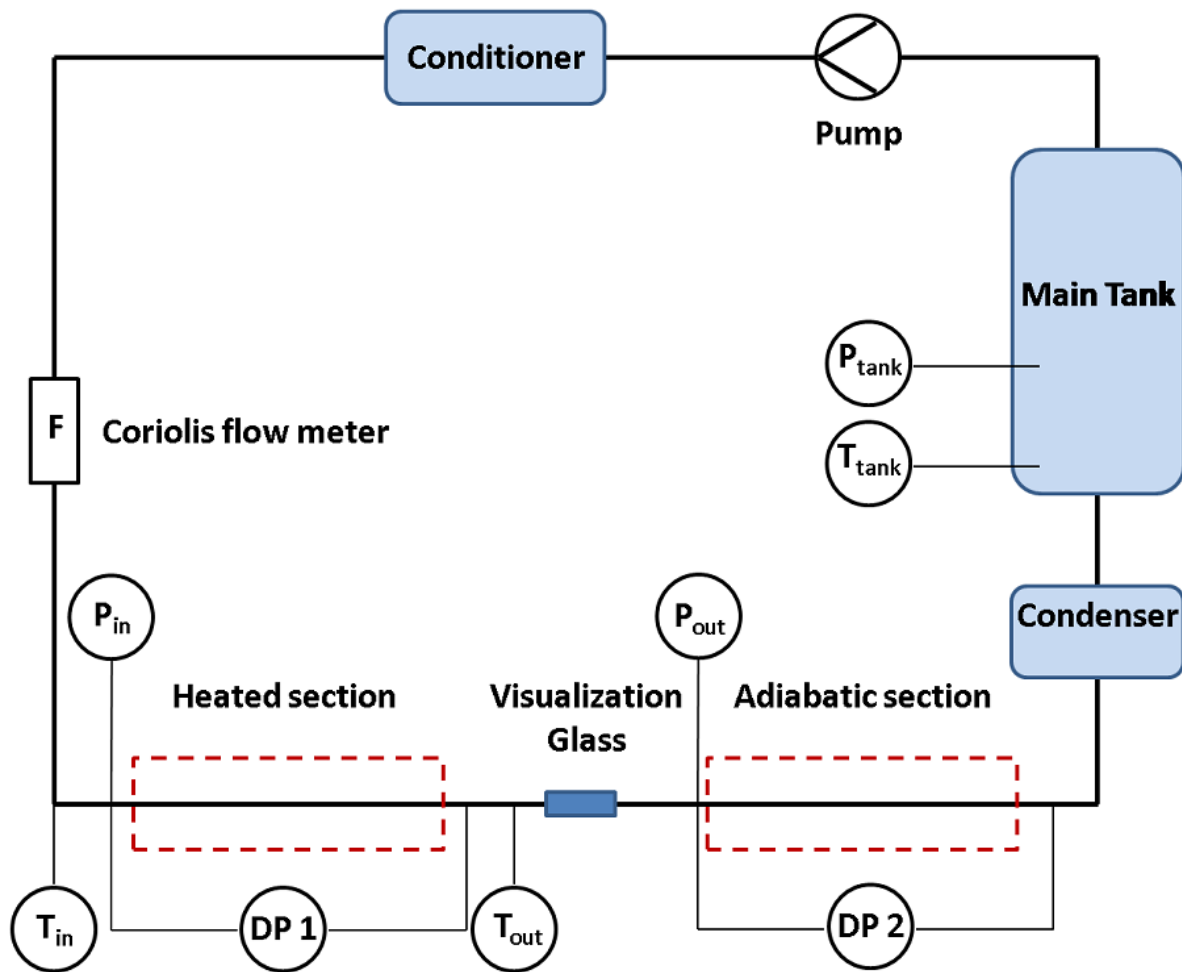


Figure 2 Main components of the test loop [23]

The four noticeable experimental conditions in the present study, mass flow rate, inlet subcooling, heat flux, and pressure can be controlled as following: Mass flow rate is determined by setting the power of the gear pump. The R-134a inlet temperature of the heated section is adjusted by controlling the temperature of refrigerant in the shell side of the conditioner. Main storage tank is filled with large volume of saturated R-134a, playing a role as a buffer by providing the stable flow condition. Operating pressure of the loop is tuned by manipulating the fluid temperature in the tank which is adjusted by the condenser.

The power of the pump, temperature of circulating fluid in the conditioner and condenser and input heat flux can be manually manipulated from the interface software.

2.1.2 Heated section

A heated section is divided into five segments, where the imposed heat flux can be controlled independently. Each segment is 0.4 m long stainless steel pipe with 5 mm and 8 mm of inner and outer tube diameter respectively.

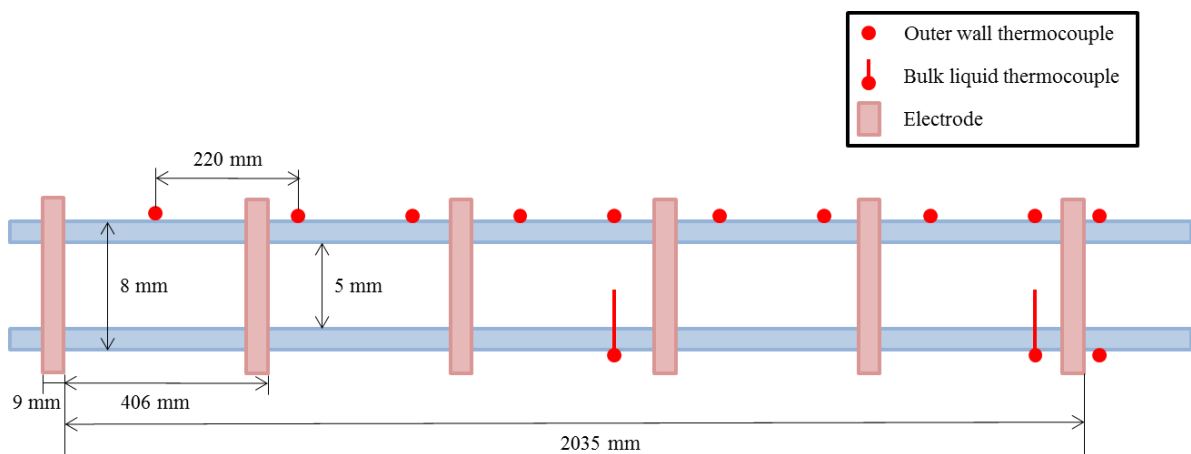


Figure 3 Heated section

Heat is applied to the working fluid electrically by Joule effect. Low voltage and high current of electric power are converted to the heat flux. Even though a controller-rectifier circuit converts AC to DC, the values of voltage and current are the functions of time. The electrical power is given by

$$P_w = \frac{\int_{t_i}^{t_f} I(t)V(t)dt}{(t_f - t_i)}. \quad (1)$$

The expression for the input heat flux q can be derived with the assumptions of perfect insulation, uniform heat flux along the whole tube and no heat loss in heat transfer from heater to the fluid in the tube as the equation (2).

$$q = \frac{P_w}{\pi D_i L} \quad (2)$$

2.1.3 Visualization section

The visualization glass is located just after the heated section and high-speed camera takes bubble images from side view. The section is 20 cm long transparent glass with 5 mm and 8 mm of inner and outer diameter respectively as shown in Figure 4.

The criterion was proposed by P.A. Kew et al. [24] for a microchannel, which is based on the value of the confinement number and it is defined as the equation (3).

$$Co = \frac{1}{D_i} \sqrt{\frac{\sigma}{g(\rho_f - \rho_g)}} \quad (3)$$

If the confinement number is greater than 0.5 under the operating conditions, it indicates characteristics of microchannel will be shown in the conditions. The experiments conducted in the present study have low confinement number, 0.1735 at maximum, due to large tube

diameter, thus the flow in the tube will show the characteristics of flow in the conventional size of tube, not narrow tube.



Figure 4 Visualization section [23]

Bubbles are filmed by the high-speed camera (Photron - FastCam SA3) with a laser (Oxford lasers - Firefly). In Figure 5, the gray object in the center is the high-speed camera and the red box is the laser. The whole visualization section is enclosed by black box for preventing the optical danger by the laser. The bubble images were taken at 500 frames/s of camera shutter speed in the 1000×450 pixels, which corresponds to a 16.18×7.4 mm window in reality. The pulse duration of laser is set at its maximum value for gaining both high brightness and high resolution as much as possible. The maximum duration is

determined according to the shutter speed of the camera, as a trigger source, and the maximum value is $20\mu s$ in this experiments.

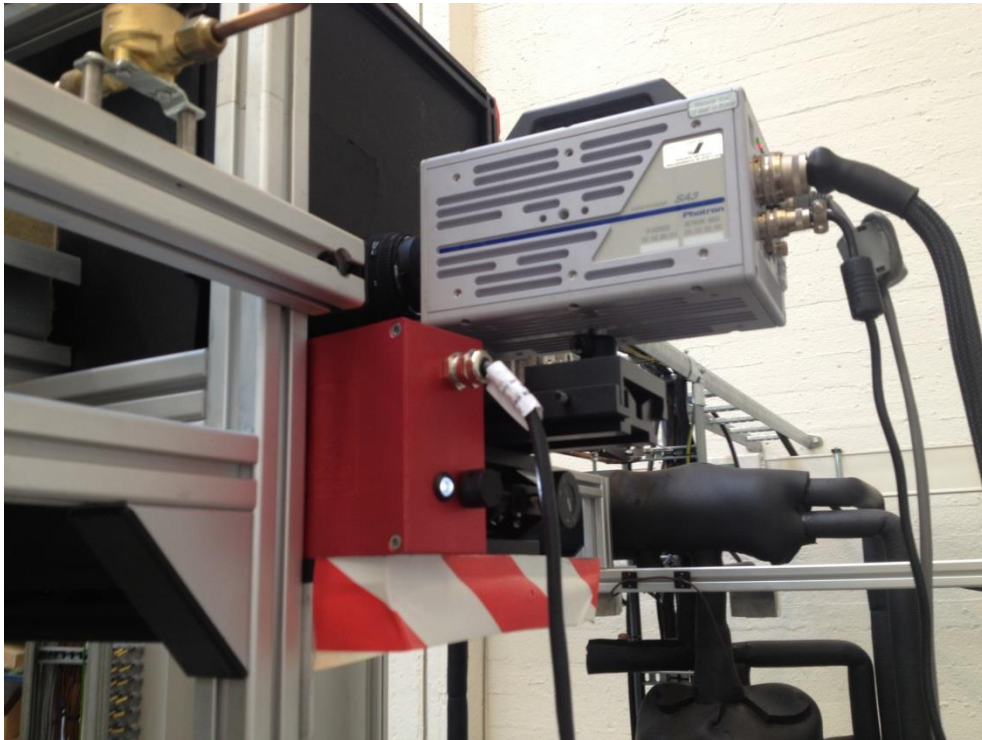


Figure 5 High-speed camera with laser

2.1.4 Measurements and accuracy

As the top-right legend in Figure 6, absolute pressure [*bar*], differential pressure [*kPa*], volumetric flow rate [*l/min*], temperature [$^{\circ}C$], and power [*W*] are measured during experiments. Absolute pressure at the inlet and outlet of the tube, in the tank, and a surge

tank are measured by the absolute pressure transducers. And differential pressure transducers are situated at in the heated section, inlet and outlet pressure-reducing valve. Thermocouples are located at the main tank, before and after the conditioner and the heated section. In addition, as shown in Figure 3, outer wall temperature are measured at nine points and bulk liquid temperature in the tube are also recorded at two different points. Two flow meters are equipped to measure the volumetric flow rate at the inlet of heated section and the outlet of the conditioner. Power is calculated from the measured voltage and current for the five each section.

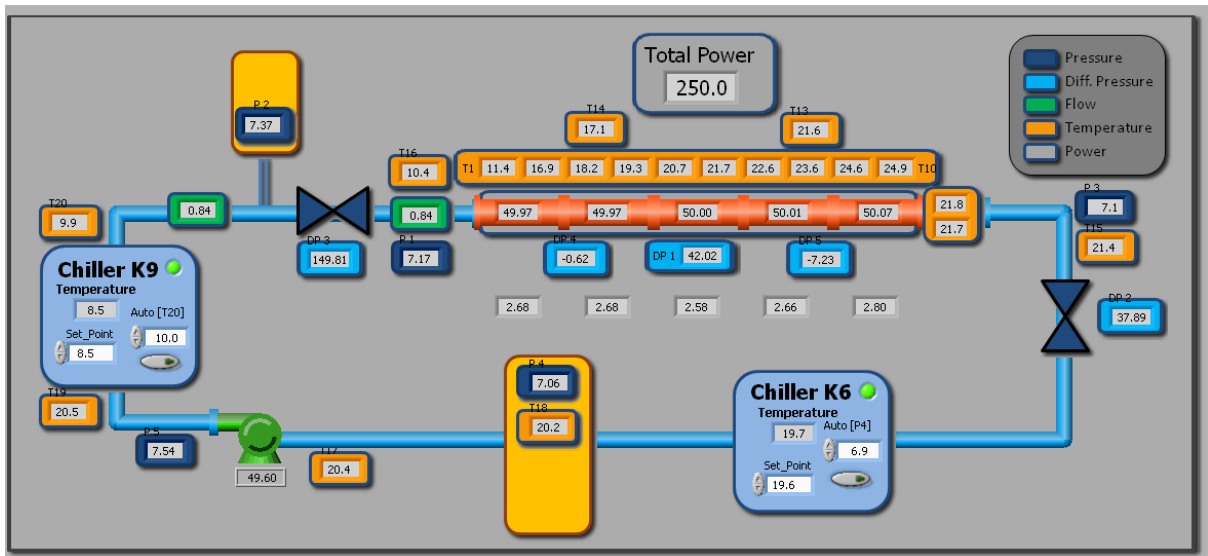


Figure 6 Software interface to control the experimental facility

The accuracies of the measurements are given by the suppliers of each device. The accuracies of the instruments and the maximum statistical error are listed in Table 1.

Table 1 Accuracy of measurements

| Instrument type | Range | Accuracy | Max. Statistical error |
|-------------------|--------------|------------|------------------------|
| Absolute pressure | 1 – 16 bar | 0.1 bar | < 10 mbar |
| DP-cell | 0 – 1 bar | 0.075 % | 1 – 5 mbar |
| Thermocouple | -50 – 100 °C | 0.1 °C | 0.1 °C |
| Flow-meter | 0 – 3 l/min | 0.01 l/min | < 0.01 l/min |
| Power | 0 – 2500 W | 20 W | 20 W |

2.2 Experiment procedures

Bubble characteristics, particularly the bubble sizes and number of flowing bubbles are significantly sensitive to not only the absolute value of operating conditions, but also their historical trajectories, which can affect the activation of nucleation sites. In order to ensure repeatability and consistencies of the experiments, the operating conditions should obey a strong standard of accuracy and a specific direction of varying conditions should be defined.

2.2.1 Hysteresis loop

Hysteresis loop has been reported in flow boiling in macrochannel [25-28], which is characterized by a sharp drop of wall temperature. C.P Yin et al. [21] reported that significant hysteresis happens at low pressure and high subcooling. Their experiments are about R-134a and have the similar tube diameter, mass flow rate, and heat flux with the present experiments, despite of lower inlet subcooling and pressure. Thus, somewhat hysteresis loop was expected to be occurred in the experiments. The phenomenon was demonstrated for our experimental facility in Figure 7, which is the measured wall temperature at the last wall thermocouple. The wall superheating trajectory of increasing power shows overshoot and sharp decline, while that of decreasing power has a smooth slope.

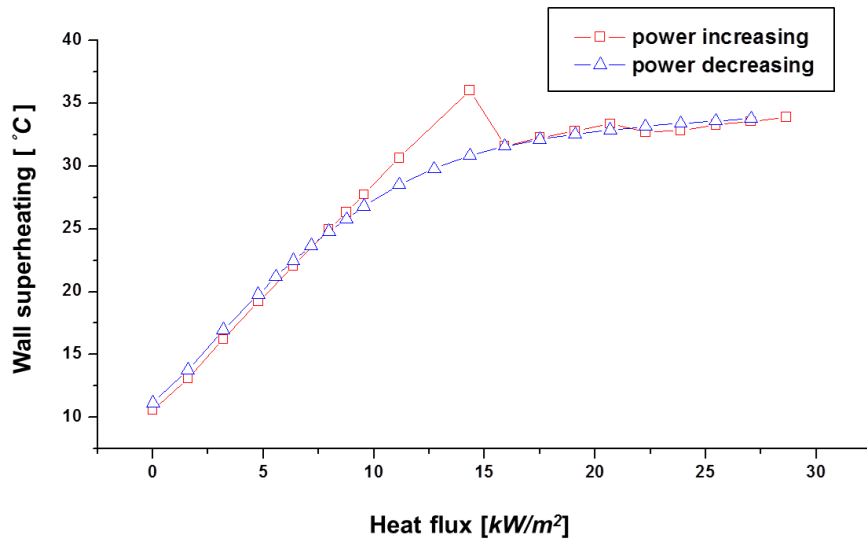
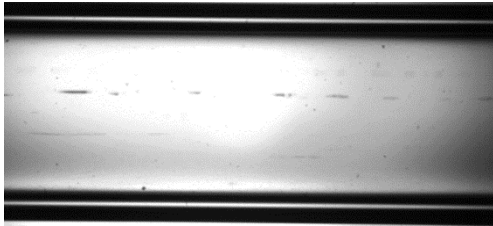
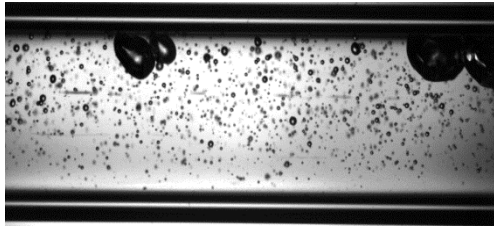
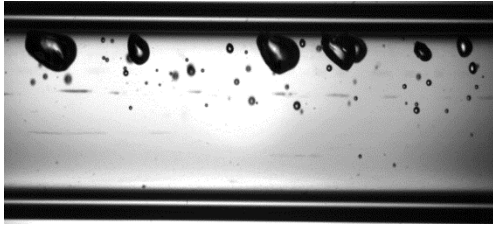
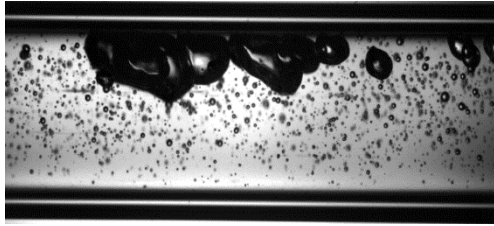
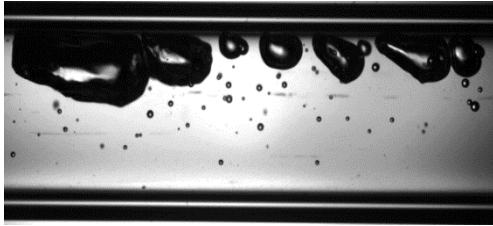
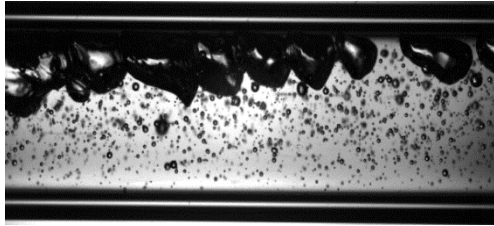


Figure 7 Hysteresis loop in the boiling curve measured at the ninth wall thermocouple

Table 2 shows several captured images during examining the hysteresis loop in the present facility. Two images in the same row were taken under the same operating conditions, but in the different way of varying power. Images were taken after confirming stabilized operating conditions based on the fixed allowable fluctuation ranges in this study, which will be provided in 2.2.2. Comparison between a pair of images gives the importance of the direction in shifting conditions to the bubble characteristics.

Table 2 Different flow patterns under the same conditions according to the way of changing power

| Q | Power increasing | Power decreasing |
|-------|--|---|
| 250 W |  |  |
| 275 W |  |  |
| 300 W |  |  |

Other three parameters except for heat flux also have the effects on the nucleation site density extensively, and similar influences of trajectories on the bubble characteristics were observed during the experiments. Consequently, in order to assure the consistencies of the experimental results, a consistent direction of changing every operating condition should be determined. In the present experiments, operating conditions always changed by following the order from more favorable bubble generation condition to less condition, i.e., the way of deactivating the nucleation sites. In other words, at all times, mass flow rate increased, subcooling went further, and heat flux and pressure decreased. This is because a sudden change in the conditions, such as wall superheating overshoot shown in Figure 7, doesn't

appear in this way of changing. When two or more operating conditions should be shifted at the same time, their varying directions could have different effects on bubble characteristics, for example increasing during flux while decreasing subcooling. In this case, bidirectional experiments were performed and data from one experiment was only selected, which was in accordance with the fundamental basis of the fixing rule, i.e., from more bubble to less.

2.2.2 Assurance for stable experimental conditions

Even though the operating conditions are stabilized, after passing oscillations in tuning time, each condition has their own inherent fluctuation according to their equipment properties. Therefore, a specific range of allowable fluctuation of the conditions should be defined in the present experiments, for providing a guidance of stable conditions. Two points were considered for defining the ranges. One is the inherent fluctuation range of each condition, which cannot be reduced after running the facility for several hours. This is because some extend of fluctuations in pump speed, imposed heat, and performances of conditioners are inevitable. The other is their influences on the experimental results. If the influence is negligible and it takes too long time to meet its inherent fluctuation range, the allowable span was slightly released for quick experiment progress. Table 3 gives the allowable fluctuations of the operating conditions which was applied to every experiment in this study.

Table 3 Allowable fluctuations of the operating conditions

| Operating conditions | Allowable fluctuations |
|-----------------------------|-------------------------------|
| P_{in} | 0.005 bar |
| ΔT_{sub} | 0.1 °C |
| G | 10 kg / m ² s |
| q | 0.01 kW / m ² |

Operating conditions in each experimental case are recorded for 360 seconds, which is the total required time for data acquisition including the videos, and only when it is confirmed the conditions are inside the allowable range, the experimental points are distinguished as reliable ones and used in analysis. Figure 8 is an example of the measured mass flow rate and inlet subcooling inside the allowable ranges. Green points are instant operating conditions recorded in 2 Hz rate and red point is the average of green points, which is stored as the operating conditions in the experimental case.

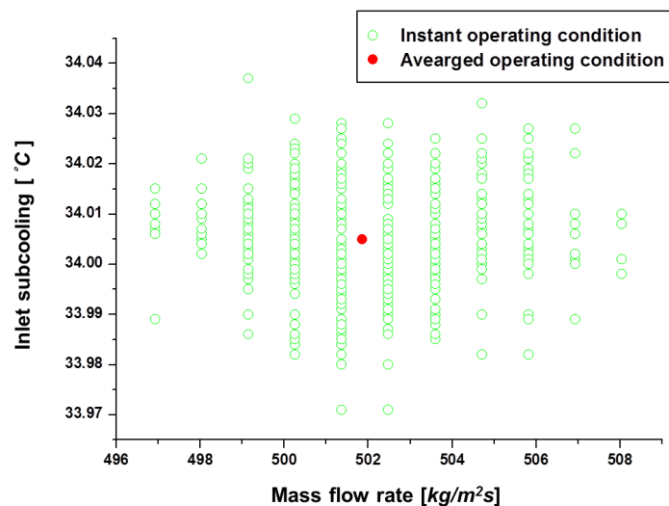


Figure 8 Example of acceptable experimental conditions

2.2.3 Consistency of experimental results

When consecutive experiments in a set were carried out over several days, with repeating turning on and off the facility, the experiment in the next day was started from the last case of previous day, not from the next case. And after confirming the coherence of two data obtained from different days, further experiments were conducted. This confirmation procedure is very important because the extent of activated nucleation sites is exceedingly sensitive to the historical variation trace of operating conditions, as aforementioned. Furthermore, different values of the unselected operating conditions as the noticeable ones in this study, such as ambient temperature, could affect to the results as well.

Despite complying with the above principles, taken bubble patterns would be different because a film is taken only for 5 seconds based on 500 frames/sec speed. Due to the inherent fluctuations in conditions, as stated in 2.2.2, the 5 seconds long video could be taken when the operating conditions are out of the average value. In order to deter a distortion in data due to these fluctuations, six videos were taken in each experimental case and the all of data in this study came from the collection of the six videos. For instance, the term, average bubble diameter, in the present study is that of every bubble in six videos. By keeping this manner, the phenomenon could be prevented that the bubble characteristics in abnormal momentary snapshot represent general aspects of bubbles in the specific operating conditions.

2.3 Experimental conditions

In the present study, four groups of experiments with distinct objectives were conducted. The first three groups are for clarifying the single parametric effect and the last one is for presenting the conjugated effects of two parameters. The variation ranges of parameters which are supposed to be constant between two adjacent cases were determined to have more than five experimental cases for each parameter variation, between two extreme bubble generation cases. For example, from $G = 500$ to $560 \text{ kg} / \text{m}^2 \text{ s}$, seven experiments with $10 \text{ kg} / \text{m}^2 \text{ s}$ interval were conducted under the same inlet subcooling $\Delta T_{sub} = 34.0 \text{ }^\circ \text{C}$. At the same time, these variation ranges were fixed to be higher than the criterion for the stable state in Table 3. The detail objectives and operating conditions are described from 2.3.2 to 2.3.5.

2.3.1 Restriction on the freedom of selecting experimental conditions

Before presenting the experimental conditions, the restrictions on the freedom of choosing them are provided. Two features mainly cause the limited range of possible experimental conditions.

At first, the inborn limitations of the experimental apparatus should be taken account of. Two allowable operating conditions of the experimental setup were primary issues in the present study.

- Working pressure should be less than 10 *bar*.
- The minimum temperature of refrigerant in the conditioner is -18 °C.
- The second clause affects the limitation on the tube inlet subcooling.

In addition, the data acquired herein are limited to specific range of operating conditions, because visualization of the bubbles is required to count each bubble accurately. If bubbles are generated too vigorously or excessively elongated bubbles, whose lengths are longer than the window, are flowing, under too much heat flux, it is difficult to visually distinguish individual bubbles. Inversely, if the heat flux is too low, single phase fluid is observed at the tube exit. Heat flux, for instance, is automatically determined after fixing other three conditions in the present experiment for avoiding visually unfeasible conditions.

Attempts of widening the interval of inlet subcooling between the conditions were intensively made on constructing a mass flow rate and inlet subcooling experiment matrix, because of its relatively high sensitivity on bubble characteristics in the present experiment settings. At first, low mass flow rate was fixed for examining the bubble coalescence and sliding. 300 kg/m^2s was chosen as the minimal mass flow rate, even though smaller flow rate is possible in the facility, due to higher sensitivity of it depending on the input power of

the pump. The pump in the experimental facility follows the affinity laws as the equation (4), which is the relation between volumetric flow rate and the input power:

$$\frac{Q_1^3}{P_1} = \frac{Q_2^3}{P_2} \quad (4)$$

Denoting the value of the equation (4) as constant k , the differential $\partial Q / \partial P$ could be expressed as $k / 3Q$. This means that the sensitivity of volumetric flow rate for changing power is higher at lower flow rate. This higher sensitivity leads to higher uncertainty in mass flow rate, because the uncertainty comes from the inherent fluctuation of pump power, as explained in 2.2.3. For these reasons, low mass flow rate is recommended in terms of uncertainty and it was fixed at $300 \text{ kg/m}^2\text{s}$ and additional experiments were carried out for $500 \text{ kg/m}^2\text{s}$.

Next, inlet subcooling was basically set at high value for reducing the variation of bubble characteristics resulting from the same amount of change in inlet subcooling. Thus, the conditioner temperature was fixed around its minimum value, $-18 \text{ }^\circ\text{C}$, for providing the lowest inlet subcooling.

And outlet quality was used for roughly determining heat flux, because outlet quality could be one of basic parameters for predicting the maximum bubble sizes. In the present study, outlet quality is estimated on heat balance as the equation (5).

$$x_{outlet} = \frac{\int_0^L q\pi D_i dz - GA_i C_{pf} \Delta T_{sub}}{GA_i i_{fg}} = \frac{\int_0^L q\pi D_i dz}{GA_i i_{fg}} - \frac{C_{pf}}{i_{fg}} \Delta T_{sub} \quad (5)$$

The approximate value of heat flux was given by the equation (5) by considering the appropriate negative outlet quality in subcooled flow boiling, and it is delicately adjusted by visual investigation.

When it comes to pressure, its effects on enlarging the interval of inlet subcooling is rather ambiguous. Following the definition of inlet subcooling in the equation (6), increasing pressure leads to not only the increment of saturation temperature, but also that of tube inlet temperature due to the increased temperature in the main tank and the conditioner inlet. The unpredictable influence of pressure was examined in the preliminary experiment, and pressure was fixed at *7.7 bar* in this study.

$$\Delta T_{sub} = T_{sat}(P) - T_{f,i} \quad (6)$$

Despite of this endeavor, the maximum difference in inlet subcooling in the matrix was bounded at $2\text{ }^{\circ}\text{C}$. Therefore investigation of the influence of inlet subcooling was underemphasized in this study.

2.3.2 Mass flow rate and inlet subcooling matrix

In order to examine the influences of mass flow rate and inlet subcooling, two sets of experiments were conducted. Mass flow rate was varied around 300 and 500 $\text{kg} / \text{m}^2\text{s}$ and inlet subcooling was shifted from 34.0 to 36.0 $^{\circ}\text{C}$. Pressure was fixed at *7.7 bar* in both experiment sets. As a dependent variable, different heat fluxes were fixed in each

experiment set, and the values were determined depending on other three parameters. Each experiment set has around 40 cases with approximately eight mass flow rates and five inlet subcoolings. Both matrixes are not in rectangular shapes because bubbles are generated vigorously in low mass flow rate and low inlet subcooling, and vice versa.

The detail experimental conditions of set 1 and 2 are provided in Table 4. Deviation in the table is the average of differences between the measured values and the desired ones. In Figure 9, the measured operating conditions are expressed as colored points and the desired ones are the intersections of the dotted lines.

Table 4 Experimental conditions of mass flow rate and inlet subcooling matrix, set 1 and 2

| Set | Type | Parameter | Value | Interval | Deviation |
|-----|------------|------------------------------|-------------|----------|-----------|
| 1 | Adjusted | $P [bar]$ | 7.7 | - | 0.00 |
| | | $q [kW / m^2]$ | 7.64 | - | 0.01 |
| | Controlled | $G [kg / m^2s]$ | 270 - 340 | 6.0 | 0.78 |
| | | $\Delta T_{sub} [^{\circ}C]$ | 34.0 – 36.0 | 0.5 | 0.03 |
| 2 | Adjusted | $P [bar]$ | 7.7 | - | 0.00 |
| | | $q [kW / m^2]$ | 13.21 | - | 0.00 |
| | Controlled | $G [kg / m^2s]$ | 460 - 560 | 10.0 | 1.14 |
| | | $\Delta T_{sub} [^{\circ}C]$ | 34.0 - 36.0 | 0.5 | 0.03 |

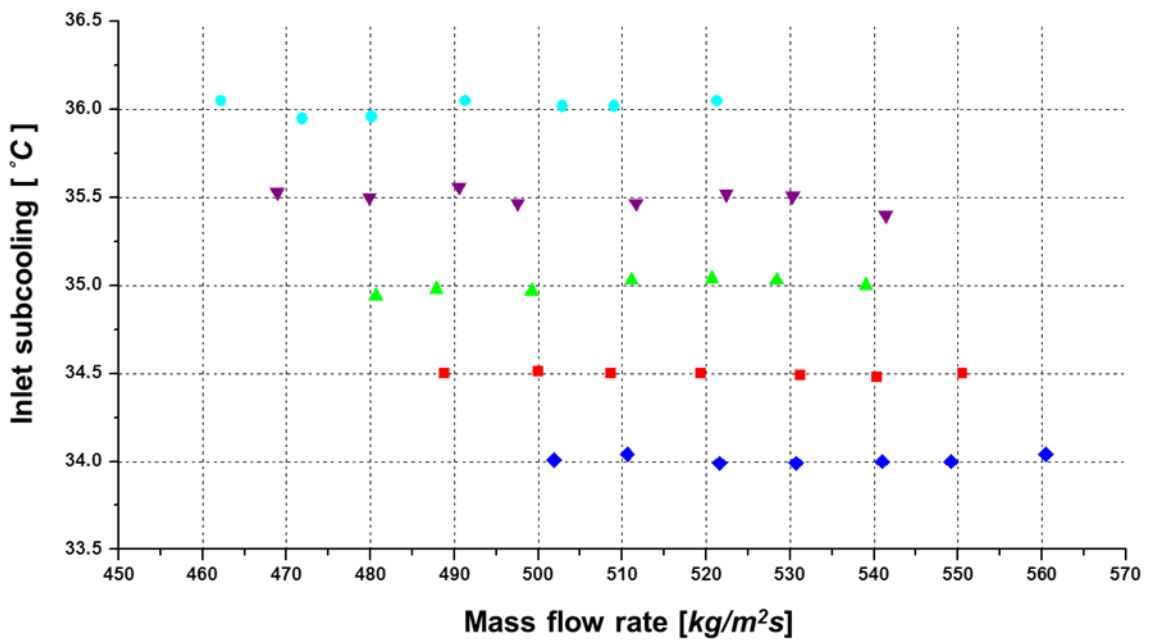
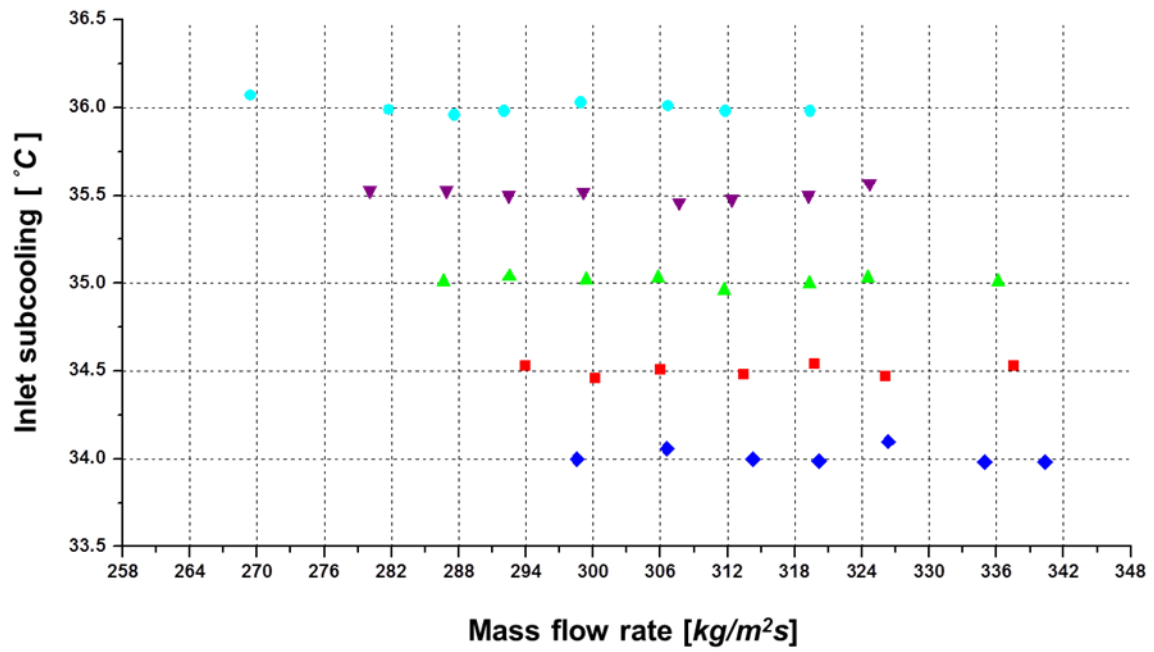


Figure 9 Recorded experimental conditions of set 1 (top) and set 2 (bottom)

2.3.3 Heat flux

To investigate the effect of the imposed heat flux on bubble characteristics and heat transfer rate, two sets of experiments of controlling heat flux were conducted for two mass flow rates, 300 and 500 kg/m^2s , with the same pressure and inlet subcooling.. Table 5 presents the experimental conditions of set 3 and 4.

Table 5 Experimental conditions with varying heat flux, set 3 and 4

| Set | Type | Parameter | Value | Interval | Deviation |
|-----|------------|------------------------------|------------------|----------|-----------|
| 3 | Adjusted | $P [bar]$ | 7.7 | - | 0.00 |
| | | $G [kg / m^2s]$ | 300 | - | 1.43 |
| | | $\Delta T_{sub} [^{\circ}C]$ | 34.0 | - | 0.03 |
| | Controlled | $q [kW / m^2]$ | 7.06 - 8.02 | 0.19 | 0.00 |
| 4 | Adjusted | $P [bar]$ | 7.7 | - | 0.01 |
| | | $G [kg / m^2s]$ | 500 | - | 0.78 |
| | | $\Delta T_{sub} [^{\circ}C]$ | 34.0 | - | 0.02 |
| | Controlled | $q [kW / m^2]$ | 11.42 - 13.21 | 0.25 | 0.00 |

2.3.4 Power

Two experiment sets with 300 and 500 kg/m^2s of mass flow rates and corresponding distinct heat flux and the same inlet subcooling were carried out for identifying the influence of pressure on the bubble characteristics and heat transfer. The adjusted inlet subcooling and heat flux were reduced in this experiment group, comparing with those in other experimental groups, in order to retain the wider span of pressure changes. Table 6 presents the experimental conditions of set 5 and 6

Table 6 Experimental conditions of varying pressure, set 5 and 6

| Set | Type | Parameter | Value | Interval | Deviation |
|-----|------------|------------------------------|-----------|----------|-----------|
| 5 | Adjusted | $G [kg / m^2s]$ | 300 | - | 1.01 |
| | | $\Delta T_{sub} [^{\circ}C]$ | 25.0 | - | 0.03 |
| | | $q [kW / m^2]$ | 5.31 | - | 0.00 |
| | Controlled | $P [bar]$ | 6.7 - 7.7 | 0.5 | 0.01 |
| 6 | Adjusted | $G [kg / m^2s]$ | 500 | - | 1.33 |
| | | $\Delta T_{sub} [^{\circ}C]$ | 25.0 | - | 0.03 |
| | | $q [kW / m^2]$ | 9.95 | - | 0.00 |
| | Controlled | $P [bar]$ | 4.7 - 7.7 | 0.5 | 0.01 |

2.3.5 Coupling effect of inlet subcooling and heat flux

The experiments of varying single parameter while maintaining others for observing the change of bubble characteristics and heat transfer coefficient have been widely performed in the past. The variation of singular parameter leads to the secondary movements of uncontrollable parameters, for instance, low mass flow rate generally results in high wall superheating. These secondary movements come down to the different outlet thermodynamical equilibrium state, quantified as the outlet quality. In other words, the comparison analyses in the previous studies were performed for fluids with different thermodynamical equilibrium state. Therefore, their experiments may be concluded that the variations of bubble characteristics could result from the different thermodynamical equilibrium state of the tube exit fluid, not from the variations of parameters.

In this experimental set, outlet quality was selected as the additional fixed parameter, and inlet subcooling and heat flux were varied at the same time. In this manner, different bubble characteristics were observed in outlet fluid with the same outlet quality, and this fact could clarify the coupling effects of inlet subcooling and heat flux. Note that the same thermodynamical equilibrium state means the same liquid temperature at tube exit, since the outlet quality is calculated based on the measured exit condition as defined in the equation (5).

Two sets of experiments were conducted by decreasing inlet subcooling and heat flux simultaneously. Table 7 and 8 show the experimental conditions of two sets.

Table 7 Experimental conditions of coupling effects in set 7

| $P = 7.7 \text{ bar} , G = 300 \text{ kg} / \text{m}^2 \text{ s}$ | | | | |
|---|-----------------------------------|-------|-------|------|
| Parameter | Set 7 ($x_{outlet} = - 0.0392$) | | | |
| | 7-1 | 7-2 | 7-3 | 7-4 |
| $\Delta T_{sub} [^{\circ}C]$ | 35.02 | 39.96 | 35.05 | 20.0 |
| $q [kW / m^2]$ | 7.64 | 6.46 | 5.28 | 4.07 |

Table 8 Experimental conditions of coupling effects in set 8

| $P = 7.7 \text{ bar} , G = 500 \text{ kg} / \text{m}^2 \text{ s}$ | | | | |
|---|-----------------------------------|-------|-------|-------|
| Parameter | Set 8 ($x_{outlet} = - 0.0362$) | | | |
| | 8-1 | 8-2 | 8-3 | 8-4 |
| $\Delta T_{sub} [^{\circ}C]$ | 34.96 | 29.99 | 25.03 | 20.01 |
| $q [kW / m^2]$ | 13.21 | 11.11 | 8.98 | 6.84 |

3 Data processing

Investigating the bubble characteristics requires multistep of image processing and designation of the obtained data in accordance with the objective of study. Through the image processing composed of several steps, distortion or missing of the important data could be occurred. Therefore, the appropriate algorithms of image processing and data for representing the videos should be determined in order to analyze the experimental results accurately.

3.1 Image analysis

3.1.1 Image analysis algorithm

The commercial software (Oxford Lasers - VisiSize) was used for extracting the quantitative data from the bubble images, such as bubble diameters and velocities. The software recognizes the bubbles by distinguishing between the bubble shadows and the illuminated background [40]. That means it is important that the difference in the brightness between bubbles and background should be distinct for correct reading. In this sense, the original images captured by the high-speed camera are not suitable due to the gray

background and consistently captured dust and scratch on the glass. For providing the better image for analysis in the software, the procedure of removing background and contaminations was performed. By comparing the original image with the saved background image without bubbles, gray background could be white and the dust and scratch expressed as black points in the original images could be eliminated. This procedure was carried out by a Matlab program. An example of image processing is presented in Figure 10.

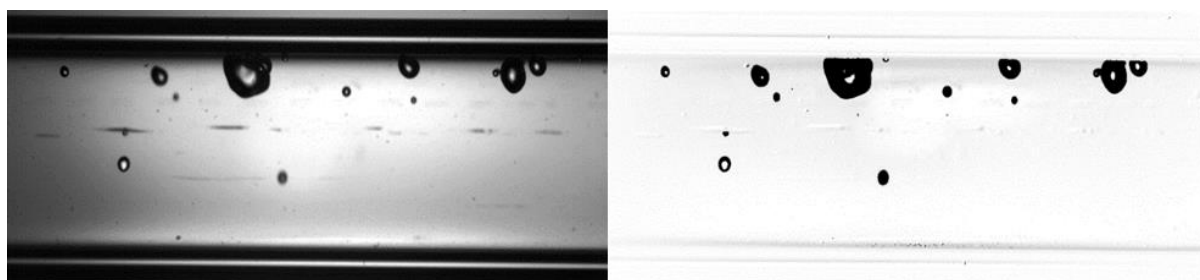


Figure 10 Example of image processing, before (left) and after (right)

The fabricated images were inserted in the software. The software provides a large number of qualitative bubble characteristics and below six information of them were used in the present study:

- Bubble diameters
- Bubble velocities
- The size distribution

- Categorized bubble velocities with different size groups
- Total number of counted bubbles
- Sphericity of bubbles

Based on the six fundamental data from the software, other bubble characteristics were calculated.

3.1.2 Measurements of bubble diameter and velocity

There are several definitions of bubble diameter for non-spherical bubble. A specific definition should be selected among the proposed ones for the elongated sliding bubbles. In the present study, equivalent circular area was chosen, which is expressed as the equation (7).

$$d_a = K_p \sqrt{\frac{4A_b}{\pi}}, \quad d_i = d_a \quad (7)$$

where A_b is the measured area occupied by bubble image in pixel and K_p is the distance between adjacent pixels and it is around $16.18 \mu\text{m}/\text{pixel}$ in this analysis.

Equivalent circular perimeter is the different way of characterizing bubble diameter based on the perimeter of bubble image in pixel and it is defined as the equation (8).

$$d_{pe} = K_p \left(\frac{P}{\pi} \right) \quad (8)$$

Sphericity of bubble is presented using the ratio between two bubble diameters as $(d_a / d_{pe})^2$.

The value is always between 0 and 1.

A set of consecutive images can be a source for obtaining bubble velocity. The software calculates the velocity using a technique called particle tracking. By identifying the same bubble in the different images, the traveling distance can be gained and it is used for calculating bubble velocity as:

$$v_b = K_p \frac{\sqrt{(x_2 - x_1)^2 + (y_2 - y_1)^2}}{\Delta t}, \quad (9)$$

where x_1, x_2 are the axial locations of bubble center and y_1, y_2 are the vertical locations of it and different figure in subscript means different images. Δt expresses the time interval between the images, and it is 2 ms from 500 frames/s of the shutter speed in the present analysis.

3.1.3 Correction for the number of bubbles

As an Eulerian specification of the flow field, the software counts the number of bubbles in a cumulative way. In other words, the same bubble in the consecutive images is counted redundantly. This point provides the wrong standard of counting for bubbles with different size due to the following feature.

The software can read a bubble only if the entire body appears in the window: If a bubble is cut by the edge of window, its image is dismissed. This is because the software identifies the bubble by tracking the black outer surface of it. As passing through the visualization section, all of bubbles experience truncation by the window edge at their appearing and disappearing moment in the window. Figure 11 is an example that bubble is counted while flowing, but is dismissed at the disappearing instant. Red 'B' on the bubble image means 'border', indicating that the bubble is uncounted because of its distorted shape. If long bubble appears and disappears through several images, they are counted less than reality. As a result, the fraction of uncounted bubble is different depending on its size, and specifically, it leads to underestimated number of large bubbles. Therefore an appropriate correction should be conducted for rectifying this error.

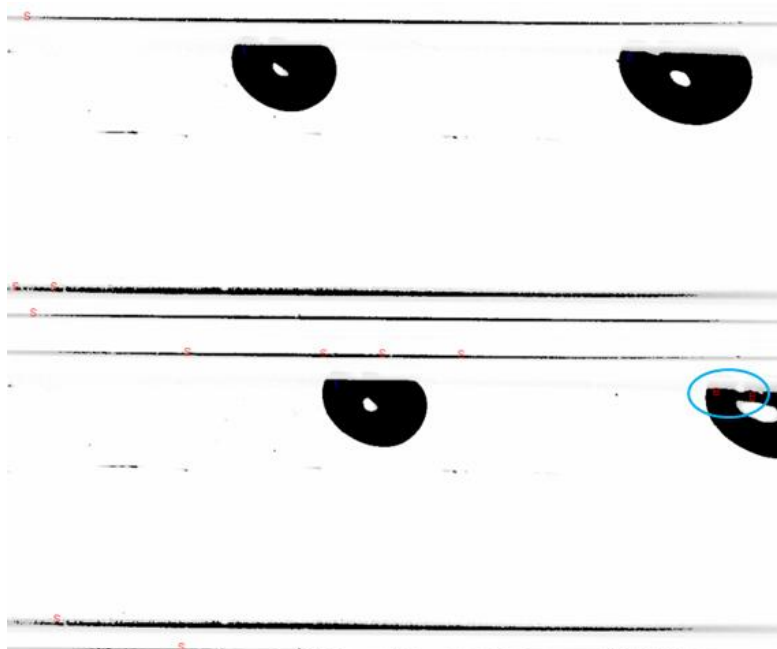


Figure 11 Dismissed bubble due to its cut shape

Proper correction factors were multiplied to the obtained number of bubbles from the software and the factors are different according to the bubble sizes. For determining the factors, bubbles were classified by their sizes and both the numbers of uncounted and counted bubbles in the each classification were manually analyzed. This analysis was conducted for the 14 set of videos with various mass flow rates. The correction factor CF is defined in the equation (10).

$$CF = \frac{N_c + N_u}{N_c} \quad (10)$$

where N_c is the number of images where a bubble is counted, while N_u is the thing where a bubble is not counted. Note that since the factors are expressed as the fraction comes from the values of flowing bubbles, the values are irrespective of absolute flowing velocity. In fact, it was turn out that a set of correlation factors is independent of the bulk mass flow rate. Consequently, the same set of factors was applied for every video. The correction factors used in this study are presented in Table 9.

Table 9 Correction factors for number of bubbles

| Diameter region [mm] | Correction factor |
|----------------------|-------------------|
| 0 – 1.00 | 1.00 |
| 1.00 – 1.75 | 1.10 |
| 1.75 – 2.25 | 1.20 |
| 2.25 – 2.75 | 1.30 |
| 2.75 – 3.25 | 1.45 |
| 3.25 – 3.75 | 1.63 |
| 3.75 – 4.50 | 1.90 |
| 4.50 – 5.00 | 3.00 |
| Over 5.00 | 5.00 |

3.2 Data reduction

3.2.1 Basic assumption

To simplify the data reduction, the following assumptions were applied in this study.

- No pressure loss along the heated section
- Perfect insulation of the tube and visualization section.
- No axial heat transfer except for convective heat transfer due to bulk mass flow

In experiments, the insignificant pressure drop in the heated section was confirmed. The value was around 0.1 *bar* of the 7.7 *bar* of inlet pressure, and this is too small to affect the variation in the fluid properties.

3.2.2 Inner wall temperature

Since the thermocouples are placed at the outer wall surface, the inner wall temperature was derived from the value. Under the assumption of perfect insulation and no axial heat transfer, the steady state heat transfer equation is derived as the equation (11).

$$\frac{1}{r} \frac{d}{dr} \left(r \frac{dT}{dr} \right) + \frac{q}{k_w} = 0 \quad (11)$$

By integrating the equation with the measured outer wall temperature as the boundary condition, the expression for the inner wall temperature is:

$$T_{wi} = T_{wo} + \frac{q''}{16k_w}(D_o^2 - D_i^2) - \frac{q''}{8k_w}D_o^2 \ln\left(\frac{D_o}{D_i}\right), \quad (12)$$

The volumetric heat transfer q'' is given by the equation (13).

$$q'' = \frac{4qD_i}{(D_o^2 - D_i^2)}, \quad (13)$$

Substituting the equation (13) into the equation (12) leads to the equation (14).

$$T_{wi} = T_{wo} + \frac{qD_i}{k_w} - \frac{2qD_i^3}{k_w(D_o^2 - D_i^2)} \ln\left(\frac{D_o}{D_i}\right) \quad (14)$$

The thermal conductivity of the wall k_w has the value of $0.0165 \text{ kW} / \text{mK}$ for stainless steel wall.

3.2.3 Wall temperature and liquid temperature profiles

Wall temperature and liquid temperature profile were linearly interpolated by using the nine measured wall temperature and two measured bulk liquid temperature along the tube.

Figure 12 illustrates the typical aspects of the two interpolated temperature profiles and the validity of linear interpolation was verified in two points of view.

The first is the constant single phase heat transfer coefficient. Before reaching the onset of nucleation boiling (ONB) point, the fluid is pure liquid state and the heat transfer coefficient

is almost constant along the tube. The linearly interpolated wall temperature and bulk liquid temperature are parallel in Figure 12 and this indicates the constant heat transfer coefficient in the region.

The secondary support is wall temperature drop at the last point in Figure 12. A.B. Ozar [13] detected the wall temperature drop after its maximum by analyzing the color change of liquid crystal on the heated tube. Although the author hasn't stated the physical meaning of the maximum point, it is estimated as the point of ONB. In the present study the calculated the point of ONB normally lies before and after the maximum point, hence the linear interpolation of wall temperature seems to be reasonable. However, since real maximum wall temperature may not be exactly located at the penultimate thermocouple, judging the measured maximum is ONB point should be prudent.

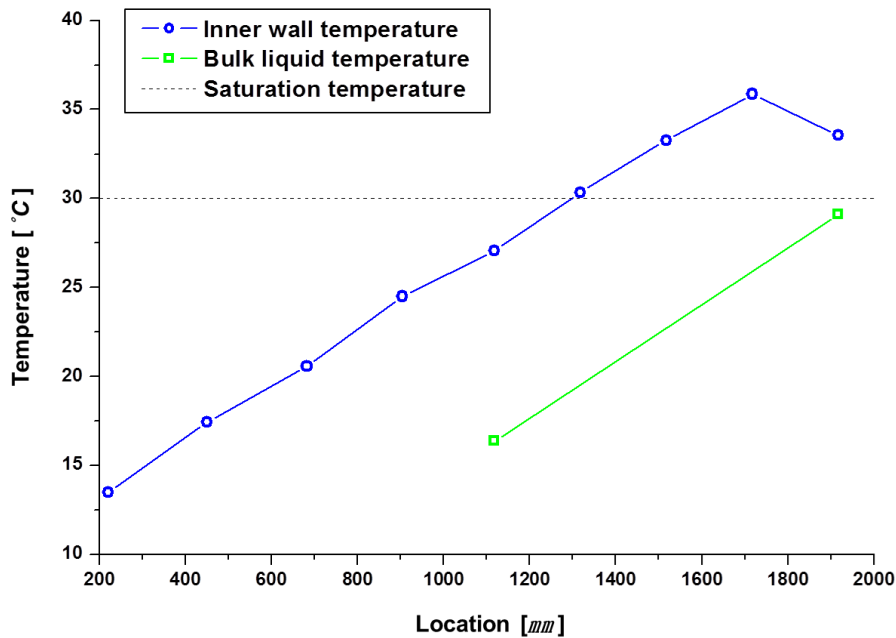


Figure 12 Temperature profiles of inner wall and bulk liquid

3.2.4 Pearson's system

In order to express the obtained size distribution from experiments as a formulated form, Pearson's system was used. According to K. Pearson [30], the distribution is generally involved in the three main Pearson types of I, IV, and VI. The following four moments derived from the given distribution are the parameters of determining the Pearson type.

Four moments (K.O. Bowman [31])

$$1) \text{ Mean, } \mu_1 \quad \mu_1 = E[x] \quad (15)$$

$$2) \text{ Variance, } \mu_2 \quad \mu_2 = E[(x - \mu_1)^2] = E[x^2] - \mu_1^2 \quad (16)$$

$$\mu_3 = E[(x - \mu_1)^3] = E[x^3] - 3\mu_1\mu_2 - \mu_1^3 \quad (17)$$

$$\mu_4 = E[(x - \mu_1)^4] = E[x^4] - 4\mu_1\mu_3 - 6\mu_1^2\mu_2 - \mu_1^4 \quad (18)$$

$$3) \text{ Skewness, } \beta_1 \quad \beta_1 = \frac{\mu_3^2}{\mu_2^3} \quad (19)$$

$$4) \text{ Kurtosis, } \beta_2 \quad \beta_2 = \frac{\mu_4}{\mu_2^2} \quad (20)$$

The following parameters are defined in Pearson's system as

$$p, q = \frac{r}{2} \left\{ 1 \mp (r+2) \frac{\sqrt{\beta_1}}{\sqrt{D}} \right\} \quad (21)$$

$$b - a = \sqrt{\mu_2} \sqrt{D}$$

$$a = \mu_1 - (b - a)p / (p + q)$$

$$r = \frac{6(\beta_2 - \beta_1 - 1)}{6 + 3\beta_1 - 2\beta_2}, \quad D = (r + 2)^2 \beta_1 + 16(r + 1)$$

$$\kappa = \frac{\beta_1(\beta_2 + 3)^2}{4(4\beta_2 - 3\beta_1)(2\beta_2 - 3\beta_1 - 6)},$$

The parameter κ is the criterion of classifying the given distribution into the three main types. If κ is negative, the distribution is type I, or κ is between 0 and 1, it is involved in type IV, otherwise, it is type VI distribution.

In the present study, most of the size distributions show bi-modal shape composed of separated two groups with different bubble diameters. The small bubble group has L-shape distribution, while the large bubble group has bell-shape distribution. Two groups were individually expressed in Pearson's distribution, and it was turn out that every distribution, either the small or large bubble group, is involved in type I distribution: κ has negative value in the every case. Type I distribution can describe both L-shape(widely-called inverted J-shaped) and bell-shape depending on the combination of parameters.

The probability density function of type I distribution can be expressed as the equation (22).

$$B(x; a, b, p, q) = \frac{\Gamma(p+q)}{\Gamma(p)\Gamma(q)} \frac{(x-a)^{p-1}(b-x)^{q-1}}{(b-a)^{p+q-1}} \quad (a \leq x \leq b; \quad p, q > 0) \quad (22)$$

And the function is normalized as the equation (23) and it is compared with the measured size distribution.

$$B_n(x) = \frac{B(x)}{\int_0^\infty B(x)dx} \quad (23)$$

Therefore, in the present study, both size distributions of small and large bubble group were expressed as type I distribution. Feasibility of predicting the size distribution by means of Pearson's system was evaluated in terms of the area difference enclosed by two distribution functions. Mean deviation E is defined as the equation (24), which indicates quadrable discrepancy of Pearson's system.

$$E = \int_0^{\infty} \sqrt{(f_s(d) - B_n(d))^2} dd \quad (24)$$

3.2.5 Data bank structure

To compare the acquired images under different conditions, qualitative data are required which represent the bubble characteristics. The data were stored in a data bank structure in this study. The data bank structure composes of the information which comes from the operating conditions and from the results of image processing and some of them are obtained from the chosen prediction models for flow boiling characteristics.

From the operating conditions

- Inlet pressure, P [bar]
- Inlet subcooling, ΔT_{sub} [$^{\circ}C$]
- Mass flow rate, G [$kg / m^2 s$]

$$G = \frac{\rho_{f,i} \dot{V}_i}{60,000 A_i} \quad (25)$$

- Heat flux, q [kW / m^2]
- Outlet vapor quality calculated by heat balance, x_{outlet}
- Outlet bulk liquid velocity, $v_{f,o}$ [m / s]

$$v_{f,o} = \frac{G}{\rho_{f,o}} \quad (26)$$

- Wall temperature and bulk liquid temperature profile along the tube
- Wall superheat, ΔT_{sat} [$^{\circ}C$]

$$\Delta T_{sat} = T_{w,i,9} - T_{sat}(P_{out}) \quad (27)$$

$\Delta T_{w,i,9}$ is the converted inlet wall temperature from the ninth measured outlet wall temperature.

- Local heat transfer coefficient, h [$W / m^2 s$]

$$h = \frac{q}{T_{w,i,9} - T_{f,2}} \quad (28)$$

$T_{f,2}$ is the measured bulk liquid temperature in the second bulk liquid thermocouple, which is located at the same axial position with the ninth thermocouple for measure outlet wall temperature.

From the image processing

- Bubble population, N_{pop} [mm^{-3}]

Bubble population is defined as the number of bubbles per unit volume in this study.

$$N_{pop} = \frac{N_b}{S_v} \quad (29)$$

N_b is defined as the total number of redundantly counted bubbles with the correction in an image data set and S_v is the summation of windows volume in an image data set. As the volume in the denominator of right hand side in the equation (29), S_v was used rather than the estimated total volume by tracking bulk flow in an image set. The repeated number of bubbles is offset by this unusual definition of total volume, because the volume is repeatedly added as well. Based on the window size and six videos for one image data set, S_v is calculated as the equation (30).

$$S_v = \frac{\pi}{4} D_i^2 L_v \times 2500 \times 6 = \frac{\pi}{4} \times 5^2 \times 16.18 \times 2500 \times 6 = 4.7654E + 06 \text{ mm}^3 \quad (30)$$

Note that the bubble population differs to the idiom “nucleation site density”, which has been widely mentioned in the previous studies as monitoring the bubble incipient place.

- Average bubble diameter, μ_1 [mm]

$$\mu_1 = \frac{\sum_{i=1}^{\infty} d_i}{N_b} \quad (31)$$

- Modal bubble diameter of the large bubble group d_m [mm]

“Mode of the large bubble group” is used as short for it in the present paper. Among the bi-modal distribution, the modal diameter of the large bubble group is selected as shown in Figure 13.

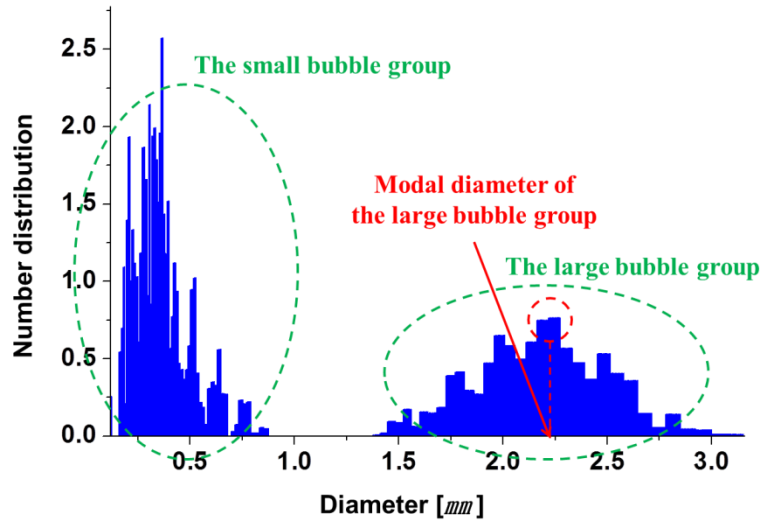


Figure 13 Modal diameter of the large bubble group

- Interfacial area concentration, a_i [mm^{-1}]

$$a_i = \frac{\sum \frac{\pi}{4} d_i^2}{S_V} \quad (32)$$

- Void fraction, α

$$\alpha = \frac{\sum \frac{\pi}{6} d_i^3}{S_V} \quad (33)$$

- Variance of the large bubble group, $\mu_{2,l}$ [mm^2]

Variance gives the degree of spread of the large bubble group, and this is useful parameter since this group generally has a bell-shape. Variance of the large bubble group can be defined as follows:

$$\mu_2 = \frac{1}{N_b} \sum_{i=l_1}^{l_\infty} (d_i - \mu_1)^2 \quad (34)$$

where l_1 and l_∞ are the smallest and the largest bubble in the large bubble group, respectively, and $\mu_{1,l}$ is the average bubble diameter of the large bubble group.

- Kurtosis of the small bubble group

Kurtosis provides the peakedness of the distribution. Peakedness is of importance for the small bubble group because it shows the L-shape distribution. Kurtosis could be either positive or negative, in either way; high kurtosis indicates a slender distribution with acute peak and fatter tail, while low one indicates a broad distribution with wider peak and thinner tail.

$$Ku = \frac{1}{\mu_2} \frac{\sum_{i=1}^{s_\infty} (d_i - \mu_1)^2}{N_b} - 3 \quad (35)$$

where s_∞ is the largest bubble in the small bubble group and $\mu_{1,s}$ and $\mu_{2,s}$ are the average and variance of bubble diameter of the small bubble group, respectively.

- The size distribution, $f_s(d_i)$

$$f_s(d_i) = \frac{N(d_i)}{\sum_{i=1}^{\infty} [N(d_i)(d_{i+1} - d_i)]} \quad (36)$$

where $N(d_i)$ is the number of bubbles with diameter d_i .

- Mean deviation, E

E is defined as the equation (24).

- The volume distribution, $f_v(d_i)$

$$f_v(d_i) = \frac{\frac{\pi}{6} d_i^3 N(d_i)}{\sum_{i=1}^{\infty} [\frac{\pi}{6} d_i^3 N(d_i) (d_{i+1} - d_i)]} \quad (37)$$

Note that all of distributions in the present study are normalized.

- Size-velocity diagram

The average velocities categorized by bubble sizes were obtained from the image processing. Size-velocity diagram shows the specific velocities of different size of bubbles.

- Average sliding bubble velocity, \bar{v}_b

To average only the bubble sliding velocities, bubbles under 0.3 mm of diameter were excluded, which are floating in the core liquid rather than sliding along the upper surface.

$$\bar{v}_b = \frac{\sum_{i=n_{300}}^{\infty} v_{b,i}}{N_{b,300}} \quad (38)$$

where n_{300} indicates the smallest bubble among the bubble group over 0.3 mm of diameter and $N_{b,300}$ is the total number of total redundantly counted bubbles with more than 0.3 mm of diameter.

- Slip ratio, $C_{r,i}$

Slip ratio is defined as the relative velocity between measured single sliding bubble and outlet bulk liquid velocity

$$C_{r,i} = v_{b,i} / v_{f,o} \quad (39)$$

From the selected models in the present study

- The point of ONB

The location and wall superheat temperature at ONB is important criterion in subcooled flow boiling. Several models have been proposed from experimental or analytical analyses. Bergles and Rohsenow(1964), Davis and Anderson(1966), Marsh and Mudawar(1989), Basu et al.(2002) are widely used. In the present study, Manon(1999) is used, which is modified model of Davis and Anderson for applying to other fluids than water.

$$\Delta T_{sat,ONB} = (T_w - T_{sat})_{ONB} = \left(\frac{8\sigma q T_{sat}}{i_{fg} q \rho_g} \right)^{1/2} Pr_f \quad (40)$$

In this study, the ONB location, corresponding to the wall superheat at ONB from the equation (40), is obtained from the measured wall temperature profile.

- The point of the onset of significant void (OSV)

Even though several models for predicting OSV point have been proposed, including Levy(1967), Staub(1968), Rogers et al.(1987), these models can be applied only for

hydrodynamically controlled regime where is $Pe_f > 70,000$ according to Saha and Zuber(1974)'s criterion. However, most of operating conditions in the present experiments are within 50,000 of, i.e., thermally controlled regime, hence Saha and Zuber(1974) model, which has been used in this regime, is used in the present study. H. Dorra et al. [32] have shown that the model is the best for predicting OSV in vertical subcooled flow boiling, however, this gave quite reasonable solution for these experiments about horizontal channel. According to the model, OSV occurs when the following criterion is met:

$$Nu_{OSV} = \frac{qD_i}{k_f(T_{sat} - T_{f,OSV})} = 455 \quad (41)$$

In the same way with the procedure of determining ONB position, the location was estimated by using the measured wall and bulk liquid temperature profiles, where the equation (41) gave a solution.

In addition, equations (40) and (41) were solved by iteration as estimating ONB and OSV points respectively and calculating needed fluid properties from the linearly interpolated bulk liquid temperature at these points.

- Local liquid velocity

Local liquid velocity at the mass center of sliding bubble is important for obtaining the accurate relative velocities which could be used in analyzing the drag force and the shear lift force applied to the bubble. The local liquid velocity near the wall is estimated by using universal turbulent flow profile of single phase from the model proposed by R. Situ

et al. [33]. Three expressions for velocities were suggested for different distance from the wall by the following formula:

$$u^+ = \begin{cases} x^+ & x^+ \leq 5 \\ 5 \ln x^+ - 3.05 & 5 < x^+ < 30 \\ 2.5 \ln x^+ + 5.5 & x^+ \geq 30 \end{cases}, \quad (42)$$

The dimensionless velocity v^+ and the dimensionless distance from the wall x^+ are defined as the equation (43) and (44), respectively.

$$u^+ = \frac{u_f}{\sqrt{\tau_w / \rho_f}} \quad (43)$$

$$x^+ = \frac{y \sqrt{\tau_w / \rho_f}}{\nu_f} \quad (44)$$

The wall shear stress τ_w can be calculated by the equation (45).

$$\tau_w = \frac{\lambda}{8} \rho_f v_f^2 \quad (45)$$

where v_f is the area-average liquid velocity and λ is the frictional factor. For a smooth surface of stainless steel and annular tube, the friction factor is expressed by the equation (46).

$$\left\{ \begin{array}{ll} \lambda = \frac{64}{\text{Re}} & \text{Re}_f < 2320 \\ \lambda = \frac{0.3164}{\text{Re}^{0.25}} & 4 \times 10^3 < \text{Re}_f < 10^5 \\ \lambda = 0.0032 + 0.221 \text{Re}^{-0.237} & 10^5 < \text{Re}_f < 3 \times 10^6 \end{array} \right. \quad (46)$$

For x^+ between 5 and 30, R. Maurus et al. [11] have shown the estimated velocity profile from this model is close to their measurements.

4 Results and discussion

4.1 Phenomenological analysis of bubble characteristics

While flowing along the tube after departing from their nucleation sites, bubbles go through evaporation, condensation, coalescence with neighbor bubbles, and even breakage at high flow rate. Since bubble observation in this study was performed at the visualization glass which is not the heated section any longer as well as is apart from the point of ONB, the captured bubbles are the outcomes of those complex mechanisms and their characteristics could be different from those at the moment of departure or lift-off. Thus, the parametric analysis in the present study should cover all of the mechanisms that might have affected to the observed bubble characteristics.

Figure 14 is the size distribution obtained at $P = 7.7 \text{ bar}$, $\Delta T_{sub} = 35.0 \text{ }^\circ\text{C}$, $G = 300 \text{ kg / m}^2\text{s}$, and $q = 7.64 \text{ kW / m}^2\text{s}$, and it shows the representative shape of size distribution which is found in most of operating conditions. The size distribution clearly indicates the existence of two separated bubble size groups, named small bubble group and large bubble group representatively in this study. Additional noticeable point is the existence of valley between two groups, which indicates that bubble with certain size was hardly detected.

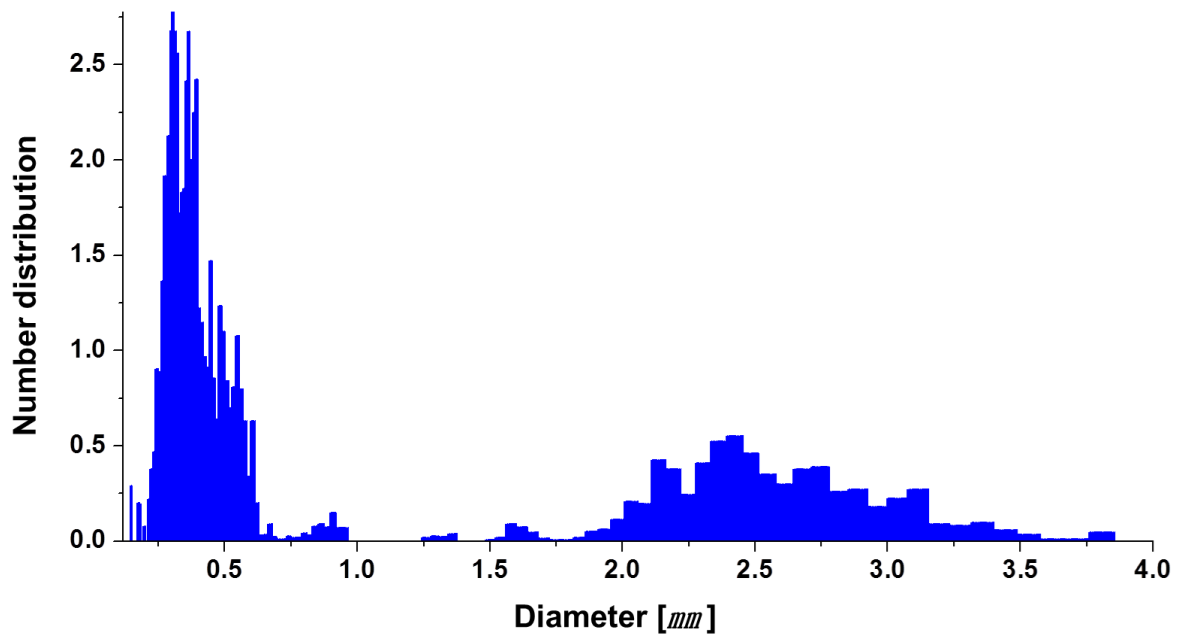


Figure 14 Representative size distribution obtained at $P = 7.7 \text{ bar}$, $G = 300 \text{ kg/m}^2\text{s}$, $\Delta T_{sub} = 35.0^\circ \text{C}$, and $q = 7.64 \text{ kW/m}^2$

Figure 15 is the typical flow patterns in our experimental conditions. Around $G = 300$ and $500 \text{ kg/m}^2\text{s}$ of mass flow rate, corresponding to 0.23 and 0.40 m/s of bulk liquid velocity, most of bubbles are sliding with being attached to the upper part of the heated surface and only tiny bubbles, less than 0.3 mm in diameter, lift-off and flow in the core of liquid. This is mainly due to the buoyancy force, which becomes a significant force component for large bubbles, and the force hinders the bubbles generated at the upper part from lifting-off and plays a role of collecting bubbles generated at other surfaces to upper wall. In addition, the bulk liquid velocity near wall is not high enough to satisfy the bubble lift-off condition that the shear-lift force should exceed the sum of the unsteady drag force and buoyancy force.

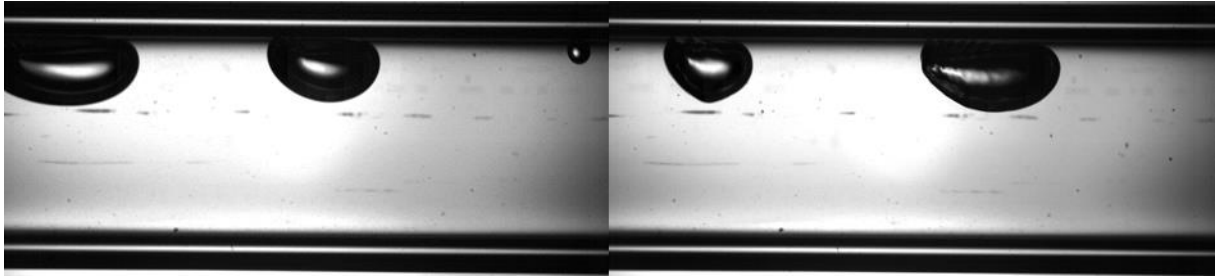


Figure 15 Typical bubble flowing patterns at $G = 300 \text{ kg/m}^2\text{s}$ (left) and $500 \text{ kg/m}^2\text{s}$ (right)

Figure 16 shows the typical aspect of bubble sliding velocities by sizes, which was measured at $G = 500 \text{ kg/m}^2\text{s}$, and it illustrates two important points: first, larger sliding bubbles are faster and their velocities are converged to bulk liquid velocity, and second, velocities are declined as increasing bubble sizes in lift-off region, which is out of analysis scope of the present study. As seen in Figure 15, larger sliding bubble has slender shape which helps it flowing with liquid smoothly. Thus, this streamlined shape of large bubble makes it sliding faster.

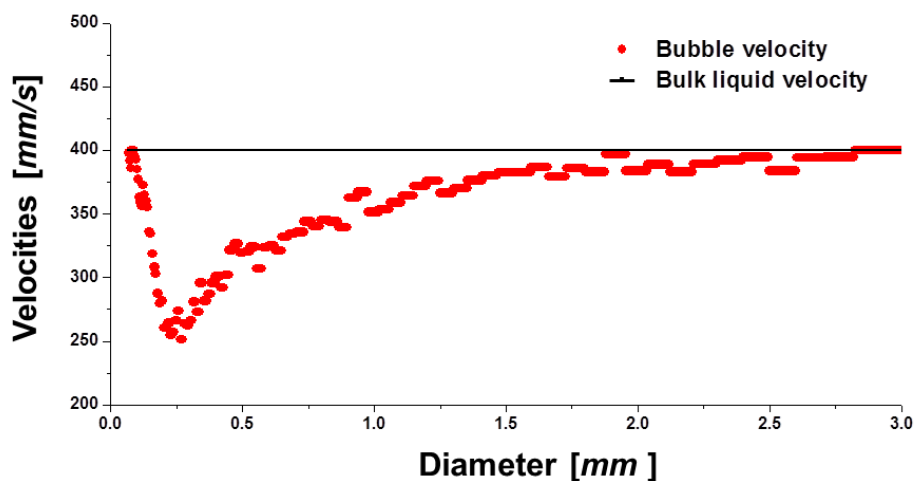


Figure 16 Typical size-velocity diagram measured at $G = 500 \text{ kg/m}^2\text{s}$

As approaching to the favorable bubble generation conditions, such as higher heat flux or lower mass flow rate, bubble coalescences may more actively occur both at the nucleation sites and in the flow. Ultra-size bubbles, around 5 mm of diameter in equivalent circular area and 10 mm of corresponding length, were occasionally observed and it is impossible to explain their existence without coalescence during flowing. Since sliding bubbles are flowing on the same line, along the upper surface, bubble coalescence between them could be occurred only when the rear bubble catch up with the front bubble. This means that for coalescence in flowing, the velocity of the rear bubble must be higher than that of the forward bubble. Due to higher sliding velocity of larger bubble, it could be concluded that the coalescence in flowing could be happened only when larger bubble follows smaller bubble. The hypothesis about genesis principle of ultra-size bubbles was demonstrated by analyzing the captured bubble images like as Figure 17. The stated way of coalescing is shown in Figure 17. Besides, the moment that rear smaller bubble rams into the front larger bubble was never found in the experiments.

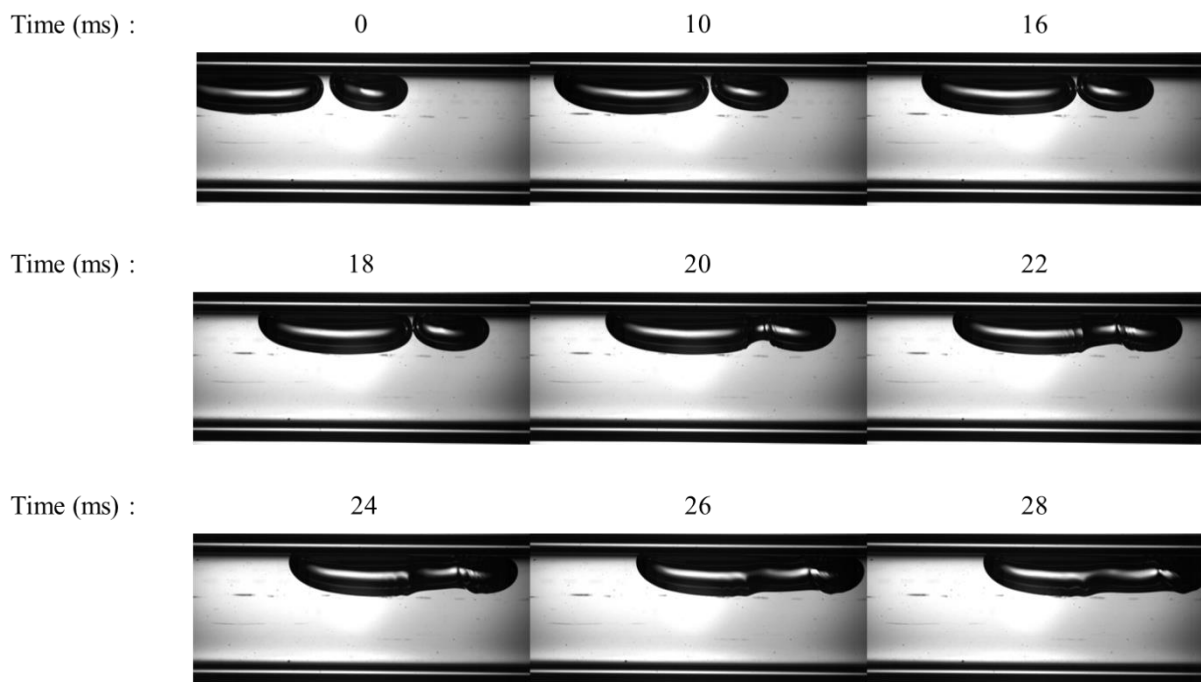


Figure 17 Observed bubble coalescence in flowing, diameter of front bubble: 2.34, rear bubble: 3.87, and after coalescence: 4.64 mm

Moreover, it was observed that other bubbles are existed in the front of the ultra-size bubble, but no bubble is found for a few milliseconds after its detection. This observation can be a evidence for supporting the assertion that coalescence in flowing is main mechanisms for forming large sliding bubbles rather than interactions between nucleation sites or single bubble growth. This interesting phenomenon could be happened because the ultra-size bubble has been formed by merging preceding small bubbles and the other small bubbles in the wake of it cannot narrow the distance due to their relatively slower speed. If the collection of nucleation sites or single bubble growth due to heat influx is the primary formation principle of this size bubble, other bubbles shouldn't or should equally exist in the before and after the ultra-size bubble, respectively.

If a bubble which is greater than surrounding bubbles, is once formed for any reasons, it can continuously feed the front small bubbles thanks to its higher velocity. In this manner, coalescence in flowing can be ceaselessly happened and finally results in the bubbles consisting of the large bubble group in the size distribution. The possibility in formation of the initial large bubble which precipitates the continuous coalescence in flowing could be indirectly demonstrated by the previous experimental results of J.J. Xu et al [34]. They observed a sharp increase in bubble sliding velocity at the initial traveling moment, and this high velocity at early stage leads to growth of the sliding bubble by merging many undetached bubbles in its flowing way.

The valley in the size distribution, no bubble region, is the clue for discovering the origin of the size distribution with bi-modal shape. If this distribution shape is primarily attributed to the breakage of the bubbles with intermediate size or a bunch of merged nucleation sites, it is still mysterious why only the middle size bubbles are eliminated, whereas larger bubble which suffers from higher shear stress and needs the larger number of nucleation sites occupies more significant portion. Coalescence in flowing is the dominant mechanism for driving the bi-modal size distribution for the following reasons.

Figure 18 is a collection of the size distributions with increasing mass flow rate from 300 to 340 kg/m^2s under the same $\Delta T_{sub} = 34.0^\circ C$, $P=7.7 bar$, and $q=7.64 kW / m^2$. This collection presents that at higher mass flow rate two groups get closer with weaker small bubble group and shaper large bubble group. It was reported in V. Prodanovic et al. [8] that at lower flow rate convective heat transfer is lower, causing higher wall superheating under

the same heat flux, and this higher temperature activates the larger number of nucleation sites. Since correspondence is shown in dependencies of observed small bubble group in this study and reported nucleation sites on mass flow rate, it seems that small bubble group is related with activation of nucleation sites. Furthermore, it could be deduced that bubbles in small group are the raw ones from nucleation sites without undergoing significant coalescence in flowing.

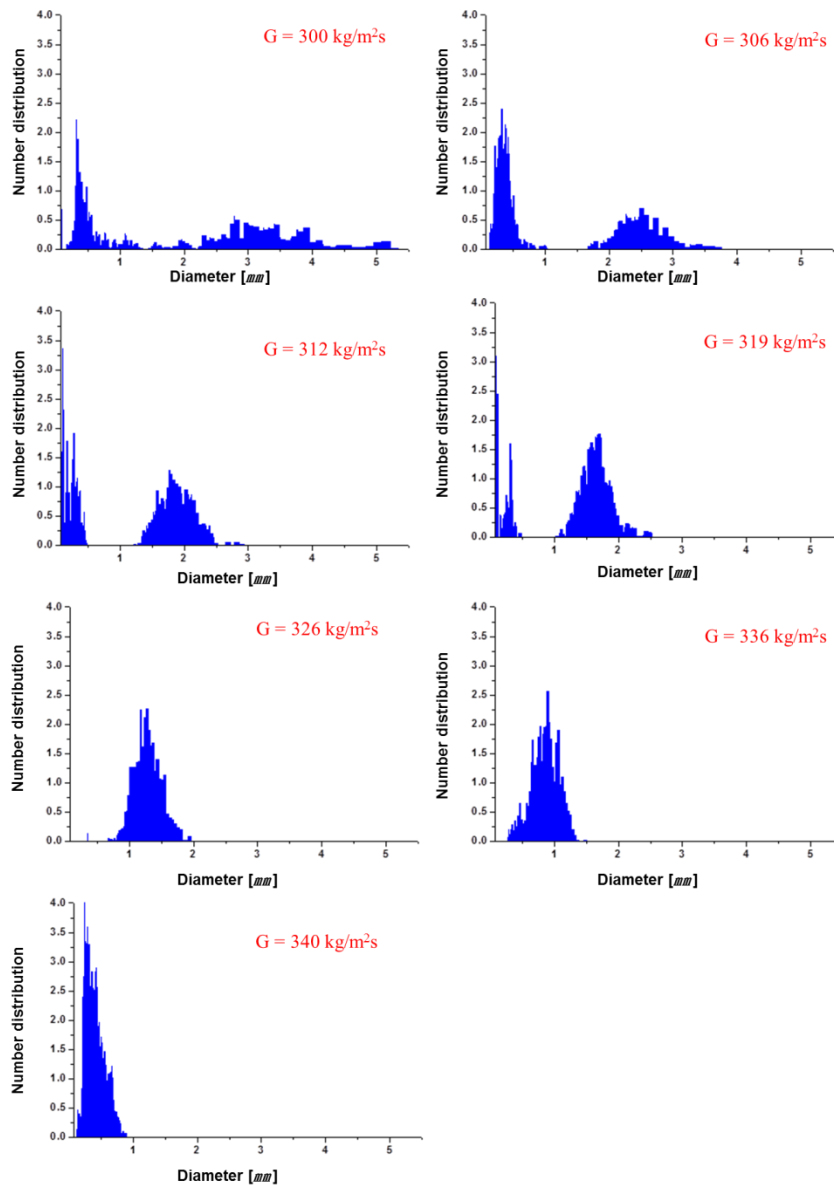


Figure 18 Collection of the size distributions with increasing mass flow rate from 300 to 340 $\text{kg/m}^2\text{s}$, adjusting $P = 7.7 \text{ bar}$, $\Delta T_{sub} = 34.0^\circ \text{C}$, and $q = 7.64 \text{ kW/m}^2$

On the other hand, large bubble group is likely to be constructed throughout sequential coalescence in flowing. The unique situation of halting the aforementioned ceaseless coalescence is when large bubbles with similar sizes and velocities are flowing with maintaining certain distances. This condition could be achieved easily at the stable situation

that bubbles are continuously generated in the same spots. This is the fundamental reason why medium size bubbles are not observed. Bubbles, which are created around the middle of the bubble generation region, potentially form medium bubble group. However, they were barely seen, because these bubbles had been fed by other bubbles, generated more upstream, before reaching the visualization section. In addition, bubbles in small group seem to be created just before the visualization section and they haven't preyed yet. And videos show a bunch of examples that bubbles with the size of small bubble group are merged by large bubbles.

As increasing mass flow rate, large bubbles have shorter time to coalesce due to faster bulk liquid and closer ONB location to exit, and simultaneously, small bubbles are less generated due to lower wall superheating. As a result, the size of large bubble group is reduced and the portion of small bubble group in the distribution decreases at higher mass flow rate. Additionally, the large bubble group becomes denser with sharper shape, and this is due to the observations that large bubbles over certain diameter have almost the same velocity, which is the converged one to that of bulk liquid, but otherwise, their velocities are proportional to the sizes, as illustrated in Figure 16. In the experimental conditions where the proportionality between velocities and sizes about the large bubble group exists, stricter conditions for stabilizing coalescence in flowing are recommended, because higher similarity in bubble sizes is required for maintaining the constant distances between them while flowing.. In other words, the proportionality leads to the unified size of the large

bubble group. From $326 \text{ kg/m}^2\text{s}$ of mass flow rate, two groups are eventually combined and at $340 \text{ kg/m}^2\text{s}$, only small bubble group was remained.

Figure 19 is one of the observed bubble populations, and it additionally emphasizes the importance of coalescence in flowing in the present experiments. As increasing flow rate from the lowest point, more nucleation sites are suppressed due to lower wall superheating, and it was expressed as the results of declining in bubble population in Figure 19. The slope of the population is drastically decreases, note that the population is described by semi-log plot with a logarithmic scale on the y-axis, and it indicates weaker influence of mass flow rate on the population at higher mass flow rate. However, less activated nucleation sites couldn't be the perfect cause of the population drop, because of the sudden inclination of it at the highest population, which was commonly found in the experimental results. Bubble coalescence in flowing is obviously less happened at higher flow rate due to lower collision opportunities of sparser and smaller bubbles. Figure 20 is the imaginary frequencies of bubble generation at the activated nucleation sites and occurred coalescence in flowing with respect to mass flow rate and this clearly explain every remarked aspect of the population above. Due to declining in the frequencies of both events with different curves, and the differences between them, which can represent the number of survived bubbles and leads to the bubble population, can have the aspects of increasing after decreasing. It should be stressed that Figure 20 is just imaginary diagram for explaining the population, and they were not measured in the present experiments as well as haven't been proven in the previous studies.

In summary, the observed bubbles are presumed to be the outcome of coalescence in flowing and this estimation is supported by several unusual features in the results of experiments. Since the bubble patterns could govern the effectiveness of heat transfer, coalescence in flowing will be intensively investigated in this paper.

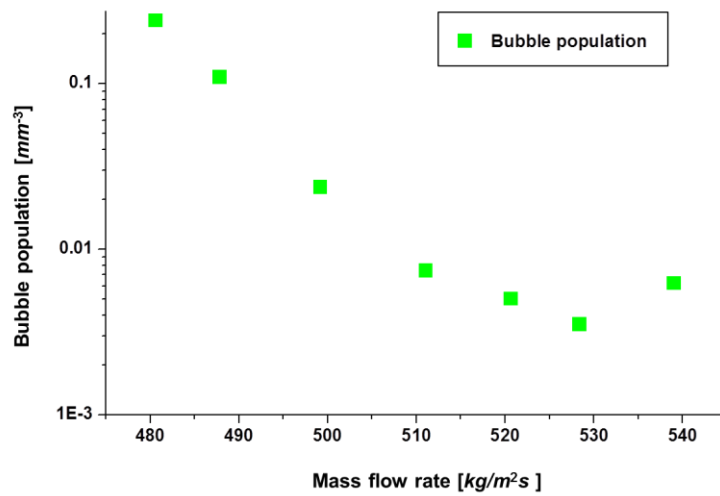


Figure 19 Bubble population at $\Delta T_{sub} = 35.0^\circ C$, $P = 7.7 \text{ bar}$, and $q = 13.21 \text{ kW/m}^2$

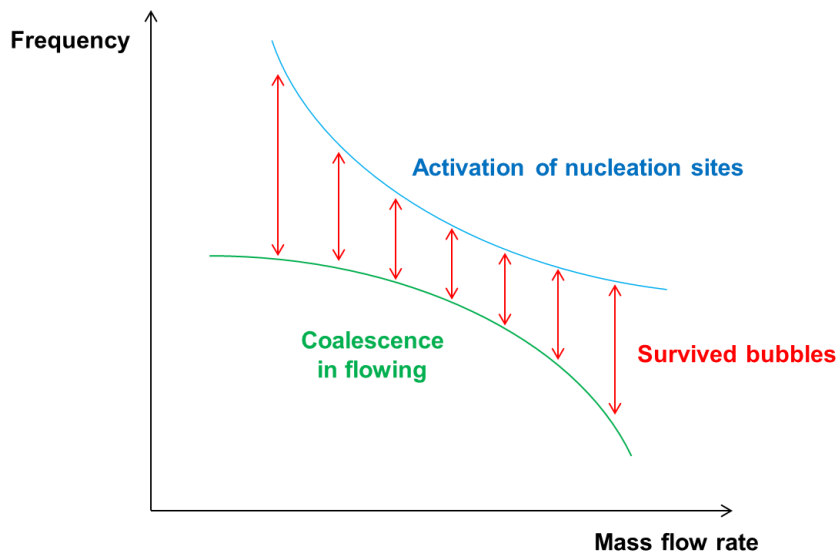


Figure 20 Imaginary frequencies of bubble departure and coalescence in flowing

4.2 The influence of single parameter on bubble characteristics

4.2.1 Mass flow rate and inlet subcooling

In extracting the bubble characteristics from the distribution, averaging could lead to a significant loss of information and wrong results, as pointed out by R. Maurus et al. [11]. In the obtained size distributions with bi-modal shape, the side effect of averaging could be more severe, and actually high level of irregularity was found in averaged data, as illustrated in Figure 21. The average bubble diameter around $G = 300 \text{ kg} / \text{m}^2 \text{ s}$ has somewhat regularity with respect to only mass flow rate, not inlet subcooling, but serious randomness is found the results around $G = 500 \text{ kg} / \text{m}^2 \text{ s}$. The size distributions gained around $G = 300$ and $500 \text{ kg} / \text{m}^2 \text{ s}$ at $\Delta T_{sat} = 35.0 \text{ }^\circ \text{C}$ are presented in Figure 22. The two bubble groups are exactly appeared in the distribution around $300 \text{ kg} / \text{m}^2 \text{ s}$, on the other hand, the small bubble group dominates the whole distribution around $500 \text{ kg} / \text{m}^2 \text{ s}$. But the existence of the large bubble group is clearly revealed in its volume distribution presented in Figure 23.

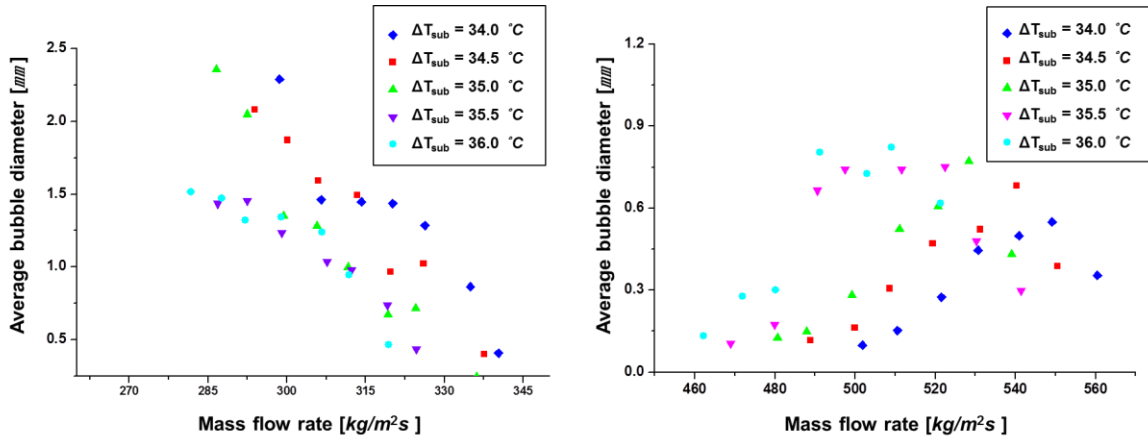


Figure 21 Average bubble diameters with respect to mass flow rate and inlet subcooling around $G = 300$ (left) and $500 \text{ kg/m}^2\text{s}$ (right)

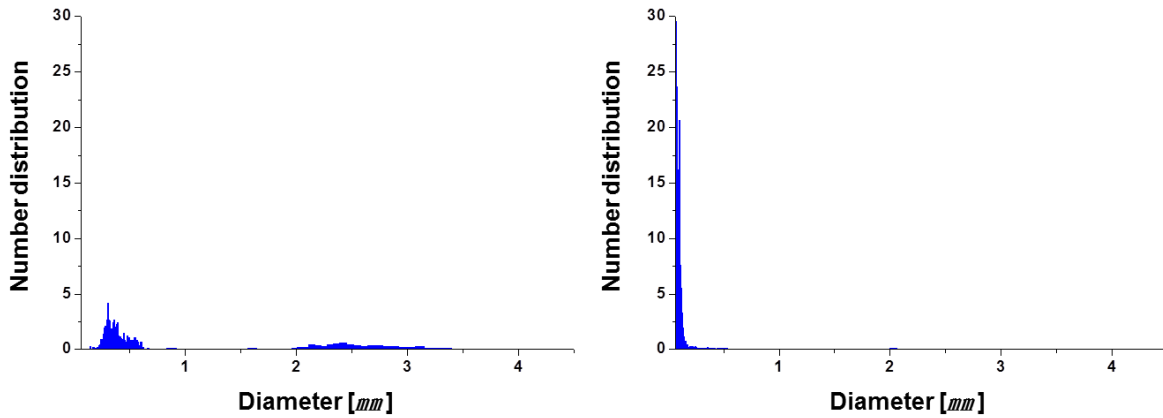


Figure 22 Size distributions around $G = 300$ (left) and $500 \text{ kg/m}^2\text{s}$ (right) at $\Delta T_{sub} = 35.0^\circ\text{C}$

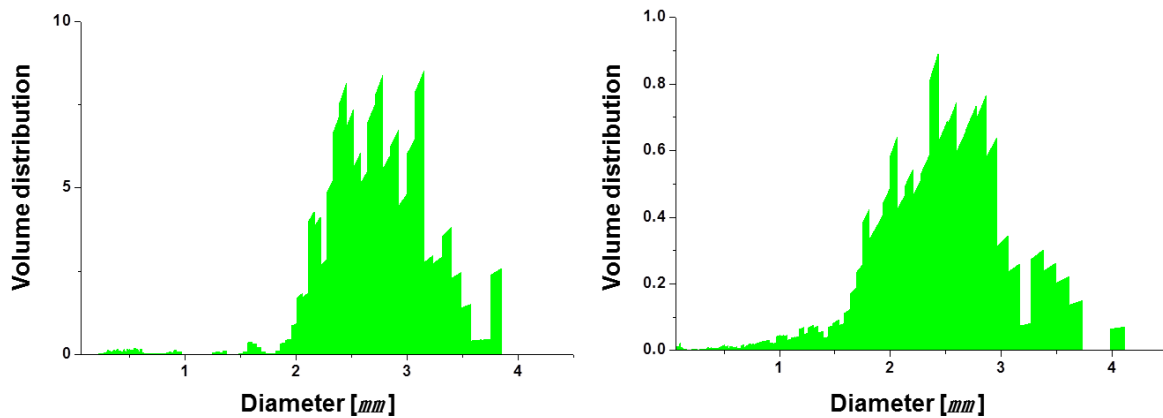


Figure 23 Volume distributions around $G = 300$ (left) and $500 \text{ kg/m}^2\text{s}$ (right) at $\Delta T_{sub} = 35.0^\circ\text{C}$

Figure 24 shows the modal bubble diameters of the large bubble group around $G = 300$ and $500 \text{ kg} / \text{m}^2 \text{ s}$ with linear interpolation lines gained from least square method, and the results present the distinct dependencies of the modes on both mass flow rate and inlet subcooling. It is illustrated that the modes are decreasing with increasing mass flow rate or inlet subcooling. Since the large bubble group is the outcome of numerous merged bubbles, it is expected that the three major factors determine sizes of the large bubble group: 1) how far the point of ONB is from the visualization section, 2) how big bubbles are departed, and 3) how much bubbles are generated, as a coalescence source. U. Puli et al [10], Y.Y. Hsieh et al [14], and C.P. Yin et al [21] have shown bubble departure size decreases with increasing mass flow rate or inlet subcooling. And they also pointed out that higher wall superheating under the same heat flux, induced by the increments of two parameters, is the direct cause of the smaller departed bubbles. The positive correlation between the mode and wall superheating from the present experiments is provided in Figure 25, and this result agrees with those of A.A. Voloshko et al. [35] and V.S. Golorin et al. [36]. Figure 26 is the dependence of the mode on theoretical ONB location from the model of Manon(1999), and the plot indicates that the further ONB is placed from the exit, the bigger the observed mode of large bubble group is. This feature proves the influence of the first mentioned major factor which may affect to the mode.

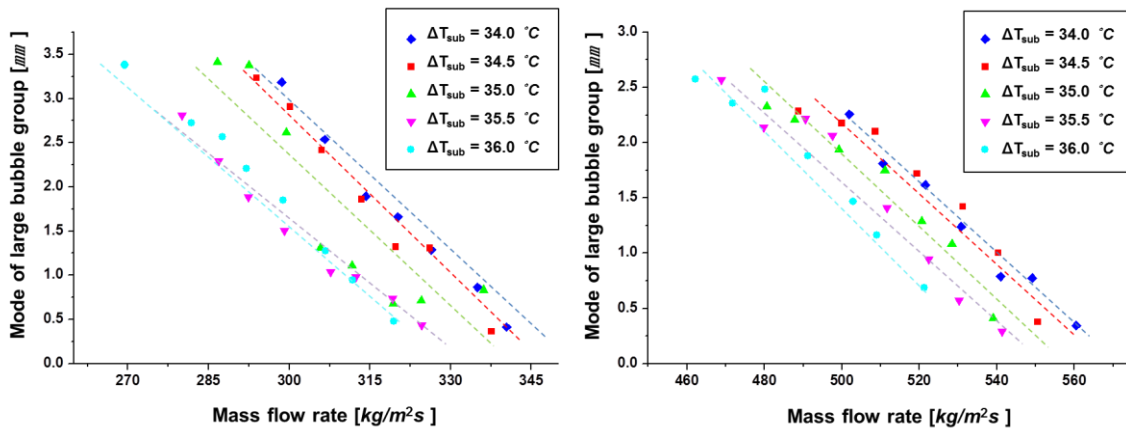


Figure 24 Mode of large bubble group with respect to mass flow rate and inlet subcooling around $G = 300$ (left) and $500 \text{ kg/m}^2\text{s}$ (right)

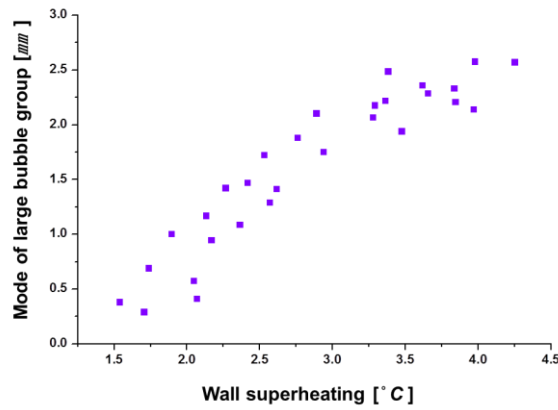


Figure 25 Mode of large bubble group with respect to wall superheating around $G = 500 \text{ kg/m}^2\text{s}$

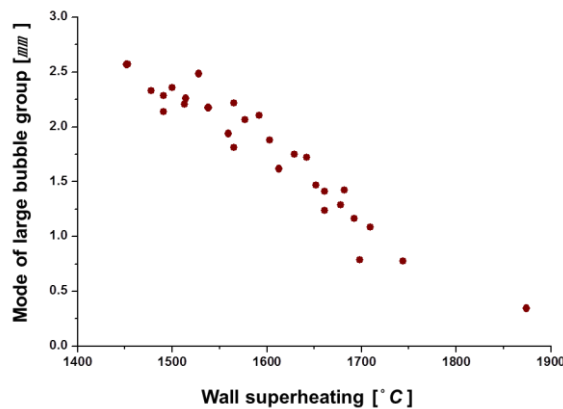


Figure 26 Mode of large bubble group with respect to predicted ONB location around $G = 500 \text{ kg/m}^2\text{s}$

Figure 27 is the bubble population at both mass flow rate regions. The population in the results shows declining aspects with slightly upward tail, as described in 4.1. While the population around $G = 500 \text{ kg} / \text{m}^2\text{s}$ is drastically declined with respect to both mass flow rate and inlet subcooling, around $G = 300 \text{ kg} / \text{m}^2\text{s}$ it is relatively flat except for two conspicuous points. Note that both diagrams use the same logarithmic scale in y-axis. This different influence of mass flow rate on bubble population agrees with the observation of R. Maurus et al [11]. In addition, as shown in L. zou [9], the population has a close relation with wall superheating and this was discovered in the present experiments, as shown in Figure 28.

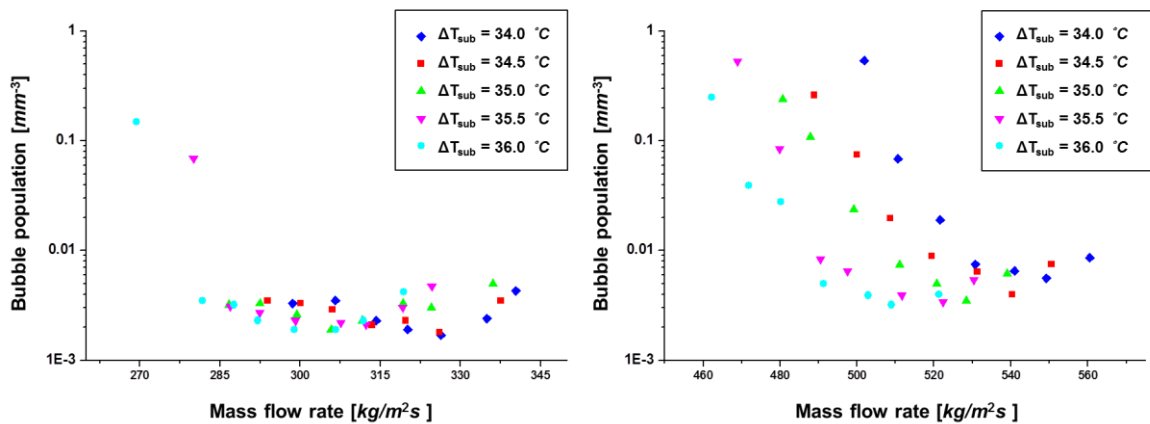


Figure 27 Bubble population with respect to mass flow rate and inlet subcooling around $G = 300$ (left) and $500 \text{ kg}/\text{m}^2\text{s}$ (right)

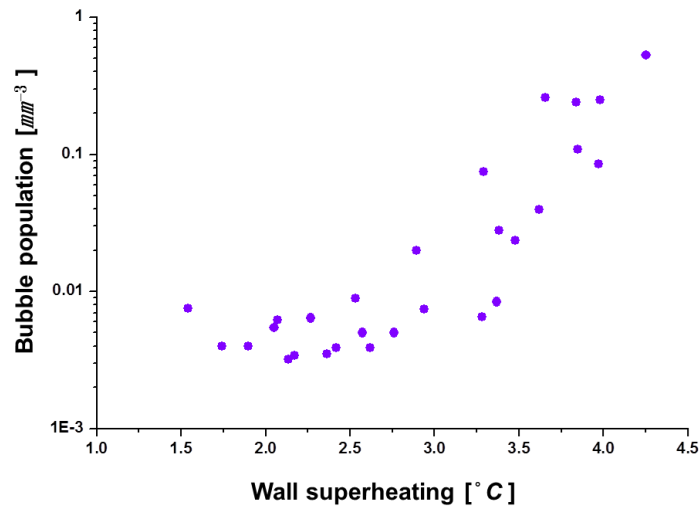


Figure 28 Bubble population with respect to wall superheating around $G = 500 \text{ kg/m}^2\text{s}$

Interfacial area concentration and void fraction show the analogous tendencies with that of the bubble population, as presented in Figure 29 and 30. This is obvious because these three bubble characteristics were calculated based on the number of bubbles. From the void fraction results, the used model of predicting the point of OSV in this study could be qualitatively demonstrated thanks to the fact that OSV is an indicator of the location where a small change in condition cause a substantial variation in the void fraction value [37]. Thus, if the actual OSV location is beyond the visualization section, the measured void fraction would be definitely small. In other words, by tracing the sudden change in void fraction, validity of the OSV prediction model could be verified. The obtained void fraction and the predicted OSV location are drawn in one diagram in Figure 31 and it was confirmed that the mass flow rate where the predicted OSV is reached to the visualization glass location (1918 mm) is where slopes of void fraction show drastic change. As a result, the

used OSV model in the present study, Saha and Zuber (1974), which has been used for vertical channel in common, is also applicable to horizontal channel.

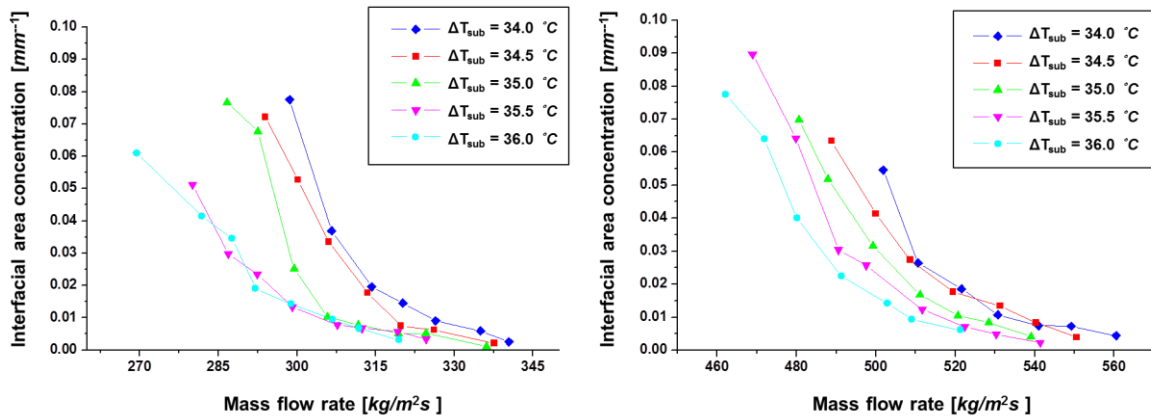


Figure 29 Interfacial area concentration with respect to mass flow rate and inlet subcooling around $G = 300$ (left) and $500 \text{ kg/m}^2\text{s}$ (right)

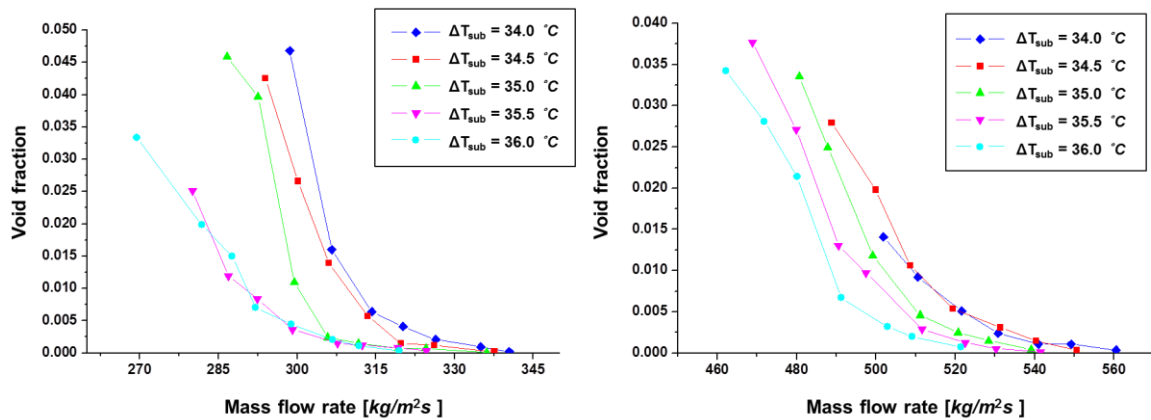


Figure 30 Void fraction with respect to mass flow rate and inlet subcooling around $G = 300$ (left) and $500 \text{ kg/m}^2\text{s}$ (right)

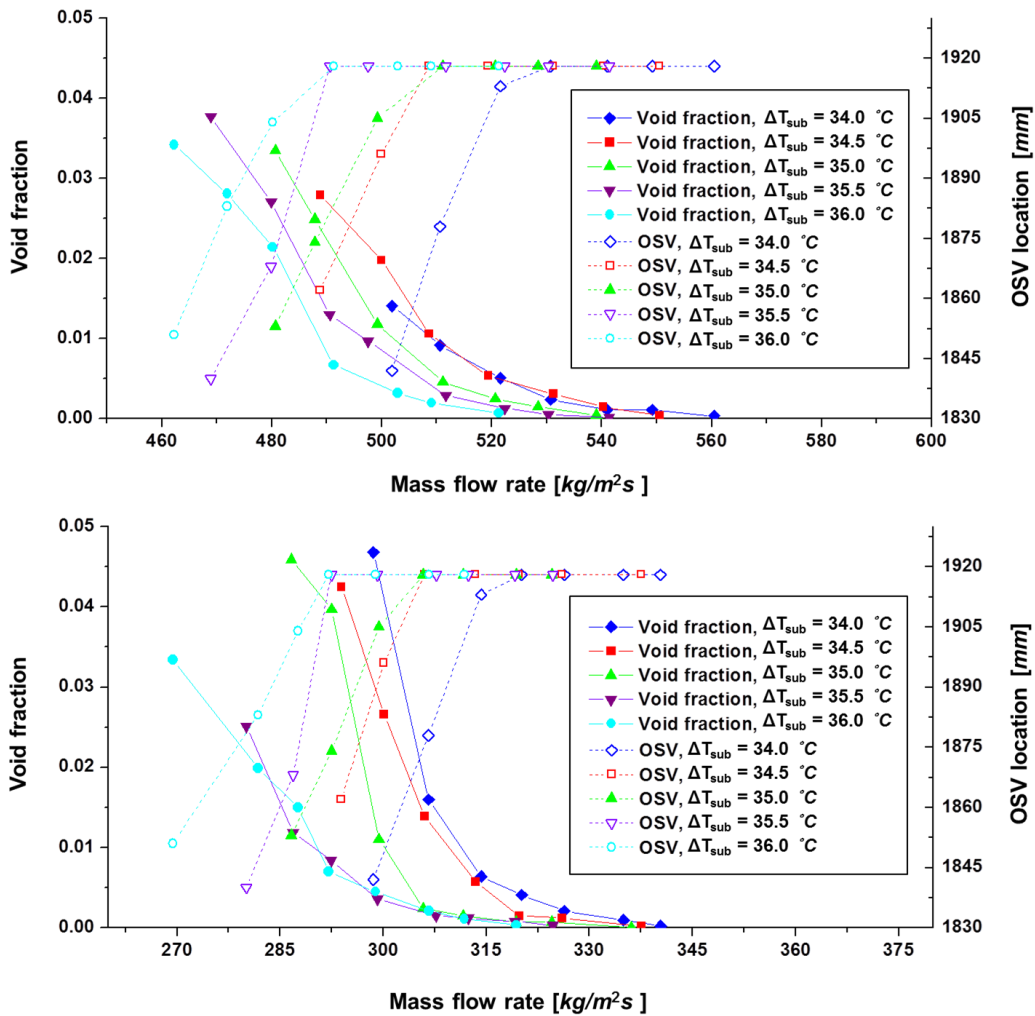


Figure 31 Relation between void fraction and predicted OSV location with respect to mass flow rate and inlet subcooling around $G = 300$ (top) and $500 \text{ kg/m}^2\text{s}$ (bottom)

After separating two size groups in the size distribution, variance of the large bubble group and kurtosis of the small bubble group can be calculated and they are presented in Figure 32 and 33 respectively. In principle, the variance is larger at lower mass flow rate or lower inlet subcooling in both experiment sets. Higher variance, indicating broader size distribution, at lower mass flow and lower inlet subcooling is caused by the sliding velocities proportional to sizes, as described in 4.1. Meanwhile, when coalescence in flowing is promoted too much,

the number of bubbles in the large bubble group could be rather smaller, and this is due to the fact that large bubbles are the collection of small bubbles. This can cause the sudden decline of the variance at the severe bubble coalescence condition, as observed in the lowest mass flow rate around $500 \text{ kg} / \text{m}^2\text{s}$ of Figure 32.

Kurtosis of the small bubble group shows distinct tendencies around $G = 500 \text{ kg} / \text{m}^2\text{s}$ for both mass flow rate and inlet subcooling: decline of kurtosis as increasing mass flow rate and inlet subcooling. Although the tendency around $G = 300 \text{ kg} / \text{m}^2\text{s}$ seems to be ambiguous, this is because of small absolute values of the kurtosis and the fluctuations within them were dismissed in this analysis. Conceptually, the kurtosis is highly dependent on how much small bubbles are observed and this seems to be affected by the extent of the activated nucleate sites. This presumption could be proven by investigating the relation between kurtosis and wall superheating. Figure 34 shows that the kurtosis drastically increases with increasing wall superheating. Furthermore, the validity of the OSV model could be once more evaluated by the kurtosis, because it can be a similar indicator with void fraction in terms of bubble creation. Since the kurtosis relies on the nucleation sites density nearby the tube exit, the value of it would be changed as to whether the predicted OSV is before the exit or not, if the model predict the exact OSV location. Figure 35 shows the points which the slope of kurtosis lines are changed is exactly where the predicted OSV locations indicate the tube exit.

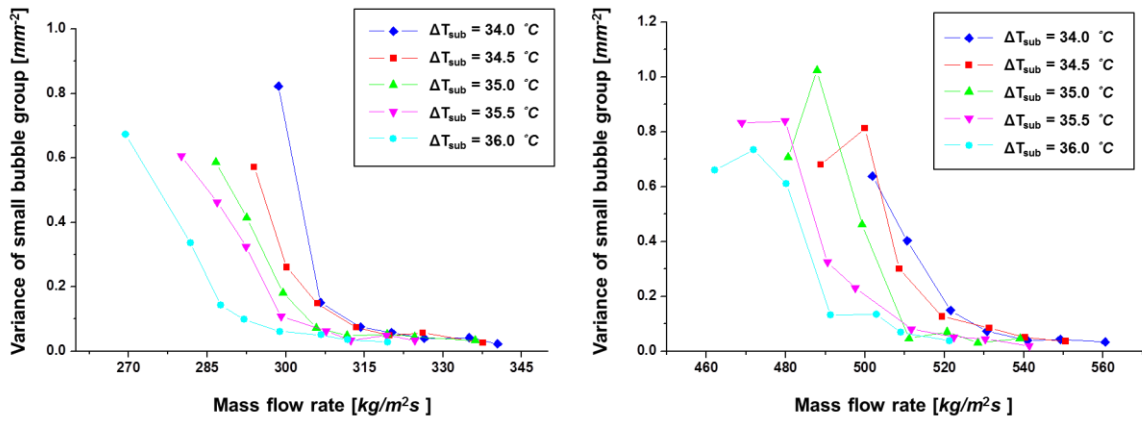


Figure 32 Variance of large bubble group with respect to mass flow rate and inlet subcooling around $G = 300$ (left) and 500 kg/m^2s (right)

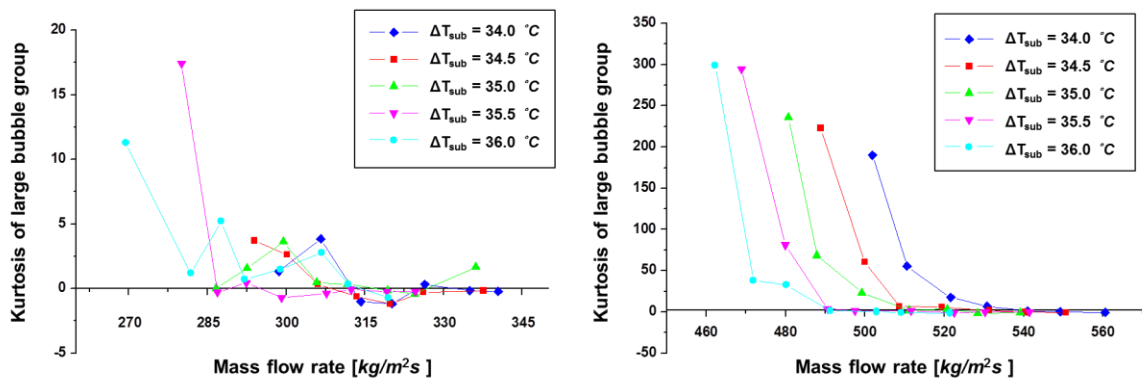


Figure 33 Kurtosis of small bubble group with respect to mass flow rate and inlet subcooling around $G = 300$ (left) and 500 kg/m^2s (right)

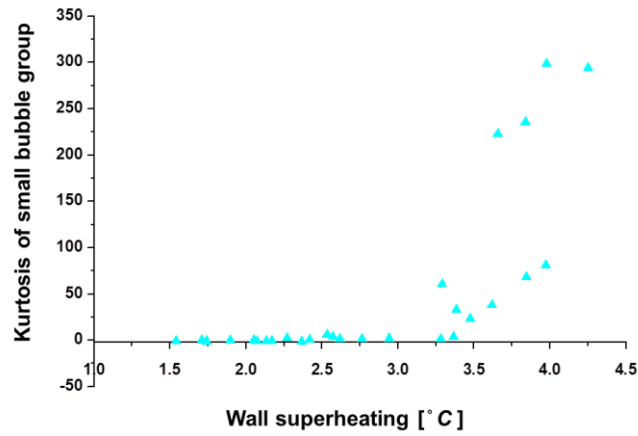


Figure 34 Kurtosis with respect to wall superheating with respect to mass flow rate and inlet subcooling around $G = 500 \text{ kg/m}^2\text{s}$

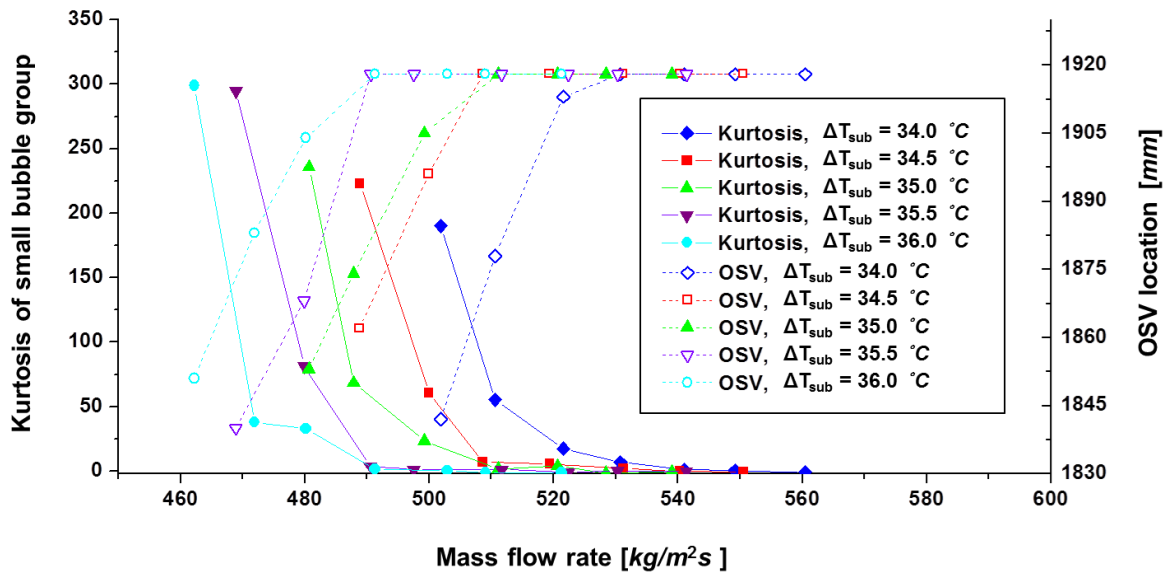


Figure 35 Relation between kurtosis of small bubble group and predicted OSV location mass flow rate and inlet subcooling around $G = 500 \text{ kg/m}^2\text{s}$

At last, average sliding bubble velocity with respect to mass flow rate and inlet subcooling is presented in Figure 36. It was observed that regardless of increased bulk liquid velocity, the average sliding bubble velocity is maintained, and even decreases at the highest mass flow rate in each inlet subcooling. This result is acceptable because larger bubbles which have higher sliding velocity are main components of the size distribution at lower mass flow rate. Note that the sliding bubble velocities approach and are finally converged to bulk liquid velocity at decreasing mass flow rate. The above results agree with those of S. Li et al [15].

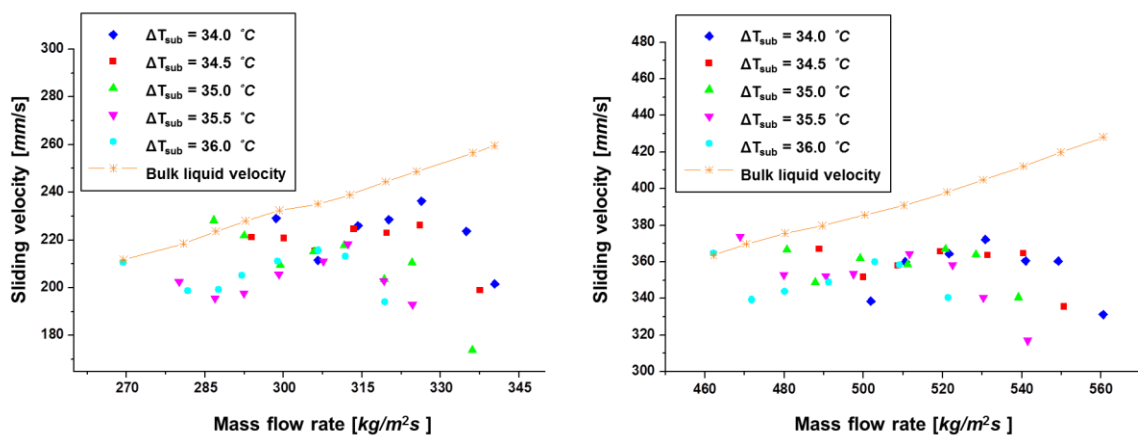


Figure 36 Average sliding bubble velocities and bulk liquid velocities with respect to mass flow rate and inlet subcooling around $G = 300$ (left) and $500 \text{ kg/m}^2\text{s}$ (right)

4.2.2 Heat flux

Y.M. Lie et al. [3] showed higher bubble departure frequency, R. Maurus et al. [38] stated longer life time of lift-off bubbles, and L. Zou [9] reported higher nucleation sites density, at higher heat flux. These results could be led to higher bubble population at higher heat flux, reported in Y.M. Lie et al. [3], S. Li et al. [15], and C.P. Yin et al. [21]. Meanwhile, Y.M. Lie et al. [3] and Y.Y. Hsieesh et al. [14] observed the severe interactions between bubbles at the nucleation sites at high heat flux by photographic study. S. Li [15] reported that bubble sliding velocity increases with increasing heat flux at first, but decreases after the heat flux is over a certain level.

These previous experimental results for incipience of bubbles could be used for explaining the observations of the present study. Figure 37-40 show every bubble characteristics discussed in the previous section for the experiment sets of varying heat flux. Average bubble diameter and mode of the large bubble group increase in principle with increasing heat flux as seen in Figure 37. Population, interfacial area concentration, and void fraction in Figure 38 are higher at higher heat flux, showing similar growing trends. Variance of the large bubble group and kurtosis of the small bubble group in Figure 39 rise with increasing heat flux. As presented in Figure 40, bulk liquid velocity is increasing with increasing heat flux, due to lower liquid density caused by higher core liquid temperature, and the relative velocity of sliding bubble with respect to bulk liquid is reduced as increasing heat flux.

An interesting point in the results is existed in the experimental case of $q = 7.83 \text{ kW} / \text{m}^2 \text{ s}$ and $G = 300 \text{ kg} / \text{m}^2 \text{ s}$. It is observed that tiny bubbles, whose diameters are less than 0.3 mm, begin to be explosively generated from this point. Figure 41 is two images taken from this point and from the point one before. The bubbles with small sizes, which have continuously existed at the higher heat flux condition than $7.83 \text{ kW} / \text{m}^2$, are suddenly disappeared at the condition of one step smaller heat flux, $q = 7.64 \text{ kW} / \text{m}^2$. This result indicates the existence of heat flux criterion for small bubble generation which wasn't shown in the experiments with varying mass flow rate and inlet subcooling. This phenomenon is appeared in the analysis results as both sudden reduction in average bubble diameter in Figure 37 and abrupt increment of kurtosis of small bubble group in Figure 39. Moreover, where the predicted OSV location points out the tube exit is $7.83 \text{ kW} / \text{m}^2$, and this fact also indicates the sharp change of bubble generation in the vicinity of OSV point. Note that these sudden variations are found only at $G = 300 \text{ kg} / \text{m}^2 \text{ s}$ experimental case, not at $500 \text{ kg} / \text{m}^2 \text{ s}$, where far greater number of tiny bubbles are consistently flowing.

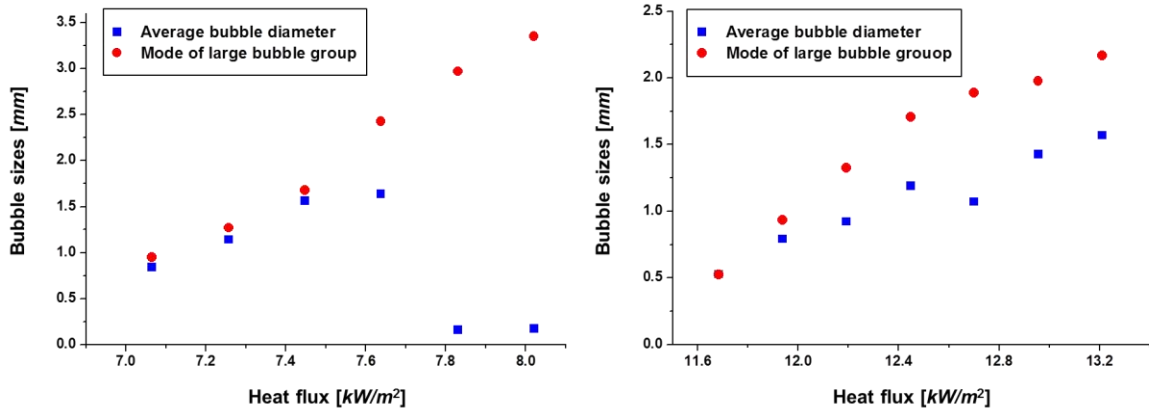


Figure 37 Average bubble diameter and mode of large bubble group with respect to heat flux at $G = 300$ (left) and $500 \text{ kg/m}^2\text{s}$ (right)

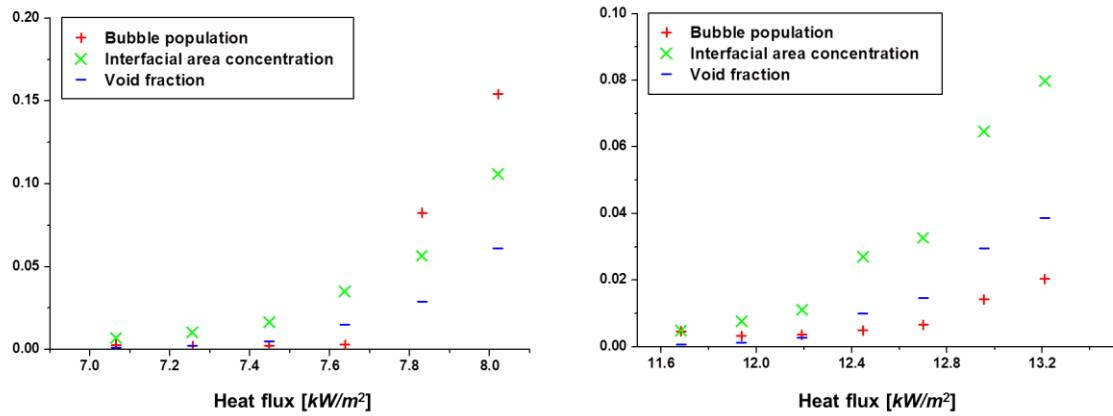


Figure 38 Population, interfacial area concentration, and void fraction with respect to heat flux at $G = 300$ (left) and $500 \text{ kg/m}^2\text{s}$ (right)

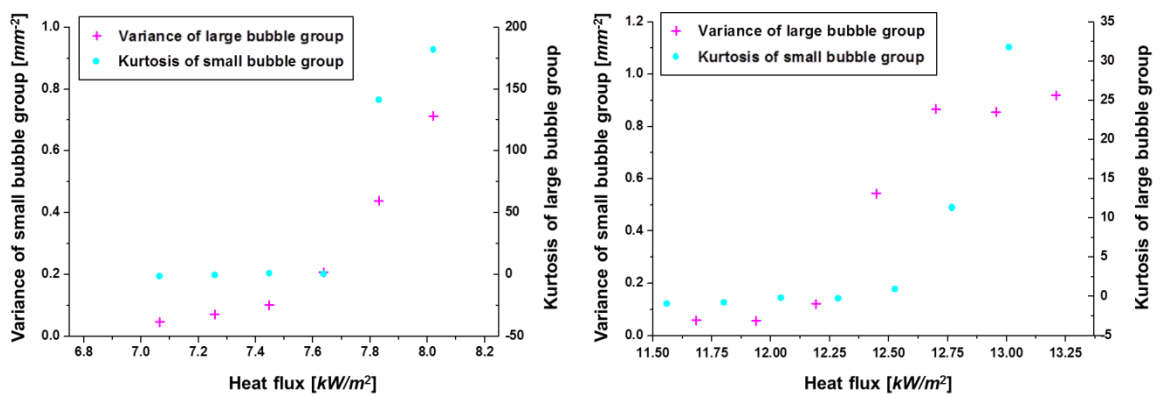


Figure 39 Variance of large bubble group and kurtosis of small bubble group with respect to heat flux at $G = 300$ (left) and $500 \text{ kg/m}^2\text{s}$ (right)

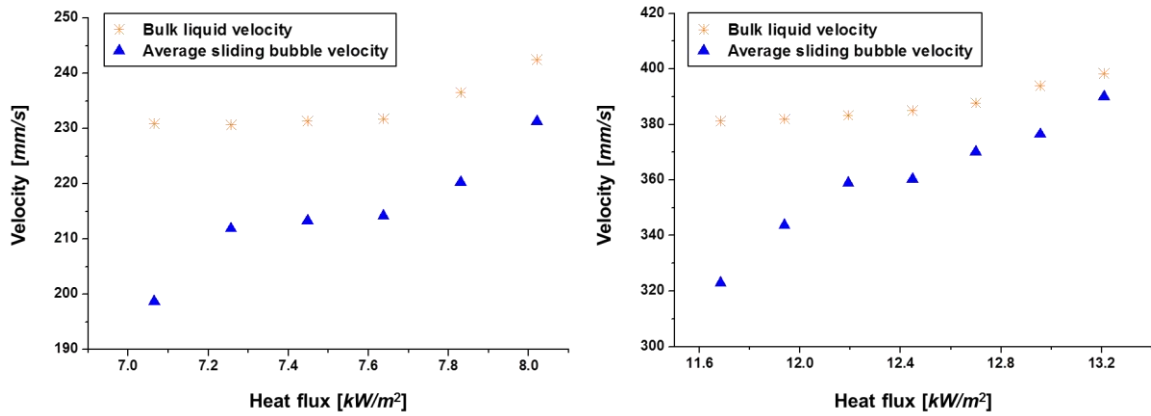


Figure 40 Average sliding bubble velocity and bulk liquid velocity with respect to heat flux at $G = 300$ (left) and 500 kg/m²s (right)

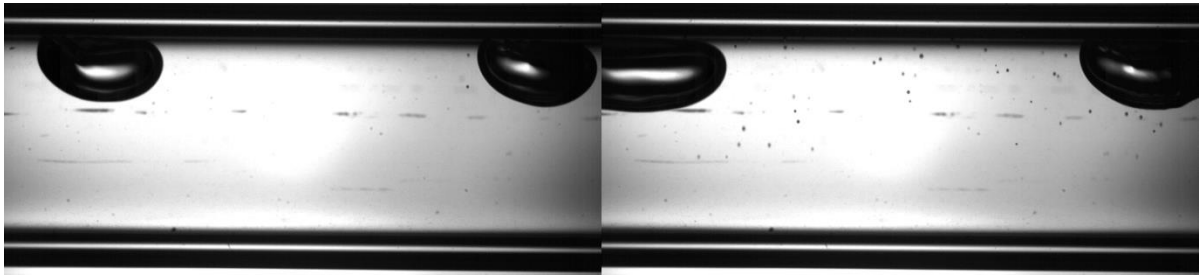


Figure 41 Captured images at $q = 7.64$ (left) and 7.83 kW/m² (right)

4.2.3 Pressure

With increasing pressure, average bubble diameter increases at the experimental set with $G = 300$ kg / m²s , while is stagnant at 500 kg / m²s except for two points at the lowest pressure, and mode of the large bubble group increases in both experimental sets, as presented in Figure 42. The

different tendencies of average bubble diameter in two cases are due to different portion of bubble size groups in size distribution. The results about the modes are more likely to have been applied in the average bubble diameter at $G = 300 \text{ kg} / \text{m}^2 \text{ s}$, where both bubble size groups have similar fractions. On the other hand, V. Prodanovic et al [8], L. Zou [9], U. Puli et al. [10], and V.I. Tolubinsky et al. [39] showed the declination of bubble departure size with increasing pressure due to longer contact time between bubble and heated surface and it seems that this has been reflected in the result of average bubble diameter at $G = 500 \text{ kg} / \text{m}^2 \text{ s}$, where the small bubble group absolutely dominates the size distribution. Different absolute values of the kurtosis between two sets in Figure 43 demonstrate the different portion of the small bubble group between them.

Rise in population, in accordance with the increase of interfacial area concentration and void fraction, with higher pressure is illustrated in Figure 44 and this is in accordance with the previous results of V. Prodanovic et al [8] and L. Zou [9], which observed inclination of nucleation sites density at higher pressure. In Figure 45, slight decrease of average sliding bubble velocity, despite of increase of bulk liquid velocity. This result may be attributed to higher surface tension of bubbles at higher pressure, as reported in L. Zou [9].

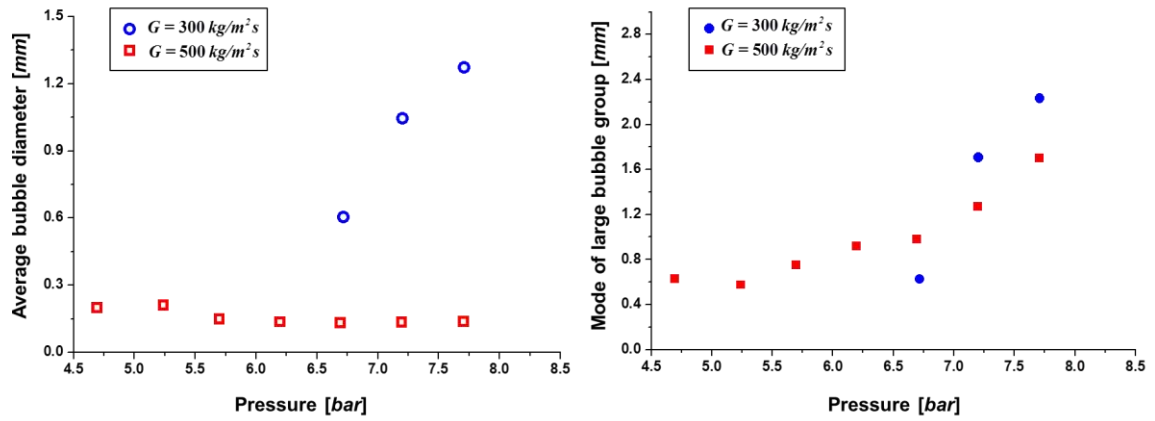


Figure 42 Average bubble diameter (left) and mode of large bubble group (right) with respect to pressure at $G = 300$ and $500 \text{ kg/m}^2\text{s}$

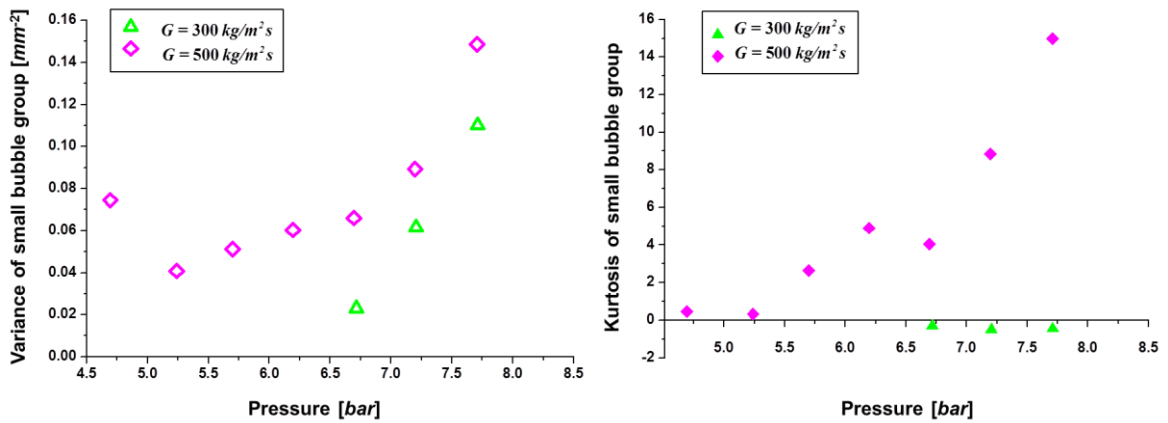


Figure 43 Variance of large bubble group (left) and kurtosis of small bubble group (right) with respect to pressure at $G = 300$ and $500 \text{ kg/m}^2\text{s}$

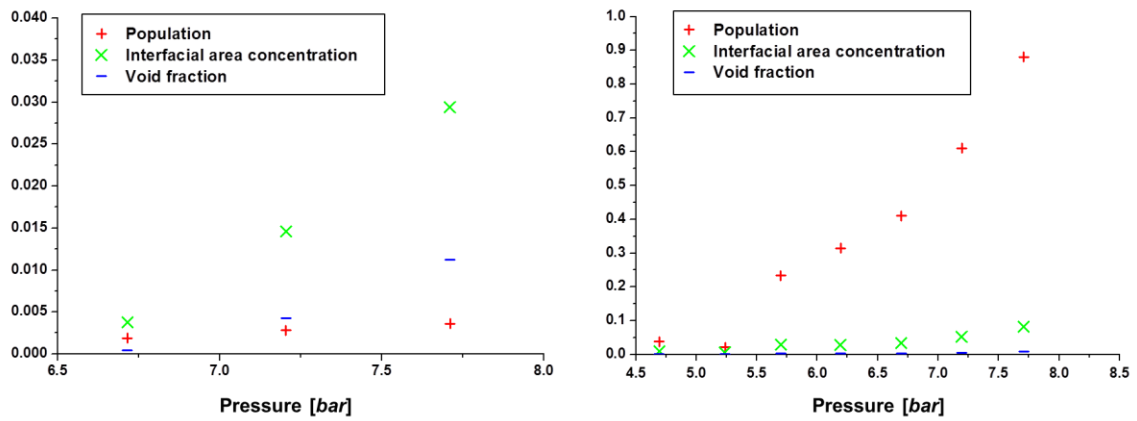


Figure 44 Population, interfacial area concentration, and void fraction with respect to pressure at $G = 300$ (left) and $500 \text{ kg/m}^2\text{s}$ (right)

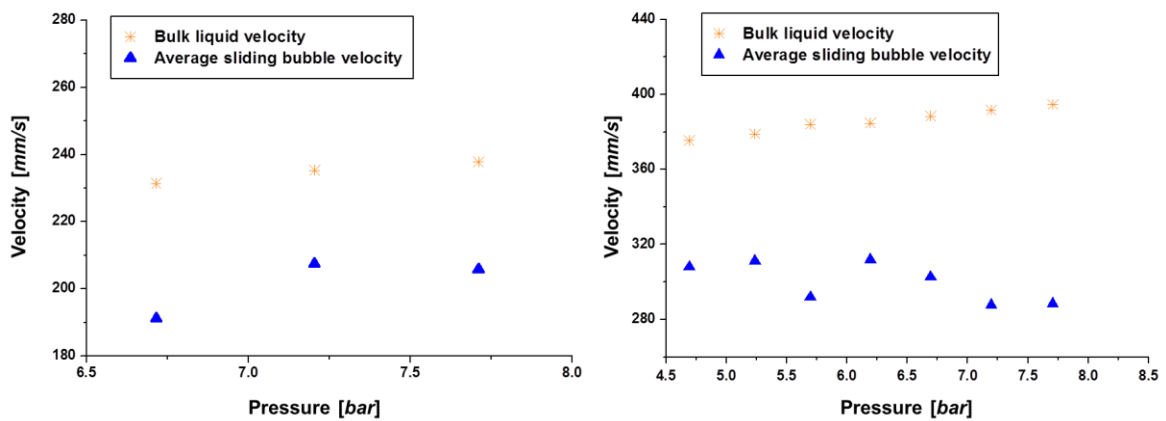


Figure 45 Average sliding bubble velocity and bulk liquid velocity with respect to pressure at $G = 300$ (left) and $500 \text{ kg/m}^2\text{s}$ (right)

Two remarkable issues are drawn from the results at $G = 500 \text{ kg/m}^2\text{s}$. In Figure 46, from 5.2 bar of pressure, the predicted ONB and OSV locations are almost invariable depending on pressure, in spite of increase of mode of large bubble group. In this case, among three decisive factors of large bubble group presented in 4.2.1, location of ONB is conserved and bubble departure sizes are estimated to decrease as mentioned. Therefore, increment of size

of large bubble group results from only increase of nucleation sites density, offsetting other two disadvantageous effects.

Secondary issue is hold-up of wall superheating from 5.7 *bar*, as shown in Figure 47.

Despite of stagnant wall superheating, increment of bubble population was observed. Since mass flow rate, inlet subcooling, and heat flux are the same between the experimental cases, the increase of population is solely attributed to increasing pressure. In conclusion, two issues lead to the conclusion of the strong influence of pressure on nucleation sites density.

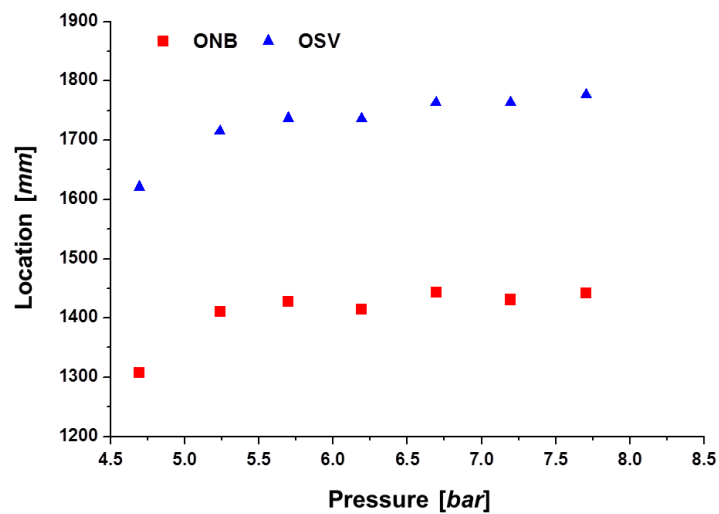


Figure 46 Predicted ONB and OSV location with respect to pressure at $G = 500 \text{ kg/m}^2\text{s}$

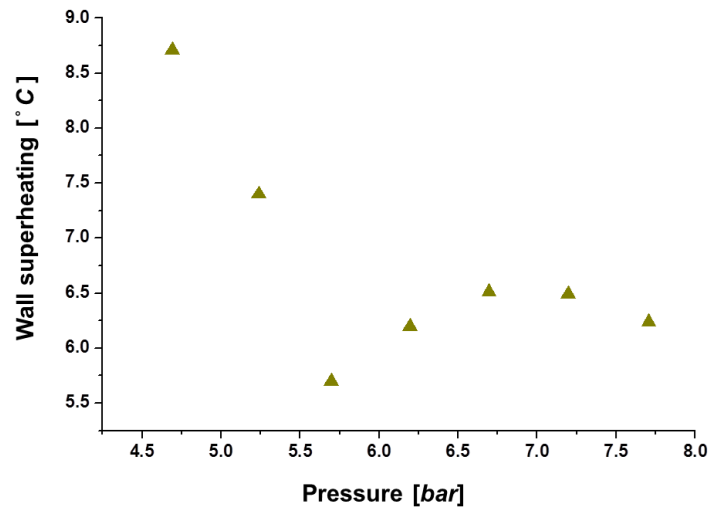
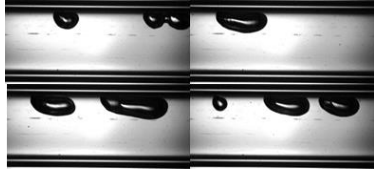

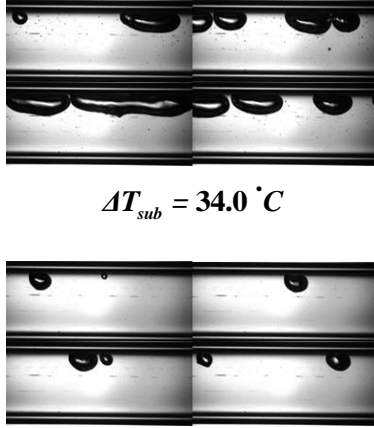
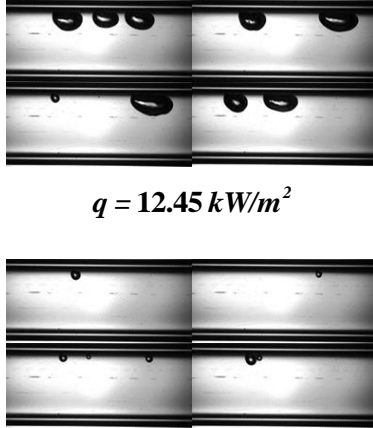
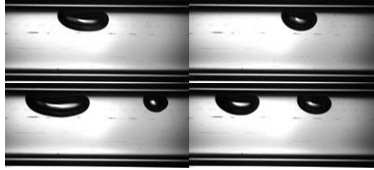

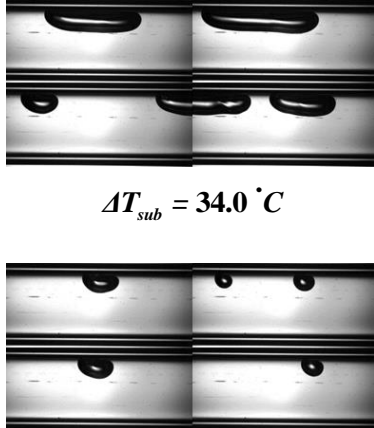
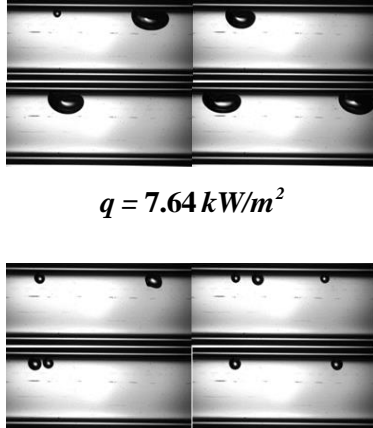


Figure 47 Wall superheating with respect to pressure at $G = 500 \text{ kg/m}^2\text{s}$

At last, a collection of photos, representing the four parametric influences is presented in Table 10. The effects of parameters which have been described as quantitative data can be inspected throughout investigating the following bubble images.

Table 10 Photos of bubbles varying operating conditions from the basic ones: $P = 7.7 \text{ bar}$ and $\Delta T_{sub} = 35.0^\circ \text{C}$

| Basic conditions | Pressure variations | Inlet subcooling variations | Heat flux variations |
|--|--|---|--|
| <p>$G = 500 \text{ kg/m}^2 \text{ s}$</p>  <p>$P = 7.7 \text{ bar}$ $\Delta T_{sub} = 35.0^\circ \text{C}$ $q = 13.21 \text{ kW/m}^2$</p> |  <p>$P = 6.2 \text{ bar}$ $P = 4.7 \text{ bar}$</p> |  <p>$\Delta T_{sub} = 34.0^\circ \text{C}$ $\Delta T_{sub} = 36.0^\circ \text{C}$</p> |  <p>$q = 12.45 \text{ kW/m}^2$ $q = 11.68 \text{ kW/m}^2$</p> |
| <p>$G = 300 \text{ kg/m}^2 \text{ s}$</p>  <p>$P = 7.7 \text{ bar}$ $\Delta T_{sub} = 35.0^\circ \text{C}$ $q = 7.64 \text{ kW/m}^2$</p> |  <p>$P = 7.2 \text{ bar}$ $P = 6.7 \text{ bar}$</p> |  <p>$\Delta T_{sub} = 34.0^\circ \text{C}$ $\Delta T_{sub} = 36.0^\circ \text{C}$</p> |  <p>$q = 7.64 \text{ kW/m}^2$ $q = 7.06 \text{ kW/m}^2$</p> |

4.3 Coupling effect of heat flux and inlet subcooling on bubble characteristics

Figure 48-50 are the experimental results of experimental set 7 and 8 which were conducted for investigating coupling effects of heat flux and inlet subcooling. The results were plotted with respect to heat flux only and the inlet subcooling conditions were marked at each case. As increasing both heat flux and inlet subcooling simultaneously, both average bubble diameter and mode of the large bubble group increase, as illustrated in Figure 48. Population is maintained, while interfacial area concentration and void fraction rise with increasing both heat flux and inlet subcooling, as shown in Figure 49. Relative velocity between sliding bubbles and bulk liquid becomes closer at higher heat flux and higher inlet subcooling, as shown in Figure 50. Since larger bubbles are flowing at this condition, increment of average sliding bubble velocity is likely to be reasonable.

Y.M. Lie et al [3] and Y.Y. Hsiesh et al [14] have demonstrated that at higher heat flux, more bubbles are merged at the nucleation sites. Even though their reports are about the experiments that heat flux is only manipulated parameter, it could be applied to the present results of the experimental set 7 and 8 throughout inspection of wall superheating behaviors, presented in Figure 51. Since the outlet qualities were tuned to have the same value in every experimental case, all of core liquid temperatures at outlet are the same, therefore, higher wall superheating means higher temperature of liquid in vicinity of the heated surface and more developed temperature gradients in radial direction in the heated tube. An interesting feature in the results is this higher wall superheating affects to only the bubble sizes, not the population. This feature leads to constant population and increase interfacial area concentration and void fraction along with increasing both heat flux and inlet subcooling, as shown in Figure 49. This unusual aspect may result from the fact that the number of activated cavities is confined by relatively cold surrounding liquid, and excess energy from high heat flux, which is transferred in the form of boiling heat transfer, is used for increasing the bubble size at each cavity.

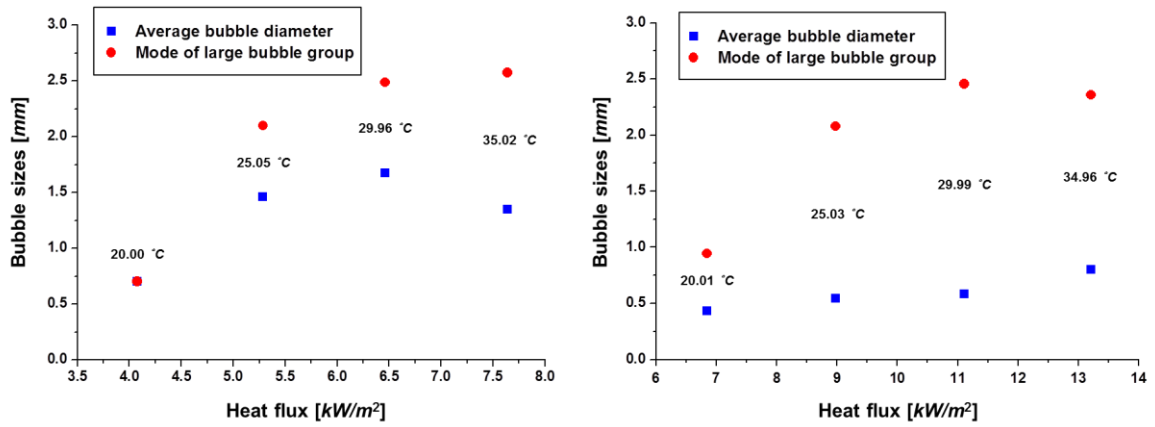


Figure 48 Average bubble diameter and mode of large bubble size with respect to heat flux and inlet subcooling at $G = 300$ (left) and 500 kg/m²s (right)

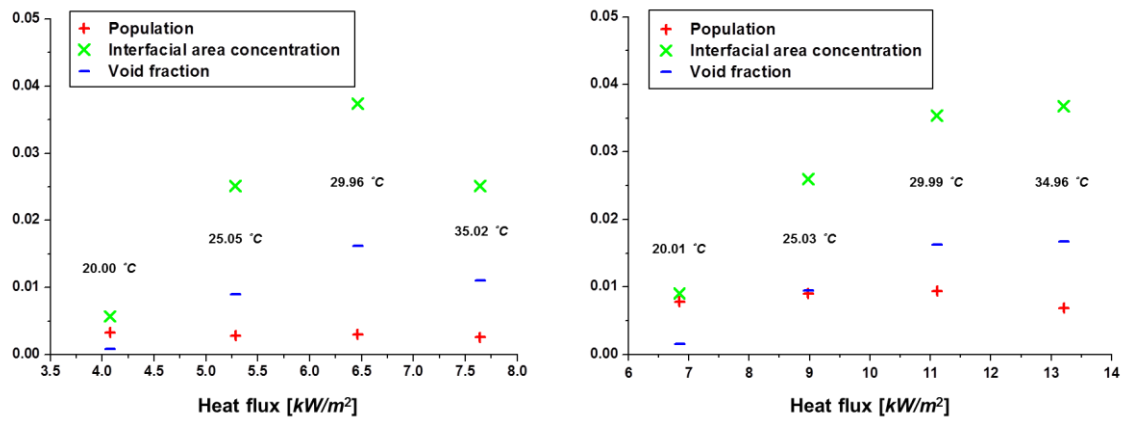


Figure 49 Population, interfacial area concentration, and void fraction with respect to heat flux and inlet subcooling at $G = 300$ (left) and 500 kg/m²s (right)

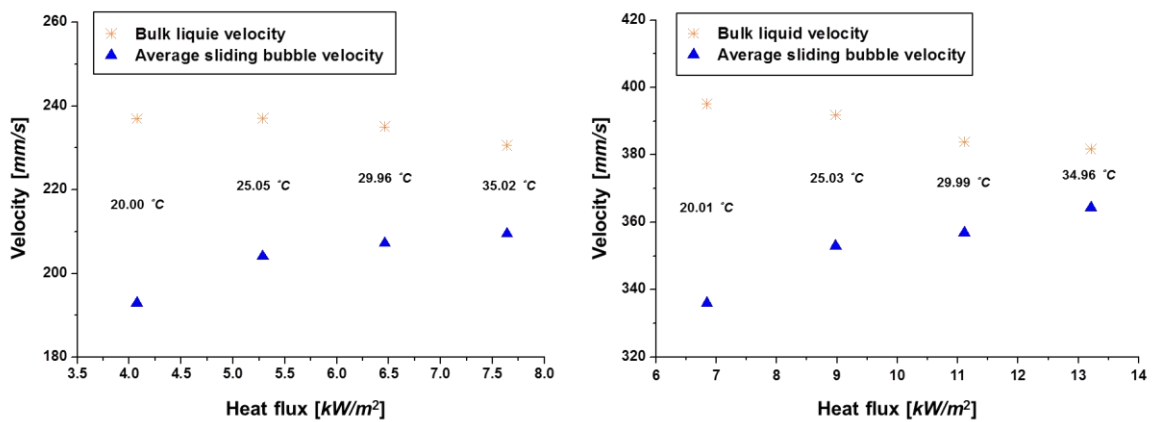


Figure 50 Average bubble sliding velocity and bulk liquid velocity with respect to heat flux and inlet subcooling at $G = 300$ (left) and 500 kg/m²s (right)

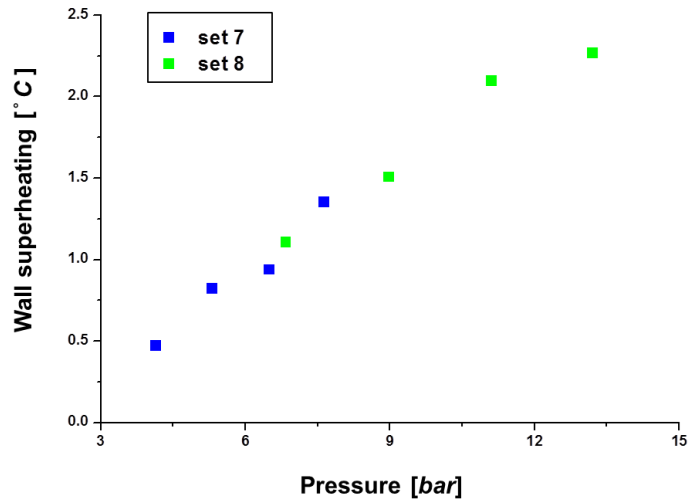


Figure 51 Increase of wall superheating with increasing heat flux and decreasing inlet subcooling

Lastly, Figure 52 represents the close correlations between bubble sizes and outlet qualities, obtained from experimental set 1. It is basically correct that as fluid approaches to saturation state, larger bubbles are observed. However, the several aspects from the previous experiment revealed that specific bubble characteristics could be appeared according to the detail operating conditions, even though the outlet qualities are the same.

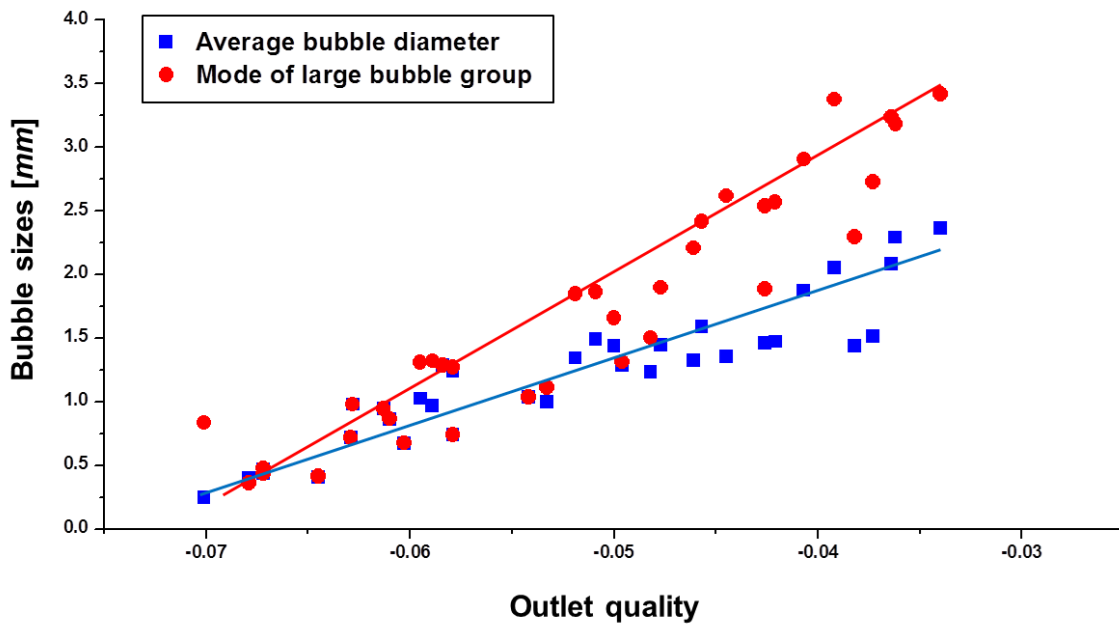


Figure 52 Average bubble diameter and mode of large bubble group with respect to outlet qualities from experimental set 1

4.4 Relation between heat transfer and bubble characteristics

An association between the local heat transfer coefficient and the bubble characteristics, gained from the present experiments, was analyzed. Before entering into it, parametric influences on the local heat transfer coefficient are presented in Figure 53-55. As increasing mass flow rate, the heat transfer coefficient obviously decreases. This trend is against the previous research, L. Zou [9], N. Basu et al. [17, 18], and R. Rzehak et al. [40] which reported mass flow rate doesn't have significant influence on heat transfer. However, Y.Y. Hsieh et al. [14] insisted that there are two opposite effects of mass flow rate on heat transfer and the negative one seems to be mainly operated in the present results, which is caused by more bubbles from larger number of activated nucleation sites at lower mass flow rate. Meanwhile, heat transfer is enhanced at lower inlet subcooling and higher heat flux, as shown in Figure 53 and 54 respectively, and these results agree with those of Y.M. Lie et al. [3].

The influence of pressure on heat transfer has been controversial: L. Zou [9] and R. Rzehak et al. [40] insisted its effect is negligible, while N. Basu et al. [17, 18] reported the enhancement of heat transfer by increasing pressure. In the present results, both conflicting effects are exposed. At $G = 300 \text{ kg} / \text{m}^2 \text{ s}$, improvement of heat transfer was measured at higher pressure, while heat transfer coefficient has a similar value with respect to pressure at $G = 500 \text{ kg} / \text{m}^2 \text{ s}$, as depicted in Figure 55. B. Donnelly et al [19] discovered two mechanisms about how sliding bubbles contribute to the effectiveness of heat transfer: first, sliding bubbles act as bluff body, and next, the wake is generated behind the bubbles and it increases mixing. Meanwhile, stronger agitating motion due to bubbles at higher pressure has been reported by Y.Y. Hsieh et al. [14], and this motion can play a role of improving heat transfer by involving in the mixing effect among two remarked mechanisms. In the present study, at $500 \text{ kg} / \text{m}^2 \text{ s}$, which corresponds to approximately 9000 of Reynold number, enhancement of heat transfer by mixing effect in high pressure condition was not appeared, because every experimental conditions are involved in fully-developed turbulent region, which means the measured heat transfer is already sufficiently enhanced by agitating bubbles, regardless of variations in pressure. However, at low mass flow rate of $300 \text{ kg} / \text{m}^2 \text{ s}$, which corresponds to around 5500 of Reynold number, the agitating effect was manifested as higher heat transfer coefficients with pressure rise, and this is because the condition is involved in less-developed turbulent flow region.

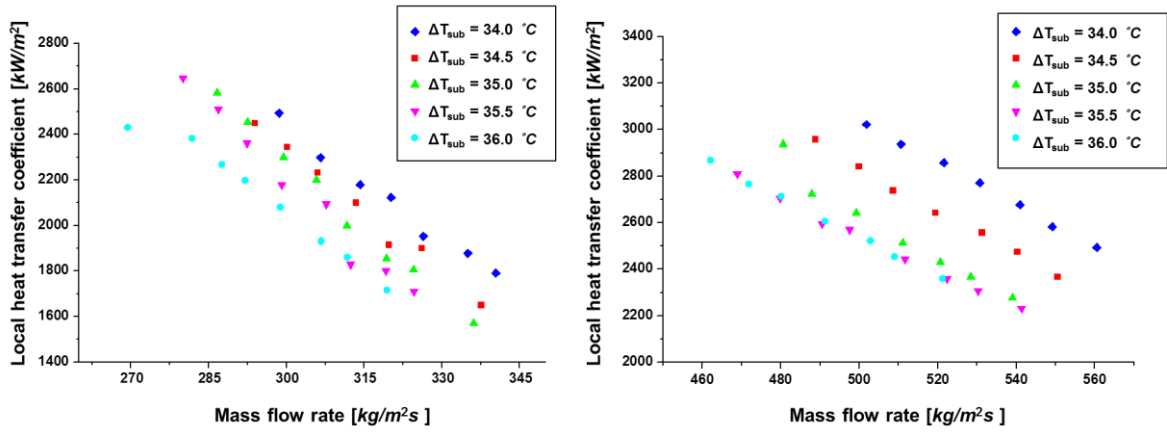


Figure 53 Local heat transfer coefficient with respect to mass flow rate and inlet subcooling around $G = 300$ (left) and $500 \text{ kg/m}^2\text{s}$ (right)

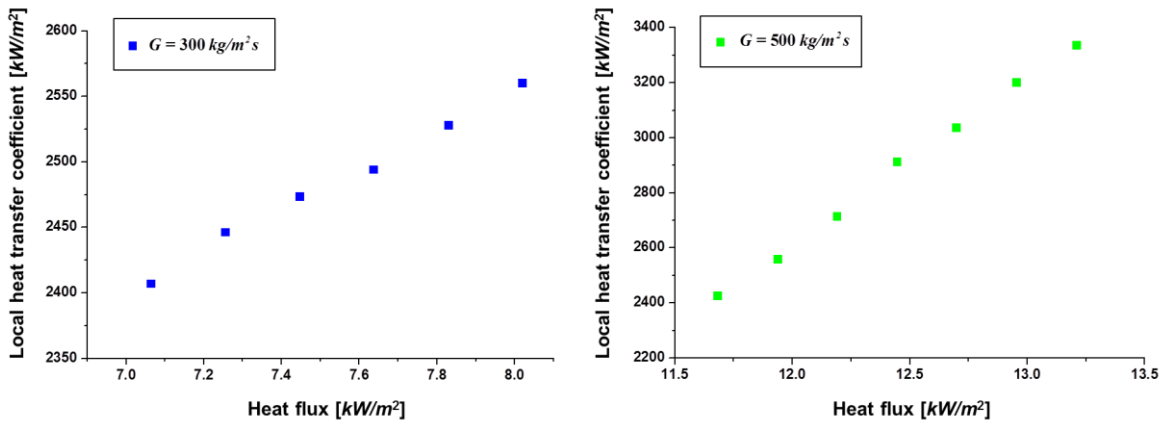


Figure 54 Local heat transfer coefficient with respect to heat flux at $G = 300$ (left) and $500 \text{ kg/m}^2\text{s}$ (right)

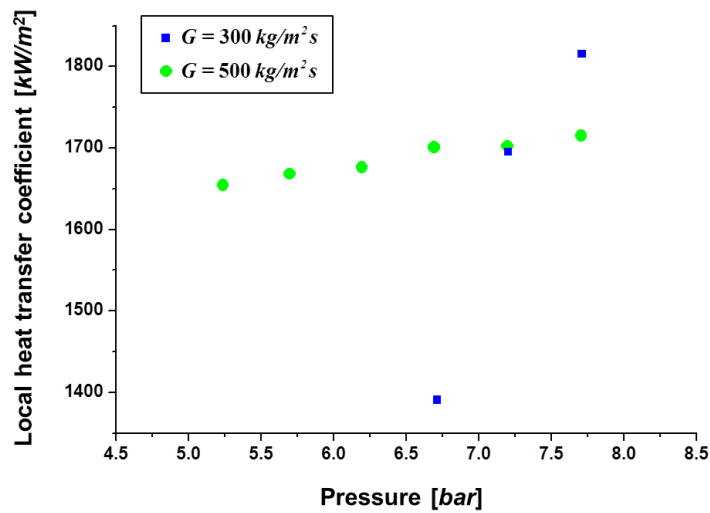


Figure 55 Local heat transfer with respect to pressure at $G = 300$ and $500 \text{ kg/m}^2\text{s}$

Figure 56 shows the positive correlation between the local heat transfer coefficient and outlet quality and this result is accordance with that of S. Basu et al [41]. The results can be explained by the definite logic that more bubbles lead to higher boiling heat transfer. Figure 57 describes the regularity came from mass flow rate, which is hidden in Figure 56. This indicates that mass flow rate doesn't affect to the trend at low mass flow rate of $G = 300 \text{ kg} / \text{m}^2 \text{ s}$, while a set of parabolic lines are drawn for constant mass flow rates around $G = 500 \text{ kg} / \text{m}^2 \text{ s}$.

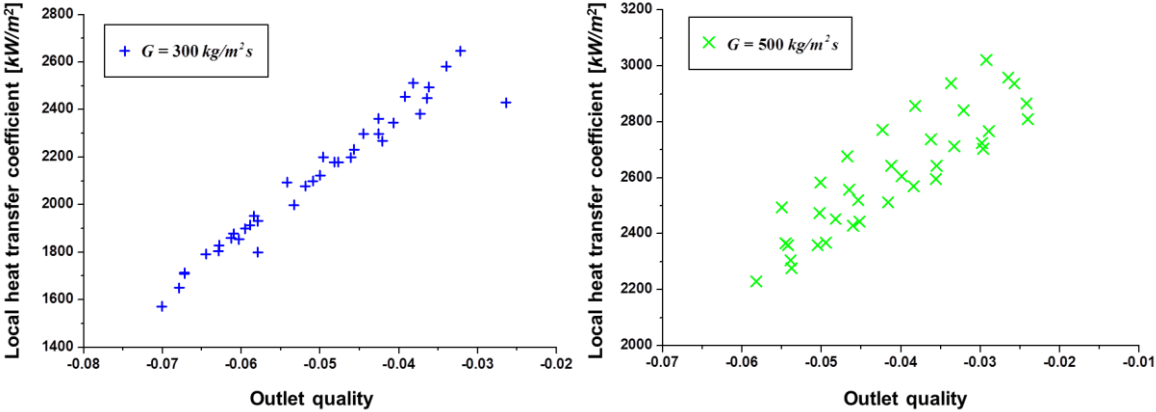


Figure 56 Local heat transfer coefficient with respect to outlet quality from experimental set 1 and 2 at $G = 300$ (left) and $500 \text{ kg/m}^2 \text{ s}$ (right)

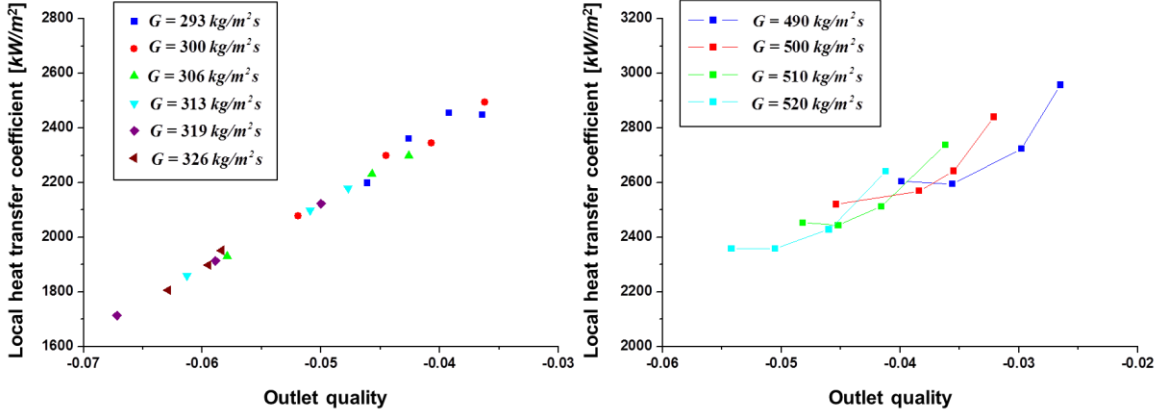


Figure 57 Effect of mass flow rate on the relation between local heat transfer coefficient and outlet quality from experimental set 1 and 2 around $G = 300$ (left) and $500 \text{ kg/m}^2 \text{ s}$ (right)

Variations of the local heat transfer coefficient depending on bubble population and interfacial area concentration are depicted in Figure 58 and 59, respectively. By comparing these two variations, it is obvious that interfacial area concentration is better parameter than the population for predicting the heat transfer efficiency. The results indicate that the decisive

factor of heat transfer efficiency is the contact area between bubbles and surroundings, including bulk liquid and surface, not just the number of them. Moreover, the data, except for pressure case, is well-interpolated in the form of power function as the following:

$$h_i = ba_i^m, \quad (47)$$

The interpolated equations with different coefficient b and power m for each experimental set are listed in Table 11.

Table 11 Coefficient and power of the interpolated equation

| Experiments | Parameter | Region | Interpolated equation |
|------------------------------|----------------------------------|---------------|---------------------------------|
| G & ΔT_{sub} set 1 | G [$kg / m^2 s$] | 270 – 340 | $h_i = 3466.6a_i^{0.1183}$ (48) |
| | ΔT_{sub} [$^{\circ}C$] | 34.0 – 36.0 | |
| G & ΔT_{sub} set 2 | G [$kg / m^2 s$] | 460 - 560 | $h_i = 3435.3a_i^{0.0727}$ (49) |
| | ΔT_{sub} [$^{\circ}C$] | 34.0 – 36.0 | |
| q set 1 | q [kW / m^2] | 7.06 – 8.02 | $h_i = 2683.8a_i^{0.0210}$ (50) |
| q set 2 | q [kW / m^2] | 11.42 – 13.21 | $h_i = 4358.6a_i^{0.1087}$ (51) |

The comparison between the equation (48) and (49) shows that mass flow rate has an impact on the power, not on the coefficient. In addition, by comparing equation (50) and (51), it can be deduced that both the coefficient and power are function of heat flux. Therefore, the equation (47) can be expressed as the equation (52) by containing the influences of two parameters on the coefficient and power.

$$h_i = b(q)a_i^{m(G, q)}, \quad (52)$$

The variations of the heat transfer coefficient by pressure have different aspects depending on mass flow rate. At low mass flow rate region, it has the similar tendency with other four experimental sets, showing a partial parabolic curve, on the other hand, heat transfer is independent on the interfacial area concentration at high mass flow rate region.

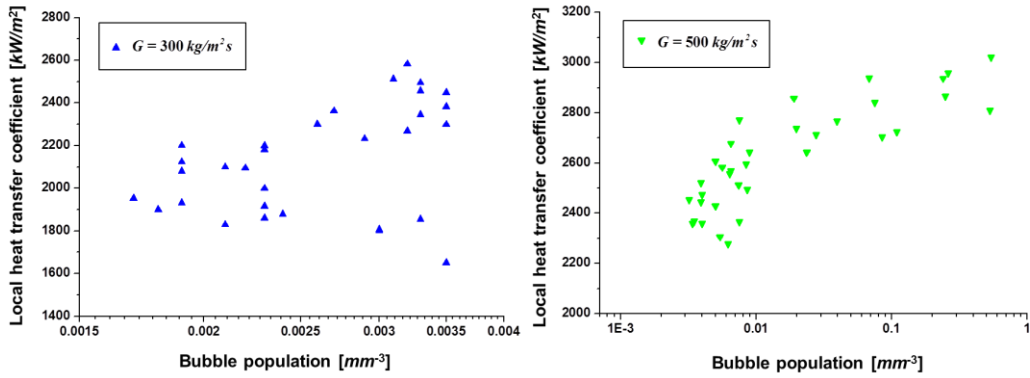


Figure 58 Local heat transfer coefficient with respect to bubble population from experimental set 1 and 2 around $G = 300$ (left) and $500 \text{ kg/m}^2\text{s}$ (right)

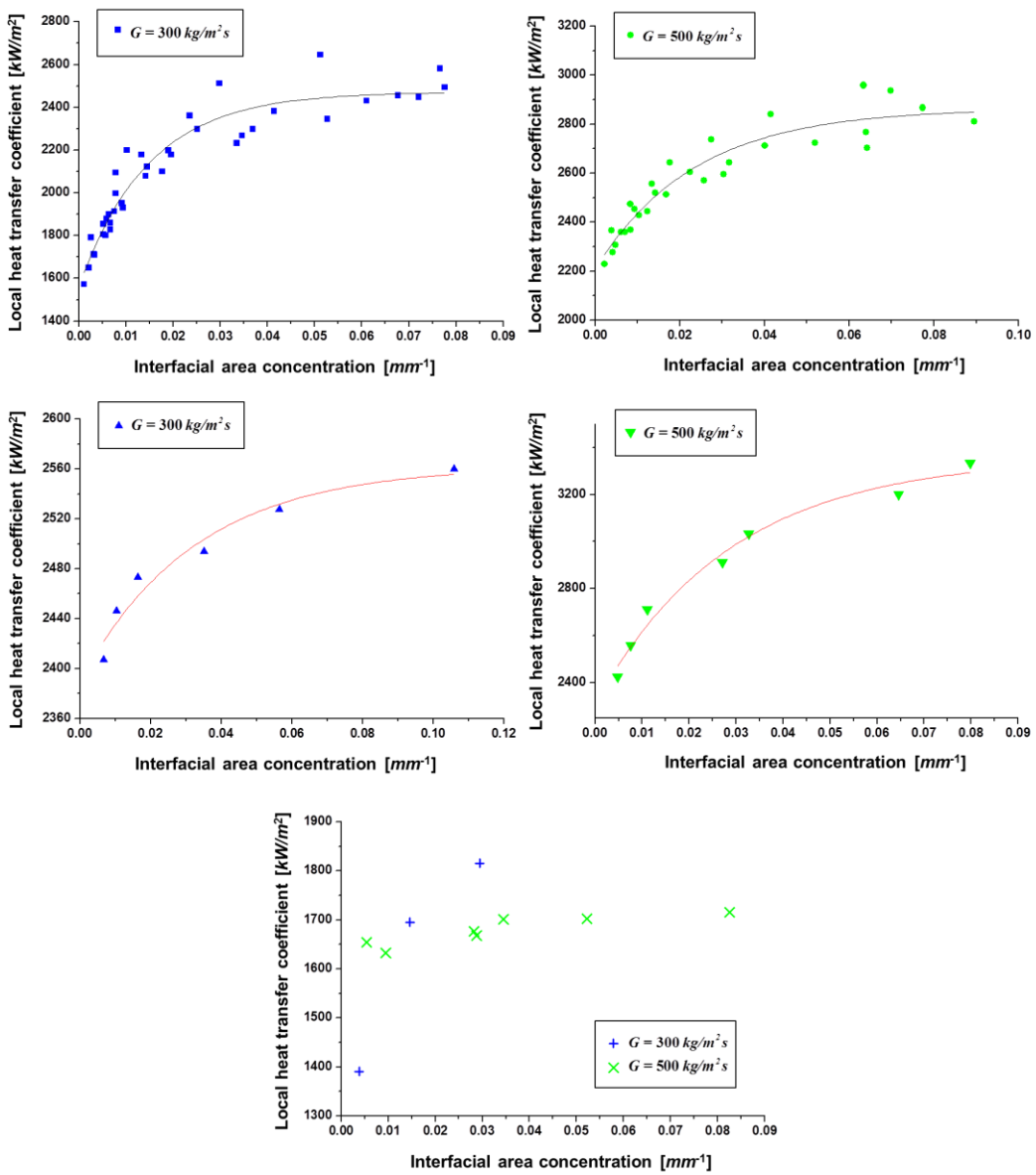


Figure 59 Local heat transfer coefficient with respect to interfacial area concentration with respect to mass flow rate and inlet subcooling (first row), heat flux (second row), and pressure (third row) at $G = 300$ (left) and $500 \text{ kg/m}^2\text{s}$ (right)

4.5 Correlation equations

Two correlation equations for the mode of large bubble group which is the products of coalescence in flowing and slip ratio which represents the interaction between sliding bubbles and surrounding liquid are proposed in the present study. The correlation equations consist of several dimensionless numbers. Slip ratio was used in the correlation equation without certain nondimensionlization, while the dimensionless mode of the large bubble is defined as the equation (53).

$$d_m^+ = \frac{d_m}{\sqrt{\sigma / g \Delta \rho}} \quad (53)$$

4.5.1 Relevant dimensionless numbers to bubble characteristics

Before moving on proposing the correlation equations, selection of appropriate dimensionless numbers which will compose the equations should be made. In the present study, a collection of the candidate dimensionless numbers was created, which have been used in the correlation equations in the literature. Some of them were sorted through investigating the relevance of the numbers to the dimensionless mode of the large bubble group and the slip ratio gained from the present experiments.

Twelve dimensionless numbers are presented in Table 12. In the definition of each number, Δi_{fg} , ζ and S are inlet liquid subcooling enthalpy, heated perimeter, and suppression factor representatively, and the suppression factor is defined as the equation (54).

$$S = \frac{1}{1 + 2.53 \times 10^{-6} Re_{tp}^{1.17}} \quad (54)$$

where Re_{tp} is the two-phase Reynolds number calculated by setting up vapor quality as zero.

Table 12 Dimensionless numbers as candidates for correlation equations

| Dimensionless number | Definition | Involving parameters |
|--------------------------------------|--|----------------------|
| Peculet number, Pe | $\frac{GD_i C_{pf}}{k_f}$ | G |
| Non-dimensional subcooling, θ | $\frac{T_{wi} - T_b}{T_{wi} - T_{sat}}$ | T_{sat}, h |
| Weber number, We | $\frac{G^2 D_i}{\sigma \rho}$ | G |
| Eötvös number, Eo | $\frac{\Delta \rho g D_i^2}{\sigma}$ | P |
| Reynold number, Re | $\frac{GD_i}{\mu_f}$ | G |
| Jakob number, Ja | $\frac{\rho_f C_{pf} (T_{wi} - T_{sat})}{\rho_v i_{fg}}$ | T_{sat} |
| Effective Jakob number, Ja_e | $\frac{\rho_f C_{pf} S(T_{wi} - T_{sat})}{\rho_v i_{fg}}$ | T_{sat} |
| Ratio of densities | ρ_f / ρ_v | P |
| Boiling number, Bo | $\frac{q}{Gi_{fg}}$ | G, q |
| Morton number, Mo | $\frac{g \mu_f^2 \Delta \rho}{\rho_f^2 \sigma^3}$ | P |
| Subcooling number, N_{sub} | $\frac{\Delta i_{sub,in}}{i_{fg}} \frac{\Delta \rho}{\rho_v}$ | $P, \Delta T_{sub}$ |
| Zuber number, N_{zu} | $\frac{q \zeta L}{Av_{ji} i_{fg}} \frac{\Delta \rho}{\rho_v \rho_f}$ | $P, \Delta T_{sub}$ |

Among the numbers, Jakob number, Boiling number and ratio of densities were chosen as the components of correlation equations, and they represent the effects of wall superheating, ratio of mass flow rate and heat flux, and pressure respectively. The three numbers show a consistent and reasonable, based on the aforementioned experimental results, tendency for dimensionless mode of the large bubble group and slip ratio and the fitting data for experimental set 2 are presented in Figure 60 as an example.

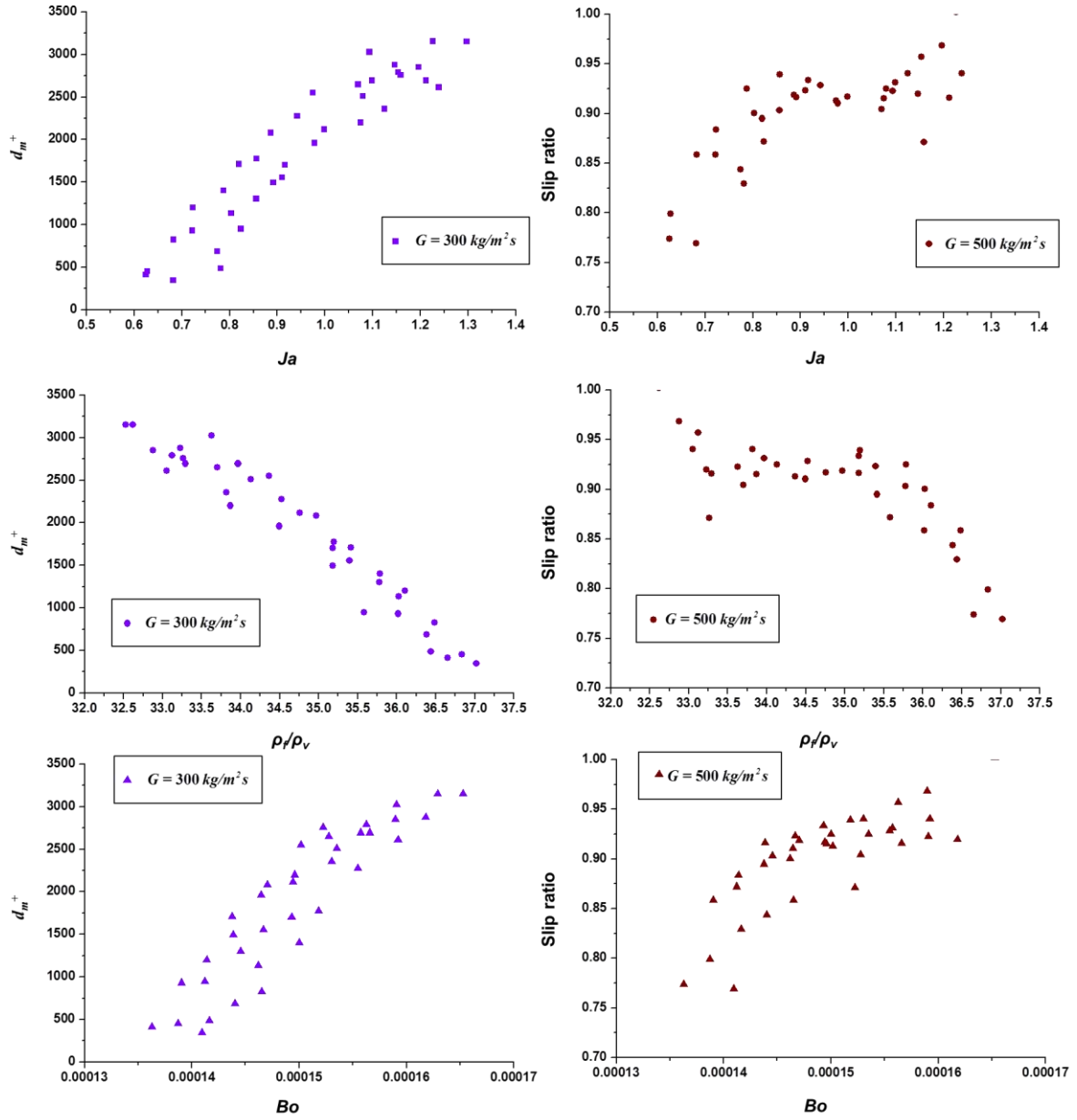


Figure 60 Relevance of Jakob number, Boiling number and ratio of densities to dimensionless mode of large bubble group (left) and slip ratio (right)

4.5.2 Correlation equations for predicting bubble characteristics

A correlation equation, presented in the equation (55), was proposed by O. Zeitoun et al. [42] for predicting average bubble departure diameter and is was demonstrated by U. Puli et al [10] and Y.Y. Hsieh et al [14] for R-134a and water respectively.

$$d_p^+ = \frac{d_p}{\sqrt{\sigma / g \Delta \rho}} = \frac{0.0683(\rho_f / \rho_v)^{1.326}}{Re^{0.324} \left[Ja + \frac{149.2(\rho_f / \rho_v)^{1.326}}{Bo^{0.487} Re^{1.4}} \right]} \quad (55)$$

Since the equation (55) contains Reynold number and three dimensionless numbers which were selected in the previous section, the modified form of the equation (55) was used in the present study. Both dimensionless mode of the large bubble group and slip ratio were correlated with the same form of equation, because these two subjects had similar trends with respect to three dimensionless numbers. Reynold number was subtracted from the original equation due to its weak relevance on the graph. The proposed correlation equations for predicting dimensionless mode of the large bubble group and slip ratio are expressed as:

$$d_m^+ \text{ and } C_r = \frac{A(\rho_f / \rho_v)^a}{Ja^b + \frac{B(\rho_f / \rho_v)^c}{Bo^d}}, \quad (56)$$

The empirical coefficients A, B, a, b, c and d were determined by least square method and they are given in Table 13.

Table 13 Coefficients of correlation equations (56)

| Parameter | A | B | a | b | c | d |
|------------------|-----------|----------|----------|----------|----------|----------|
| d_m^+ | 1.747E+18 | 0.2726 | 0 | 1 | 8.781 | 0.5 |
| C_r | 9206.48 | 30.46 | 0 | 1 | 0.07392 | 0.6275 |

The comparisons of the correlations of dimensionless mode of the large bubble group and slip ratio and the current experimental data are shown in Figure 61 and 62. The figure suggests that the data trend agrees well with the prediction. Both measured data are located within $\pm 10\%$ of deviation from the prediction.

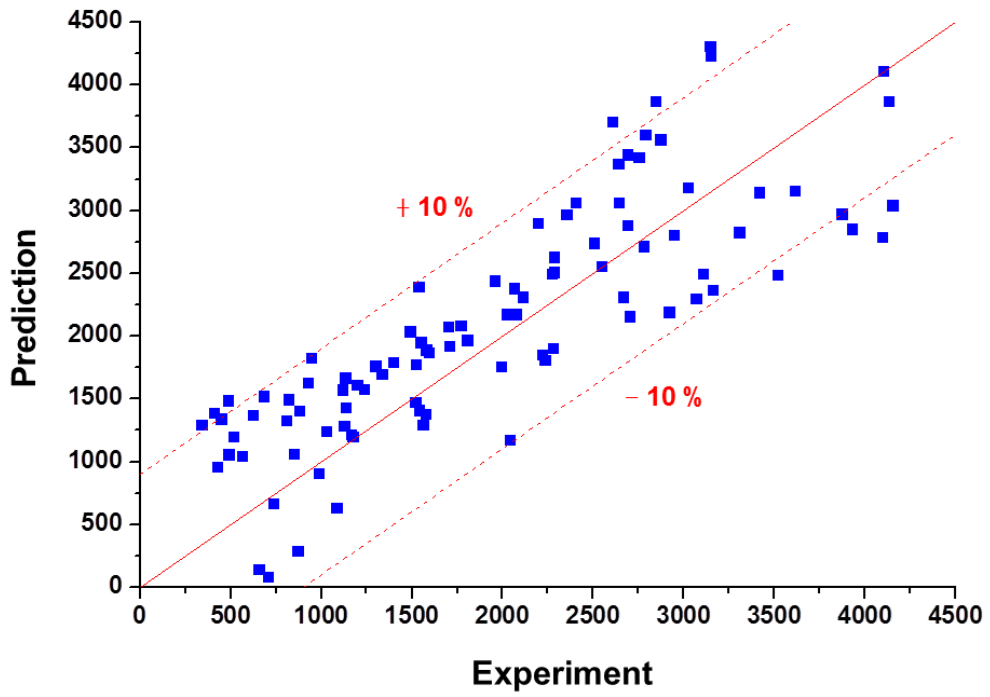


Figure 61 Comparison between predicted and measured dimensionless mode of the large bubble group

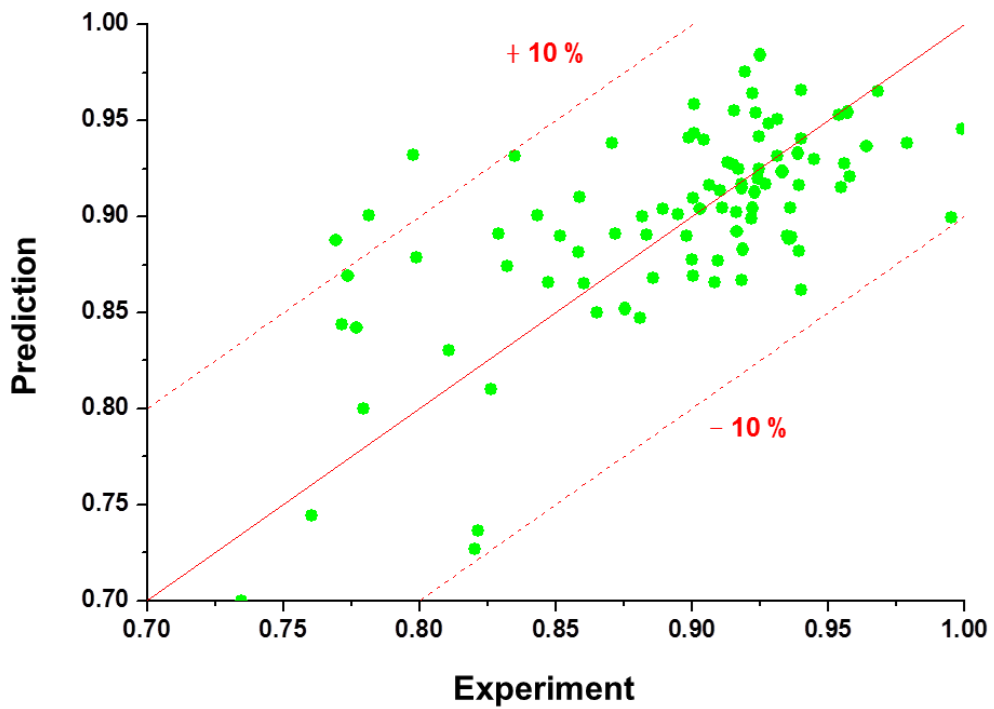


Figure 62 Comparison between predicted and measured slip ratio

5 Conclusion

Visual investigation by means of high-speed camera was made to observe the bubble characteristics of coalesced sliding bubbles and associated heat transfer coefficient was measured.

Three groups of experiments were conducted for discovering the singular parametric effect of mass flow rate, inlet subcooling, heat flux, and pressure, at the same time, an additional group of experiment with adjusting outlet qualities was carried out for revealing the coupling effect of heat flux and inlet subcooling. The relation between the heat transfer coefficient and the bubble characteristics was analyzed. From these studies results the following conclusions were drawn:

1. Bi-modal shape of size distributions were commonly obtained in both mass flow rate regions. It was concluded that the large bubble group is the outcome of coalescence during flowing, while the small bubble group is composed of raw bubbles without significant merging.
2. Most of bubbles slide along with upper wall. Large bubble has higher sliding velocity and it is converged to the bulk liquid velocity. This is because of slender shape of larger bubble and it makes only one way of coalescing in flowing possible: large bubble catch up with small bubble.
3. At higher mass flow rate or higher inlet subcooling, smaller mode of the large bubble group, declined bubble population with upward tail at the highest mass flow rate, lower variance of the large bubble group, and lower kurtosis of the small bubble group were observed. Average sliding bubble velocity was irrespective with mass flow rate due to different sizes of sliding bubbles.
4. Increase of heat flux resulted in increasing bubble sizes, population, and variance and kurtosis of each size group. Slip ratio decreases with higher imposed heat flux and sudden explosive small bubble generation was detected at certain value of heat flux.

5. Pressure increments had remarkably strong influence on activation of nucleation sites. This effect was exceptionally revealed at high mass flow rate region where the small bubble group dominates the size distribution.

6. Coupling effect was observed: at higher heat flux and higher inlet subcooling, higher wall superheating was observed, but it resulted only in increase of bubble sizes, not in the population. The phenomenon seems to be due to the higher energy for generating bubbles but colder liquid around the nucleation sites.

7. The feasibility of applying the predictive model for the onset of nucleate boiling, Saha and Zuber (1974), in horizontal tube was validated from the results of void fraction and kurtosis of the small bubble group.

8. Interfacial area concentration was the most influential bubble characteristics to the heat transfer coefficient. They were well-interpolated as a set of power functions.

9. Correlation equations for predicting dimensionless mode of the large bubble group and slip ratio were derived. These are composed of Jakob number, ratio of densities, and Boiling number because they showed continent associations with the two correlated subjects. The maximum deviation between prediction and experiments were $\pm 10\%$ for both targets.

It should be stressed here that although the results can help the fundamental understanding of bubble dynamics, ultimately, the clarified bubble characteristics in this study, which are represented as the distributions of bubble sizes and sliding velocities as well as coalescence in flowing, can be used for developing more rigid population balance framework in future study.

6 Reference

- [1] L.E. Patruno, J.M. Marchetti, C.A. Dorao, H.F. Svendsen, H.A. Jakobsen. Droplet size distribution after liquid entrainment in horizontal stratified two-phase three-field dispersed flow. *Chemical Engineering Science* 2010;65(4):1407-1414.
- [2] L.E. Patruno, C.A. Dorao, P.M. Dupuy, H.F. Svendsen, H.A. Jakobsen. Identification of droplet breakage kernel for population balance modeling. *Chemical Engineering Science* 2009;64(4):638-645.
- [3] Y.M. Lie, T.F. Lin. Subcooled flow boiling heat transfer and associated bubble characteristics of R-134a in a narrow annular duct. *International Journal of Heat and Mass Transfer* 2006;49(13):2077-2089.
- [4] H. Eriksen. Development of calculation model for heat exchangers in subsea system. Master thesis, Norwegian University of Science and Technology 2010.
- [5] J.F. Klausner, R. Mei, D.M. Bernhard, L.Z. Zeng. Vapor bubble departure in forced convection boiling. *International Journal of Heat and Mass Transfer* 1993;36(3):651-662.
- [6] F.C. Gunther. Photographic study of surface-boiling heat transfer to water with forced convection. *Trans. ASME* 1951;73(2):115-123.
- [7] J. Garnier, E. Mannon, G. Cubizolles. Local measurements on flow boiling of refrigerant 12 in a vertical tube. *Multiphase Science and Technology* 2001;13(1&2):1-111.

[8] V. Prodanovic, D. Fraser, M. Salcudean. Bubble behavior in subcooled flow boiling of water at low pressures and low flow rates. *International Journal of Heat and Mass Transfer* 2002;28(1):1-19.

[9] L. Zou. Experimental study on subcooled flow boiling on heating surfaces with different thermal conductivities. Doctoral dissertation, University of Illinois 2010.

[10] U. Puli, R.A. Kumar. Parametric effect of pressure on bubble size distribution in subcooled flow boiling of water in a horizontal annulus. *Experimental Thermal and Fluid Sciences* 2012;37:164-170.

[11] R. Maurus, T. Sattelmayer. Bubble and boundary layer behavior in subcooled flow boiling. *International Journal of Thermal Sciences* 2006;45(3):257-268.

[12] B.J. Yun, A. Splawski, S. Lo, C.H. Song. Prediction of a subcooled boiling flow with advanced two-phase flow models. *Nuclear Engineering and Design* 2012;253:351-359.

[13] A.B. Ozer, A.F. Oncel, D.K. Hollingsworth, L.C. Witte. The effect of sliding bubbles on nucleate boiling of a subcooled liquid flowing in a narrow channel. *International Journal of Heat and Mass Transfer* 2011;54(9):1930-1940.

[14] Y.Y. Hsieh, L.J. Chiang, T.F. Lin. Subcooled flow boiling heat transfer of R-134a and the associated bubble characteristics in a vertical plate heat exchanger. *International Journal of Heat and Mass Transfer* 2002;45(9):1791-1806.

- [15] S. Li, S. Tan, C. Xu, P. Gao, L. Sun. An experimental study of bubble sliding characteristics in narrow channel. *International Journal of Heat and Mass Transfer* 2013;57(1):89-99.
- [16] G. Sateesh, S.K. Das, A.R. Balakrishnan. Analysis of pool boiling heat transfer: effect of bubbles sliding on the heating surface. *International Journal of Heat and Mass Transfer* 2005;48(8):1543-1553.
- [17] N. Basu, G.R. Warriar, V.K. Dhir. Wall heat flux partitioning during subcooled flow boiling: Part 1-Model development. *Transactions of the ASME-C-Journal of Heat Transfer* 2005;127(2):131-140.
- [18] N. Basu, G.R. Warriar, V.K. Dhir. Wall heat flux partitioning during subcooled flow boiling: Part II -Model validation. *Transactions of the ASME-C-Journal of Heat Transfer* 2005;127(2):141-148.
- [19] B. Donnelly, T.S. O'Donovan, D. B. Murray. Surface heat transfer due to sliding bubble motion. *Applied Thermal Engineering* 2009;29(7):1319-1326.
- [20] M. Lin, P. Chen. Photographic study of bubble behavior in subcooled flow boiling using R-134a at low pressure range. *Annals of Nuclear Energy* 2012;49:23-32.
- [21] C.P. Yin, Y.Y. Yan, T.F. Lin, B.C. Yang. Subcooled flow boiling heat transfer of R-134a and bubble characteristics in a horizontal annular duct. *International Journal of Heat and Mass Transfer* 2000;43(11):1885-1896.

[22] L.C. Ruspini. Experimental and numerical investigation and two-phase flow instabilities. Doctoral dissertation, Norwegian University of Science and Technology 2013;4..

[23] D. Doder. Experimental analysis of the pressure characteristic curve of a forced convection boiling flow in single horizontal channel. Master thesis, Norwegian University of Science and Technology 2013.

[24] P.A. Kew, K. Cornwell. Correlations for the prediction of boiling heat transfer in small-diameter channels. *Applied Thermal Engineering* 1997;17(8):705-715.

[25] M. Lee, L.S.L. Cheung, Y.K. Lee, Y. Zohar. Height effect on nucleation-site activity and size-dependent bubble dynamics in microchannel convective boiling. *Journal of Micromechanics and Microengineering* 2005;15(11):2121.

[26] G.M. Lazarek, S.H. Black. Evaporative heat transfer, pressure drop and critical heat flux in a small vertical bubble with R-113. *International Journal of Heat and Mass Transfer* 1982;25(7):945-960.

[27] P.H. Yoon, J. Jeong, Y.T. Kang. Boiling hysteresis at low temperature on enhanced tubes. *International Journal of Refrigeration* 2004;27(1):4-9.

[28] M. Piasecka, S. Hozejowska, M.E. Poniewski. Experimental evaluation of flow boiling incipience of subcooled fluid in a narrow channel. *International Journal of Heat and Mass Transfer* 2004;25(2):159-172.

[29] VisiSize software operation manual for VisiSize 6. Oxford Lasers Imaging Division 2010.

- [30] K. Pearson, E.S. Pearson. *Biometrika*. New York: Cambridge;1902.
- [31] K.O. Bowman, L.R. Shenton. The beta distribution, moment method, Karl Pearson and RA Fisher. *Far East Journal of Theoretical Statistics* 2007;23(2):133.
- [32] S.C. Lee, H. Dorra, S.G. Bankoff. A critical review of predictive models for the onset of significant void in forced-convection subcooled boiling, *ASME-PUBLICATIONS-HTD* 1993;217:33.
- [33] R. Situ, T. Hibiki, M. Ishii, M. Mori. Bubble lift-off size in forced convective subcooled boiling flow. *International Journal of Heat and Mass Transfer* 2005;48(25):5536-5548.
- [34] J.J. Xu, B.D. Chen, Y.P. Huang, X. Yan, D.W. Yuan. Experimental visualization of sliding bubble dynamics in a vertical narrow rectangular channel. *Nuclear Engineering and Design* 2013;261:156-164.
- [35] A.A. Voloshko, A.V. Vurgaft. Dynamics of vapor-bubble break off under free-convection boiling conditions. *Heat Transfer-Soviet Research* 1970;2(6):136-141.
- [36] V.S. Golorin, B.A. Kol'chugin, E.A. Zakharova. Investigation of the mechanism of nucleate boiling of ethyl alcohol and benzene by means of high-speed motion-picture photography. *Heat Transfer-Soviet Research* 1978;10(4):79-98.
- [37] E.L. Bibeau, M. Salcudean. A study of bubble ebullition in forced-convective subcooled nucleate boiling at low pressure. *International Journal of Heat and Mass Transfer* 1994;37(15):2245-2259.

[38] R. Maurus, V. Ilchenko, T. Sattelmayer. Automated high-speed video analysis of the bubble dynamics in subcooled flow boiling. *International Journal of Heat and Fluid Flow* 2004;25(2):149-158.

[39] V.I. Tolubinsky, D.M. Kostanchuk. Vapour bubbles growth rate and heat transfer intensity at subcooled water boiling. *Proceedings of the 4th International Heat Transfer Conference* 1970;5.

[40] R. Rzehak, E. Krepper. CFD for subcooled flow boiling: Parametric variations. *Science and Technology of Nuclear Installations* 2013.

[41] G.J. Michana, Y. Peles, M.K. Jensen. Flow boiling of R134a in circular microtube-Part1: Study of heat transfer characteristics 2011;133:051502-1-051502-9.

[42] O. Zeitoun, M. Shoukri. Bubble behavior and mean diameter in subcooled flow boiling. *Journal of Heat Transfer* 1996;118(1):110-116.